TUNING THE THERMO-MECHANICAL RESPONSE AND CELL MORPHOLOGY OF POROUS SHAPE MEMORY POLYMER SCAFFOLDS FOR ENDOVASCULAR OCCLUSION DEVICES

A Dissertation

by

SAYYEDA MARZIYA HASAN

Submitted to the Office of Graduate and Professional Studies of
Texas A&M University
in partial fulfillment of the requirements for the degree of

DOCTOR OF PHILOSOPHY

Chair of Committee,	Duncan J. Maitland
Committee Members,	Karen L. Wooley
	Melissa A. Grunlan
	Balakrishna Haridas
Head of Department,	Anthony Guiseppi-Elie

May 2016

Major Subject: Biomedical Engineering

ABSTRACT

Shape memory polymers are a class of smart materials that have the capability to transition from a mechanically programmed secondary shape to their original shape. This unique shape change behavior is useful for medical applications such as sutures and self-expanding stents. Polyurethane SMP foams have been studied as an implantable material for embolic applications due to their high surface area to volume ratio, known biocompatibility, and tunable mechanical properties. Passive actuation of SMP foam in physiological conditions is dependent on factors such as hydrophobicity and transition temperature of the polymer, which affect plasticization by water and shape recovery.

This research focuses on altering the chemical structure of the foam matrix to control the glass transition temperature (T_g) and actuation time. Incorporation of nano-fillers into the foam matrix was used to induce radio-opacity and enhance mechanical properties such as toughness and tensile strength. Further, the effect of filler concentration and dispersion within the liquid phase on mechanical toughness was evaluated. Lower filler concentrations yielded nanocomposites with improved mechanical properties and thermal stability, with tunable actuation profiles and shape recovery.

Control over the cell morphology was achieved by synthesizing a siloxane-glycol amphiphile to serve as a foaming surfactant. Changes in foam morphology and cell size due to changes in chemical structure and concentration of the surfactant were studied. This work provided enhanced control over the foam morphology and the chemical,

thermal, and mechanical properties of the SMP foam for use in medical applications, specifically as vascular embolic agents.

DEDICATION

To my wonderful family, who supported me through all my endeavors and encouraged me to achieve my goals despite the setbacks.

ACKNOWLEDGEMENTS

I would like to thank my committee chair, Dr. Duncan Maitland for his support and guidance throughout the course of my research. He was instrumental to my success in the Biomedical Device Laboratory and my growth as a scientist. His mentoring style allowed me to learn from my mistakes and think critically to solve problems. Dr. Maitland always been available to answer my questions, listened to my concerns, and when when he couldn't help me right away, guided me in the right direction. Dr. Maitland always treated me like a peer which was refreshing and allowed me to build my confidence as a researcher. He accepted me into his lab, despite my short comings, and mentored me to become an independent thinker and a self-possessed individual.

I would also like to acknowledge my committee members Dr. Melissa Grunlan, Dr. Karen Wooley, and Dr. Balakrishna Haridas for their extended technical support throughout my research. I would specifically like to thank Dr. Grunlan for her time and feedback on designing my experimental protocol for surfactant synthesis and troubleshooting the product purification step to improve my yield.

I would like to extend my appreciation to the laboratory for synthetic-biological interactions and its director, Dr. Karen Wooley, for providing the key instrumentation I needed for the mechanical evaluation of my materials. Additionally, I would like to thank the collaborators for this work, Fang Zhou, from the Characterization Facility at the University of Minnesota, who acquired all of the TEM images necessary for this work. Thanks also go to my collaborators at Lawrence Livermore National Laboratory, specifically Dr. Thomas Wilson and Dr. Jennifer Rodriguez. Dr. Wilson has been an

academic mentor to me since my arrival at the Biomedical Device Laboratory. He has provided valuable advice to me that allowed me to gain a better understanding of my research and the scientific process. Dr. Jennifer Rodriquez has been my dear friend and colleague. Her support and persistence gave me the confidence to pursue my Ph.D. and her technical input aided my progress in all my research goals. I also want to extend my gratitude to the Laboratory for Biological Mass Spectrometry at Texas A&M University and Dr. Yohannes Rezenom and Vanessa Santiago for their technical support in acquiring mass spectrometry data that was crucial to my project. My thanks goes out to Dr. Jeffery Raymond for guiding me through the basics of research during my first semester as a graduate student. Additionally, I would like to thank Dr. Tiffany Gustafson and Julie Grinde for acquiring X-ray images of my polymer samples at the Texas Institute of Preclinical Studies.

My peers at the Biomedical Device Laboratory also deserve my gratitude for all of their help and support throughout my time at Texas A&M. Special thanks to Rachael Muschalek, Nicole Rivera, Landon Nash, Anthony Boyle, Todd Landsman, Alexa Easley, Garrett Harmon, Jane Fredrick, Harrison Emery for their time and effort spent brainstorming new ideas, assisting me with new experimental setup, and being a good friend over the years.

I would like to thank my undergraduate mentors at Texas Lutheran University, Dr. John McClusky and Dr. William Davis, for getting me interested in chemistry and polymer science. Their encouragement and mentorship allowed me to realize my interests and helped me recognize my career goals.

Finally, thanks to my mother and father, Gulshan Hasan and Sayed Shameem Hasan, for inspiring me to pursue a career in a STEM field. Their hard work and sacrifice has given me a chance to achieve my dreams and provided an example for me to follow for my professional and personal life. My sisters, Sayyeda Tooba Hasan and Sayyeda Ayesha Hasan, supported all my decisions and have motivated me to be the best version of myself. I would also like to recognize my wonderful friends Brian Ramirez, Jessica Unterberger, Chelsea Cruz, Stephen Gutierrez, and Jonathan Eagle for their patience and love throughout the years, along with their unwavering confidence in me, that provided the platform I needed to progress in life.

NOMENCLATURE

Al_2O_3	Aluminum oxide
$CDCl_3$	Deuterated chloroform
CO_2	Carbon dioxide
D	Dispersion parameter
DCTB	trans-2-[3-(4-t-Butylphenyl)-2-methyl-2-propenylidene]malono-nitrile
DI H_2O	Deionized water
DMA	Dynamic mechanical analysis
DSC	Differential scanning calorimetry
E’	Dynamic shear storage modulus
E”	Dynamic shear loss modulus
FOW	foam-over-wire
FTIR	Fourier transform infrared
GDC	Gugleilmi detachable coil
HDI	Hexamethylene diisocyanate
H’NMR	Proton nuclear magnetic resonance
HPED	N,N,N’,N’-Tetrakis(2-hydroxypropyl)ethylenediamine
ICP-MS	Inductively coupled plasma mass spectrometry
IPDI	Isophorone diisocyanate
ISAT	International Subarachnoid Aneurysm Trial
KBr	Potassium bromide

KTFA	potassium trifluoroacetate
MALDI	Matrix-assisted laser desorption ionization
NCO	Isocyanate
Nitinol	Nickel-titanium alloy
OH	Hydroxyl
PDMS	poly(dimethylsiloxane)
PEG	Polyethylene glycol
Pt	platinum(0)-1,3-divinyl-1,1,3,3-tetramethyldisiloxane complex
Rh	tris(triphenylphosphine)rhodium(I) chloride
RO H_2O	Reverse osmosis water
SAH	Subarachnoid hemorrhage
SEM	Scanning Electron Microscopy
SiO_2	Silicon dioxide
SMP	Shape memory polymer
TEA	Triethanolamine
TEM	Transmission electron microscopy
TGA	Thermogravimetric analysis
T_g	Glass transition temperature
TMHDI	trimethyl-1,6-hexamethylene diisocyanate, 2,2,4- and 2,4,4-mixture
TS	1,1,1,3,5,5,5-heptamethyltrisiloxane
T_{trans}	Transition temperature

W	Tungsten
X.D.	X-ray density

TABLE OF CONTENTS

Page

LIST OF FIGURES

Page

Page

Page

Page

LIST OF TABLES

Page

CHAPTER I

INTRODUCTION*

1.1 Shape memory polymers (SMPs)

Shape memory polymers (SMPs) are "smart" materials that have the capability of shape change from a programmed secondary shape to a primary shape upon the input of an external stimulus such as heat, light, or electricity. [1-3] For thermal actuation, the polymer can be synthesized in a primary shape, heated above its transition temperature and mechanically programmed into a secondary shape. [4] Once cooled below the transition temperature, the material will remain in the secondary shape until it is heated again to return to its original shape. [4] Shape fixity occurs when the polymer chains are forced to align into conformations with net orientation versus equilibrium random conformations and cooled below the actuation transition to restrict chain mobility. [5] Entropic recovery so that the polymer chains may once more achieve random orientation then drives the return to original shape. [5] Due to this shape memory behavior, SMPs have a wide range of uses in medical and industrial applications such as vascular stents, occlusion devices, and self-controlled actuators. [1, 6]

Since their discovery in the 1980's, shape memory polymers (SMPs) have become widely used in applications that require innovative materials. [7, 8] The active shape change response of SMPs has been harnessed to develop smart, stimuli-responsive

---

* Parts of this chapter were reprinted from "Porous Shape Memory Polymers: Design and Applications," by Sayyeda M. Hasan, Landon D. Nash, Duncan J. Maitland, Journal of Polymer Science Part B: Polymer Physics 2016. Copyright (2016) John Wiley and Sons.

systems that have utility in a wide range of applications including biomedical, aerospace, textiles, and robotics. [8] The term "shape memory" was first coined by Vernon in 1941, however it was not until the 1960's when crosslinked polyethylene was used to develop heat-shrinkable tubes and films. [9, 10] Over the last two decades, the growing interest in SMPs has facilitated commercial applications of these materials in textiles and smart customer products. [10]

SMPs consist of net points, which are a part of the stable polymer network, and reversible switching segments. [2, 11] Net points are responsible for the original shape while the switching segments provide the secondary shape and allow for shape change to occur. [12] As shown in **figure 1.1**, a thermally-actuated SMP can be programmed, *via* external stress, into a secondary shape after being heated above the transition temperature of the switching segments. [9] The new shape can be set by cooling at a constant load. The new shape is at a higher energy state because the new orientation of the polymer chains decreases the entropy of the system. However, the rigidity of the polymer chains below the transition temperature prevents the polymer from relaxing to the lower energy primary shape. However, when heated above the transition temperature, the programmed SMP returns to its original shape due to entropic recovery of the net points. [5, 9] In addition to ambient changes in temperature, this shape change can be triggered by different stimuli such as light, magnetic field, pH, solvent, and electricity and is dependent on the polymer type and incorporation of additives such as nanoparticles. [4, 12]

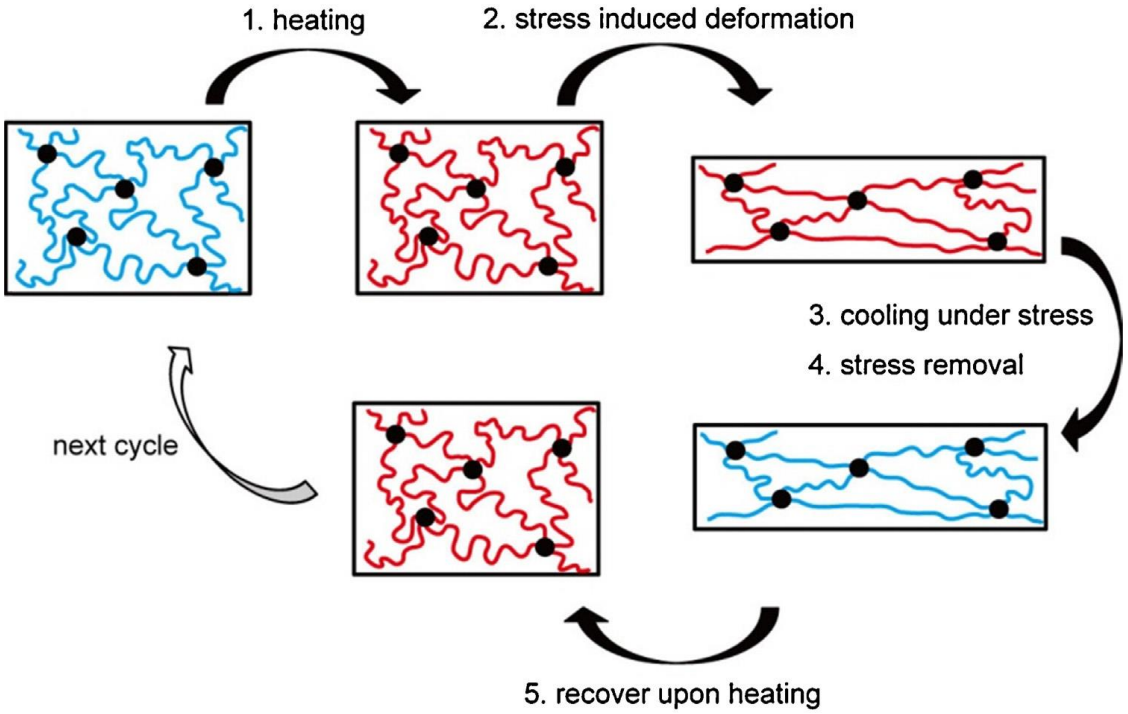

Figure 1.1: The molecular mechanism of a typical thermally-actuated SMP. (Reproduced from [9], with permission from Elsevier.)

1.2 Fabrication of SMP foams

1.2.1 Gas blowing

Although gas blowing is traditionally used to create commercial polymer foams for thermal and mechanical insulation, the use of this fabrication technique has significantly increased in the medical industry. [13, 14]

Regardless of the desired application or foaming process being used, cell nucleation and growth of bubbles is important for the development of pores. [15, 16] Bubbles can be generated using three different methods: chemical, physical, and biological blowing. Chemical blowing agents generate gas due to a chemical reaction

while physical blowing agents cause bubble formation as a result of mechanical action or phase transitions. [16] Biological agents are usually bacterial species that generate gas as a result of their metabolic functions. [16] Carbon dioxide (CO_2) and other volatile solvents are typical blowing agent due to their low critical point, non-flammability, and non-toxicity. [15, 17] **Figure 1.2** shows a typical SEM image of foam blown using CO_2. [18]

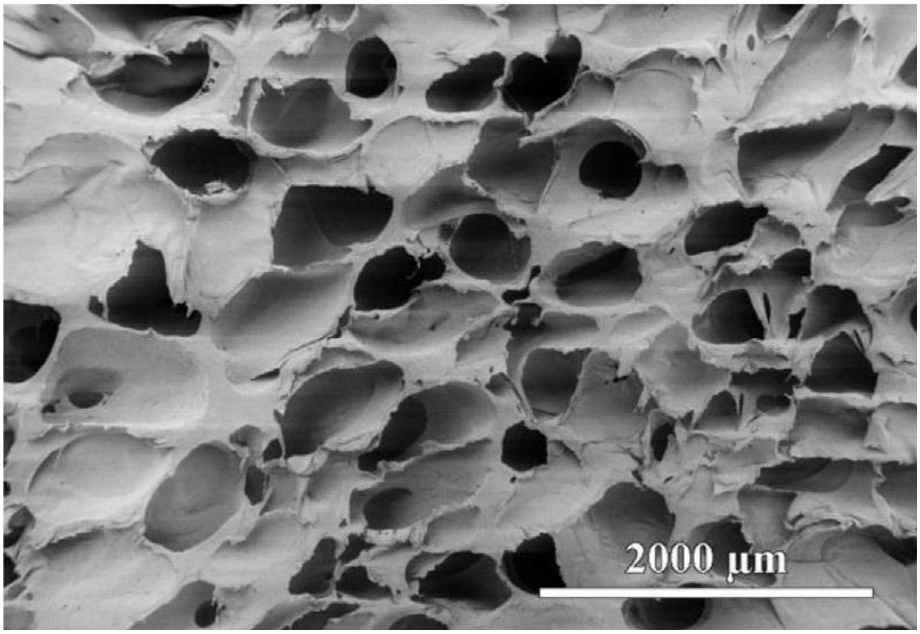

Figure 1.2: Scanning electron microscopy (SEM) image of a CO_2-blown poly (butylene succinate) foam. (Reproduced from [18], with permission from Elsevier.)

Gas foaming can be divided into two classes. The first class occurs when a liquid phase turns to vapor as a result of pressure drop or a temperature rise. [16] Singhal *et al.* developed SMP foams that utilized gas blowing to achieve solid polyurethane foams. This polymer system was chemically crosslinked during foaming to maintain the pore

morphology and prevent bubble coalescence. [19] Water was the chemical blowing agent for the synthesis. During foam blowing, water reacted with the isocyanate monomers to generate carbon dioxide. The released gas provided cell nucleation and yielded a porous material with good interconnectivity. Pore structure and interconnectivity was tuned by controlling the type of foaming agent and its concentration in the polymer-gas mixture. [17] Reduced scaffold toxicity for *in vivo* applications is an advantage of gas blowing compared to other fabrication methods. [13] Disadvantages associated with gas blowing include difficult control over pore sizes and connectivity. [13] Molecular weight of the monomers and concentrations of foaming agents, specifically catalysts, provide some variation in pore morphology and membrane openness. Lee *et al*. fabricated SMP foams with controllable cell size and open-versus-closed morphology by modifying the gelling catalyst concentration and the polyol molecular weight. [20] This played a major role on the crosslink density of the foams along with their density, shape fixity, and shape recovery. Similarly, Kang et al. demonstrated control over the cell size of SMP foams by varying the molecular weight of the polyol; higher molecular weight resulted in larger cell sizes due to delayed gelling reaction. [21]

In the second class of gas blown foams, a gas phase separates from a supersaturated solution due to changes in pressure and temperature. Inert gasses such as carbon dioxide can be compressed into supercritical fluids at pressures and temperatures above their critical point. Solid-state foaming with an inert gas occurs in two main steps. [22, 23] First, the polymer is saturated with the physical blowing agent, such as supercritical CO_2, at high pressure and at a temperature below the melting temperature

of the polymer. During this step, the T_g of the polymer decreases allowing the material to become rubbery. In the second step, the pressure within the system is decreased to promote a shift in the thermodynamic equilibrium. If the polymer is in the rubbery state, oversaturation of CO_2 will lead to instantaneous nucleation and cell growth. Once the CO_2 evaporates out of the system, the polymer will return to the glassy state, leaving behind a porous structure. These supercritical fluids simultaneously possess fluid characteristics, namely density, and gas properties such as compressibility and mass diffusion, [24] which collectively enable supercritical fluids to solvate polymer networks. Once the supercritical pressure conditions are removed, the dissolved gas expands and blows the polymer into a porous structure. The lack of residual solvents, catalysts, and surfactants make supercritical fluids attractive for creating porous structures for biomedical and tissue engineering applications. [25] Supercritical carbon dioxide has been used to create porous structures from blends of thermoplastic polyurethane and polylactic acid. Because the foam formation occurs below the thermal transition, these scaffolds have a dynamic, contractible porous structure that is proposed for drug delivery systems and wound dressings. [26]

1.3 Use of SMP foams in medical devices

Recent studies have supported the thrombogenic nature of the porous SMP foam morphology. Numerical simulations for the embolization of a patient specific basilar artery aneurysm using SMP foam revealed thrombogenic hemodynamics. [27] Blood within the SMP foam had fluid residence times several orders of magnitude greater than the untreated anatomy. This increase in fluid residence and the decrease in fluid shear

rates imparted by the foam collectively contribute to thrombus forming conditions. These observations are further supported by an in-vitro study by Muschenborn et al, which compared the permeability of reticulated SMP foams to traditional embolic coils. When considering only fluid dynamics, the increased form factor and decreased permeability of embolic SMP foams when compared to coils suggest that SMP foam would create better flow stagnation for eventual thrombus formation. [28]

Several material formulations have been proposed to improve on the clinical implementation of SMP embolic foams. Many embolic foam devices require delivery through a catheter, requiring a delayed expansion profile to prevent the embolic foam from expanding prematurely and binding within the catheter lumen. The metric of "working time" defines the amount of time that a device can be exposed to the aqueous environment of a delivery catheter before it can no longer be delivered or retracted from the target anatomy. Working time can be increased by controlling the bulk material hydrophobicity through monomer selection. Using different stoichiometric amounts of hydrophobic diisocyanate monomers can successfully control the rate of moisture plasticization for embolic foams, leading to controlled working times. [29, 30]

The majority of reported embolic SMP foams are designed to be permanent biostable implants. [19, 31] Although these permanent foams have demonstrated excellent healing responses *in-vivo,* [32] certain tissue engineering applications motivate the development of degradable tissue scaffolds that can be entirely replaced with native tissue. With that goal in mind, Singhal *et al.* successfully developed SMP embolic foams with tunable degradation profiles. [33] This was achieved by incorporating hydrolysable

polyester segments into the foam using polycaprolactone triol. These degradable foams have morphologies and thermo-mechanical properties comparable to non-degradable SMP scaffolds. Similar to working time, the degradation rate of these scaffolds can be tailored by altering the bulk hydrophobicity through diisocyanate monomer selection.

Acute animal studies have been conducted for SMP foam devices used for both peripheral [34] and aneurysm embolization. [35] **Figure 1.3** shows embolic foam plugs used to occlude arterial vessels within a porcine model. [34] These reticulated foam devices demonstrated an average occlusion time of 90 ± 11 s, making them promising candidates for peripheral vessel occlusion.

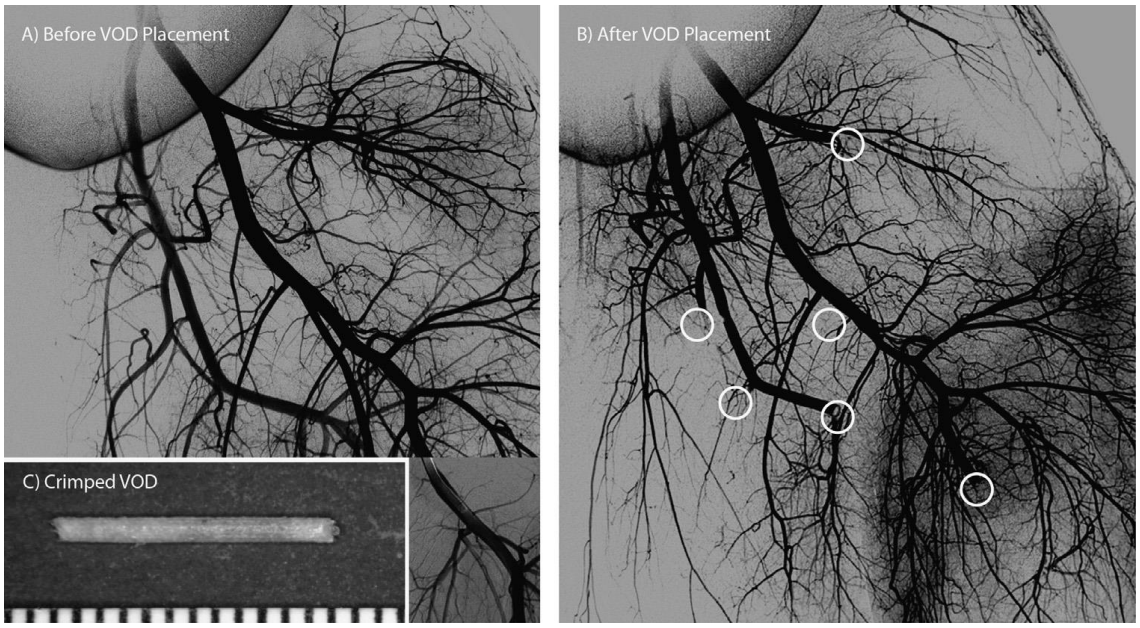

Figure 1.3: Angiograms acquired before (A) and after (B) vessel occlusion with multiple vascular occlusion devices composed of SMP foam. (C) Compressed vascular occlusion device (scale divisions in mm). (Reproduced from [34], with permission from Elsevier.)

Figure 1.4 shows the in-vivo embolization and ex-vivo observation of porcine vein pouch side wall aneurysms occluded with prototype SMP foam-over-wire (FOW) embolization devices. [35] These devices employ the volumetric filling and high surface area advantages of SMP foams with the familiarity of traditional embolic coils to help enable clinical adoption. The acute embolization and stable thrombus formation observed during this study show promising efficacy for these intracranial aneurysm embolization devices.

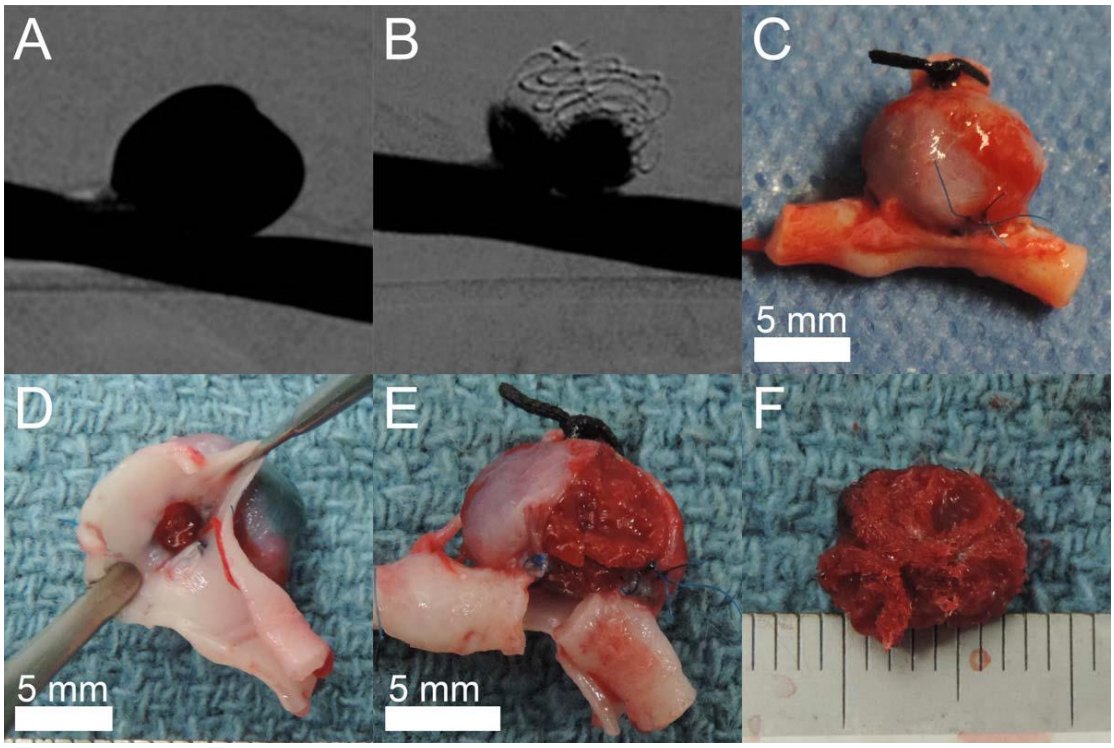

Figure 1.4: (A) Digital subtraction angiography of the aneurysm prior to treatment. (B) Digital subtraction angiography of the aneurysm after implantation of four FOW devices. (C) Explanted aneurysm including parent vessel. (D) Visualization of the explanted aneurysm neck. (E) Partial removal of the explanted aneurysm wall. (F) Thrombus with the implanted devices is stable after removal from the aneurysm. (Reproduced from [35], with permission from John Wiley and Sons.)

1.4 SMP foams for neurovascular aneurysm occlusion

Wilson et al. developed highly crosslinked, amorphous SMPs using aliphatic polyurethanes for use in medical devices.[5] These materials had high recovery stresses due to a high level of crosslinking, tunable T_g's, and good shape recovery.[5] Polyurethanes are an extremely versatile class of polymers that have the capability to be biocompatible, biodegradable, and have tunable mechanical properties.[36] These characteristics make polyurethanes optimal for use *in vivo.* In an effort to increase the surface area, Singhal et al. synthesized the polyurethane SMPs developed by Wilson et al. as foams with low density and high porosity.[19] Open-celled SMP foams provide a substrate for increased cellular infiltration and adhesion, as well as flow stagnation and recirculation zones, resulting in rapid formation of a stable thrombus upon contact with blood.[6, 37] These properties of SMP foams make them ideal for embolization applications, especially in the treatment of aneurysms and vascular malformations.

Aneurysms are a weakening of the blood vessel that result in ballooning of the artery wall.[38] If left untreated, the vessel walls may weaken over time and burst, resulting in hemorrhaging in the subarachnoid space. Subarachnoid hemorrhage (SAH) is a major cause of death for individuals who suffer from aneurysms; half of the patients die within one month of experiencing a SAH.[39] SAH occurs in approximately 300,000 people in the United States each year and most commonly affects individuals between 30 and 60 years of age.[39]

Current treatments include procedures such as surgical clipping and endovascular embolization.[40] Surgical clipping is a highly invasive procedure during which a portion

of the skull is removed while the patient is under anesthesia and a small metal clip is placed on the aneurysm neck to stop blood flow. This method is effective in preventing future bleeding and reopening of the aneurysm, however, long hospital stays and high procedural costs are a major disadvantage. [40] Alternatively, endovascular embolization is a minimally invasive procedure that was first introduced in 1990 in the form of Guglielmi Detachable Coils (GDCs). [41] This technique involves delivering platinum coils to the aneurysm space, via catheter, to cause thrombus formation and subsequently treat the aneurysm. [41] However, treatment with GDCs has shown to have incomplete thrombus formation which leads to recanalization (15%), poor occlusion, and a renewed risk of aneurysm rupture. [42, 43] The International Subarachnoid Aneurysm Trial (ISAT) conducted in 2002 showed treatment with GDCs resulted in 18% fatality, notably because of rebleeding of the aneurysm after treatment and parent-vessel occlusion from the embolic devices. [42] HydroCoil, an alternative product introduced in 2002, consists of an expandable and resorbable acrylic hydrogel around a platinum coil to serve as a space-filling agent and promote improved occlusion. [44] Although these coils had better packing of the aneurysm lumen compared to GDCs (72% verses 32%), procedural complications of device delivery failure and aneurysm rupture during treatment was still a major concern. [45]

1.4.1 Rationale for increasing the hydrophobicity of SMP foams

Endovascular occlusion using SMP foams would provide better occlusion and thrombosis compared to current treatments such that they are more volume filling which results in stable occlusion and minimized recanalization. [38, 46] One drawback of this

approach includes premature actuation of the foam in the catheter under aqueous conditions. [46] Singhal et al. studied the effect of water plasticization of the actuation time of SMP foam along with their biocompatibility. [19, 38] Increasing polymer hydrophobicity changed the water plasticization rate of the foam T_g from 1 to 10 minutes, decreasing the rate of foam actuation and likelihood of premature expansion within the delivery catheter. [47] This is important for clinical applications that require long working times for device delivery and positioning via catheter, where premature SMP actuation would cause the device to lodge in the catheter and prevent delivery of the device, which would add to the total operation time and cost. Thus, achieving increased hydrophobicity to further reduce the rate of actuation was a major focus for the first section of this research proposal.

1.4.2 Rationale behind using fillers in SMP foams

Polyurethane SMP foams lack the ability to intrinsically attenuate x-rays, which is a major disadvantage for their use in endovascular delivery of medical devices using x-ray fluoroscopy. [38, 48] Rodriguez et al. dispersed tungsten microparticles into the foam matrix to achieve radio-opacity. [38] The SMP composites had sufficient visibility via x-ray fluoroscopy, along with improved mechanical properties, to enable endovascular delivery. However, the microparticles only allowed up to 4% by volume loading in the foam matrix before the foams coalesced during the curing process. Nanoparticle use as fillers, instead, has the potential to achieve higher loading concentrations and better dispersion in the foams compared to microparticles, enabling utilization of smaller, less dense devices that are still visible using x-ray.

1.4.3 Rationale behind using silicone surfactants during foaming

Silicone surfactants have been used in polyurethane foam synthesis since the 1950's and their ability to stabilize cell structure has been well documented. [49-51] The surface activity of the surfactant allows for pore stabilization during foam rising and controls the rate of open versus closed cells in the bulk foam. [49] The effect of the chemical structure of the surfactant on foam morphology is a critical aspect of reproducible foam synthesis using gas blowing technique. The use of commercial surfactants has two significant drawbacks for the manufacture of medical SMP foams.

First, they are only available in bulk amounts that far exceed the demand for manufacturing small batches of foam medical devices. The surplus of surfactant compounded with limited shelf life (18 months) results in excessive waste. Second, the current synthesis uses a surfactant from a sole source supplier, making the material dependent on a chemical with questionable long term availability and unknown constituents. Further, two or more surfactants are used during foam synthesis due to the different properties provided by each component. Synthesizing a customized surfactant would eliminate utilization of surfactant combinations, bulk waste generation, and provide a stable surfactant source for long term material synthesis.

CHAPTER II

CHEMICAL MODIFICATION OF SMP FOAMS TO CONTROL THERMO-MECHANICAL PROPERTIES∗

2.1 Introduction

Shape-memory polymers (SMPs) are considered smart materials because they have the capability of switching between a primary and a secondary shape due to thermo-mechanical memory. [12, 52-59] The SMP can be synthesized into a primary shape; when heated above a transition temperature (T_{trans}) an SMP can be programmed *via* mechanical stimulus and set into a secondary shape during cooling. [3, 52-55] Upon the input of an external stimulus, such as heat, the material will actuate to its original shape, thus demonstrating shape-memory behavior. [60, 61] Our group focuses on developing polyurethane shape-memory polymers, specifically, as foams for their potential application in an embolic vascular device for aneurysm treatment. [56-58] A recent review of alternative porous/foam SMP strategies in biomedical applications, such as scaffolds, sponges, and drug-delivery platforms, are elucidated elsewhere. [62]

Aneurysms are a weakening of the blood vessel wall that result in ballooning of the area. [12, 63] They affect about 3 to 5 million people in the United States and up to 300,000 people suffer from a ruptured aneurysm each year. [63] Aneurysm rupture results in a subarachnoid hemorrhage which can lead to severe disability or even death. [64, 65]

∗Reprinted with permission from "Effects of Isophorone Diisocyanate on the Thermal and Mechanical Properties of Shape-Memory Polyurethane Foams," by Sayyeda M. Hasan, Jeffery E. Raymond, Thomas S. Wilson, Brandis K. Keller, Duncan J. Maitland, Macromolecular Chemistry and Physics 2014, 215 (24), 2420-2429. Copyright (2014) John Wiley and Sons.

Current endovascular treatments, such as Guglielmi Detachable Coils, are effective though they have limitations that result in aneurysm rupture and recanalization. [65, 66] We aim to develop a shape-memory polymer foam embolic device that would be deliverable *via* catheter to the aneurysm space and would provide better occlusion and healing than the current treatments. We selected a polyurethane chemistry approach to SMP foam generation, as urethanes are well-known for their biocompatibility, versatility, and tunable mechanical properties. [36, 67-71] Previously, our group has developed aliphatic shape-memory polyurethane foams for use in embolic devices; however, a prominent issue with these systems has been the depression of the glass transition temperature (T_g) in aqueous environments. [57] Water molecules serve as plasticizing agents, enabling mobility of the polymer chains at reduced temperature. It has been shown that the effect in urethanes is due to interference of water with inter-chain hydrogen bonding. [57, 72-74] This causes a significant decrease in the T_g, which results in premature foam actuation and a reduction in working time for the device. [75] In order to deliver the foam from the catheter to the aneurysm the foam must maintain its secondary, programmed shape for a considerable length of time to ensure ease/completion of delivery. However, water plasticization may cause the foams to actuate too quickly in the catheter, presenting a hurdle in foam-over-wire delivery. Singhal et al. synthesized SMP foams using various combinations of hexamethylene diisocyanate (HDI), trimethyl hexamethylene diisocyanate (TMHDI), hydroxypropylethylenediamine (HPED) and triethanolamine (TEA) to achieve a similar goal of increasing working time of the embolic device;

however, those efforts attained *ca.* ten minutes of working time before the SMP foam began to actuate. [57]

The goal our research in this study was to elongate the working time beyond ten minutes by further increasing the hydrophobicity and glass transition, hence the actuation rate of the SMP foams, by incorporating isophorone diisocyanate (IPDI) into the foam chemistry. In this paper we develop ultra-low density SMP foams and determine their chemical and mechanical properties, as well as, study their actuation times in an aqueous environment (range: 4 min. to > 20 min.).

2.2 Materials and methods

2.2.1 Synthesis and post-processing

N,N,N',N'-Tetrakis(2-hydroxypropyl)ethylenediamine (HPED, 99%; Sigma-Aldrich Inc.), triethanolamine (TEA, 98%; Sigma-Aldrich Inc.), trimethyl-1,6-hexamethylene diisocyanate, 2,2,4- and 2,4,4- mixture (TMHDI, TCI America Inc.), isophorone diisocyante (IPDI, 98%; Sigma-Aldrich Inc.), DC 198 (Air Products and Chemicals, Inc.), DC 5943 (Air Products and Chemicals, Inc.), T-131 (Air Products and Chemicals, Inc.), BL-22 (Air Products and Chemicals, Inc), Enovate 245fa Blowing Agent (Honeywell International, Inc.) and deionized (DI) water (> 17 M Ω cm purity; Millipore water purifier system; Millipore Inc.), Phosphate Buffered Saline (1X) (0.0067M PO_4) (HyClone Laboratories, Inc) were used as received.

SMP foam was synthesized using the three-step protocol mentioned in previous work. [56, 57] First, an isocyanate (NCO) prepolymer was synthesized with appropriate molar ratios of HPED, TEA, TMHDI, and IPDI. These prepolymers were allowed to

react for 2 days with a temperature ramp from room temperature to 50°C and back to room temperature. Next, a hydroxyl (OH) mixture was blended with the remaining molar equivalants of HPED and TEA. This mixture also contained DI water, and catalysts. Finally, the NCO prepolymer and the OH mixture were combined in the foam cup along with surfactants, DC 198 and DC 5943, and Enovate. This mixture was allowed to mix in a FlackTek speedmixer (FlackTek, Inc., Landrum, SC) and poured in the foam bucket. The foam was allowed to cure at 90°C for 20 minutes before being allowed to cool down to room temperature for further processing. **Table 2.1** shows the weight percent of each component used for foam synthesis and **Figure 2.1** shows the corresponding molecular structure of each monomer.

Post-processing for the foam consisted of mechanically crimping the foams by heating them to 90°C and compressing them using the Carver Press (Carver, Inc., Wabash, IN). Once cooled, the foams were acid etched using 0.1N HCl for 2 hours, under sonication. After this step, the foams were sonicated in isopropyl alcohol (IPA) for two 15 minute cycles. The foams were then washed with a 20:80 Contrad:Reverse Osmosis (RO) water solution for four 15 minute cycles. Finally, the Contrad solution was rinsed out of the foams and they were sonicated in RO water for two 15 minute cycles. The foams were allowed to dry overnight at 50°C under vacuum before characterization.

Table 2.1: Composition of foams using trimethylhexamethylene diisocyanate (TMHDI) and isophorone diisocyanate (IPDI) for the isocyanate component of the urethane foam. Three foam batches were synthesized and the average weight percent was determined for all batches.

Sample	TMHDI [wt%]	IPDI [wt%]	HPED [wt%]	TEA [wt%]	Water [wt%]	T-131 [wt%]	BL-22 [wt%]	DC 198 [wt%]	DC 5943 [wt%]	Enovate [pph]
0% IPDI	66.78 ± 0.5	0	17.10 ± 0.03	5.74 ± 0.02	2.35 ± 0.01	0.26 ± 0.001	0.64 ± 0.005	2.54 ± 0.02	4.59 ± 0.02	14.89 ± 0.01
5% IPDI	63.62 ± 1	3.54 ± 0.5	17.08 ± 0.2	5.33 ± 1	2.39 ± 0.100	0.26 ± 0.01	0.64 ± 0.05	2.55 ± 0.01	4.59 ± 0.02	14.91 ± 0.2
10% IPDI	59.82 ± 0.05	7.04 ± 0.01	17.03 ± 0.01	5.72 ± 0.01	2.34 ± 0.01	0.26 ± 0.001	0.64 ± 0.001	2.56 ± 0.01	4.59 ± 0.02	14.95 ± 0.02
15% IPDI	56.37 ± 0.05	10.52 ± 0.01	17.01 ± 0.02	5.71 ± 0.02	2.34 ± 0.01	0.26 ± 0.002	0.64 ± 0.005	2.54 ± 0.05	4.60 ± 0.01	14.98 ± 0.03
20% IPDI	53.74 ± 0.01	14.20 ± 0.01	16.23 ± 0.01	5.45 ± 0.01	2.34 ± 0.02	0.26 ± 0.002	0.64 ± 0.005	2.57 ± 0.01	4.58 ± 0.01	15.06 ± 0.03

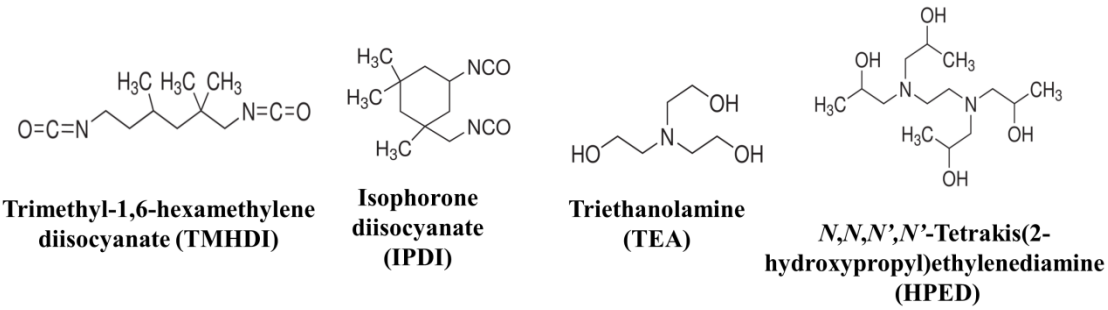

Figure 2.1: Molecular structures of the hydroxyl and isocyanate monomers used during foam synthesis.

Neat polymer samples were cast with measured amounts of HPED, TEA, TMHDI, and IPDI in rectangular aluminum molds. These were non-porous polymers that did not utilize any catalysts, surfactants, or blowing agents during synthesis. The solution was mixed for 1 minute using the speedmixer and poured into the molds, which were sealed with a Teflon stopper. The neat polymer containing molds were placed in a pressurized environment of 60 PSI for 3 hours. Next, the samples were cured in an oven with the temperature ramped to 120°C at 20°C h^{-1}. The polymers were held at 120°C for 2 hours after which they were allowed to cool to room temperature. **Table 2.2** shows the weight percent of each monomer used for non-porous polymer synthesis.

Table 2.2: Composition of neat polymers following the same schematic synthesis as that of the foams (Table 1). No foaming additives such as surfactants, catalysts, physical, or chemical blowing agents were added.

Sample	TMHDI [wt%]	IPDI [wt%]	HPED [wt%]	TEA [wt%]
0% IPDI	61.66	0	28.71	9.63
5% IPDI	58.47	3.25	28.67	9.61
10% IPDI	55.28	6.50	28.62	9.60
15% IPDI	52.12	9.75	28.55	9.57
20% IPDI	48.96	12.97	28.51	9.56

2.2.2 Chemical and mechanical characterization

2.2.2.1 Density and cell structure

Foam cubes were cut using a resistive wire cutter from top, middle, and bottom of the foam as required by at ASTM standard D-3574. Length, width, and height of the cube was measured, mass of the sample was recorded, and density was calculated in $g \cdot cm^{-3}$. Cell structure was determined by cutting thin slices of the bulk foam in the axial and transverse direction. The samples were mounted onto a stage and sputter coated for 60 seconds at 20 mA with gold using Cressington Sputter Coater (Ted Pella, Inc., Redding, CA). The samples were then visualized using Joel NeoScope JCM-5000 Scanning Electron Microscope (SEM) (Nikon Instruments, Inc., Melville, NY) at 15x magnification under high vacuum and 5-10 kV current.

2.2.2.2 Fourier-transform infrared (FTIR) spectroscopy

Thin foam samples were cut (2-3 mm) and the spectra was collected using Bruker ALPHA Infrared Spectrometer (Bruker, Billerica, MA). Thirty-two background scans of the empty chamber were taken followed by sixty-four sample scans of the various foam compositions. FTIR spectra was collected in absorption mode at a resolution of 4 cm^{-1}. OPUS software (Bruker, Billerica, MA) was utilized to subtract the background scans from the spectra and also to conduct a baseline correction for IR beam scattering and an atmospheric compensation to remove any peaks acquired due to carbon dioxide. Each composition was measured three times for duplicity.

2.2.2.3 Differential scanning calorimetry (DSC)

Foam samples (3-8 mg) were used for T_g analysis and were stored in a dry container with desiccant. A Q-200 DSC (TA Instruments, Inc., New Castle, DE) was used to attain the thermogram for our foams. The first cycle consisted of decreasing the temperature to -40°C at 10°C·min^{-1} and holding it isothermal for 2 minutes. The temperature was then increased to 120°C at 10°C ·min^{-1} and held isothermal for 2 minutes. In the second cycle, the temperature was reduced to -40°C at 10°C·min^{-1}, held isothermal for 2 minutes, and raised to 120°C at 10°C·min^{-1}. T_g was recorded from the second cycle based on the inflection point of the thermal transition curve using TA instruments software. This test was conducted 5x per foam composition for duplicity. The aluminum tin was not vented during this step.

2.2.2.4 Dynamic mechanical thermal analysis (DMA)

DMA of the foam compositions were conducted to determine changes in T_g as a function of storage modulus. Dynamic temperature sweeps, ranging from 25°C to 150°C, were conducted on the dry foam compositions using Triton Technology (TT) DMA (Mettler Toledo International, Inc., Columbus, OH). The frequency was set to 1 Hz, dynamic force to 0.1N, and the ramp rate to $1°C \cdot min^{-1}$. Cylindrical foam samples with diameters of 6 mm and a heights of 5 mm were used. Data points were collected every 20 seconds. Dynamic shear storage modulus (E'), dynamic shear loss modulus (E"), and tan δ (E"/ E') was recorded using the Titron Laboratory software (Mettler Toledo International, Inc., Columbus, OH). The peak of the tan δ curve and the inflection point of E' indicated T_g for the dry foam samples.

2.2.3 Characterization of hydrophobicity and foam actuation

2.2.3.1 Contact angle

Hydrostatic contact angle measurements on neat polymer samples were done using KSV CAM-2008 Contact Angle Analyzer (KSV Instruments, Ltd., Helsinki, Finland). A 5 μL drop of DI water was placed on the sample surface. The drop was allowed to reach equilibrium for 60 seconds and the contact angle was measured using an Attension Tensometer and the Attension Theta software package (Biolin Scientific, Stockholm, Sweden). Contact angles were collected (n = 3) and the average was presented as the water contact angle for each neat polymer composition.

2.2.3.2 Phase transition rates in water

Foam samples (3-8 mg) were submerged in RO water at 50°C for 5 minutes to allow full plasticization. After the samples were removed from water, they were pressed dry with Kim Wipes (Kimberly-Clark Professionals, Roswell, GA), weighed, and placed in an aluminum pan sealed with an aluminum lid that was vented. Q-200 DSC was used to cool the samples to -40°C, hold them isothermal for 2 minutes, and heat them to 80°C at $10°C \cdot min^{-1}$. TA instruments software was used to generate the thermogram and acquire the T_g, after water plasticization, using the average inflection point of the thermal transition of multiple measurements (n = 5).

2.2.3.3 Immersion DMA

Cylindrical foam samples with a diameter of 6 mm and a height of 5 mm were used in this procedure. The samples were crimped using the Carver Press to a height of 0.8 mm. TT DMA was used to collect the kinetic thermogram of various foam compositions at 37°C and 50°C. For each temperature, the samples were submerged in a PBS bath, to mimic physiological osmolarity (pH = 7), and changes in storage modulus (E') were recorded using the TT DMA software. The frequency was set to 1.0 Hz, dynamic force to 0.1N, and each run was carried out for 20 minutes. This test was conducted in triplicate per foam composition. The inflection point between E'_{onset} and E'_{end} corresponded to the actuation time for the sample.

2.2.3.4 Volume recovery and expansion

Cylindrical foam samples with a diameter of 6 mm and a height of 1 cm were cut. A 203.20 μm diameter nickel-titanium (Nitinol) wire (NDC, Fremont, CA) was

inserted through the center of the sample along its length to serve as a stabilizer. The foam samples were radially compressed to their smallest possible diameter using ST 150-42 stent crimper (Machine Solutions, Flagstaff, AZ) by heating the material to 100°C, holding it isothermal for 15 minutes, and programming the foams to the crimped morphology. Initial foam diameter was measured and recorded for each sample using Image J software (NIH, Bethesda, MD). The foams were placed in a water bath at 50°C, removed after 20 minutes, and allowed to cool to room temperature. The final diameter of the samples was measured and recorded using Image J software. Volume expansion was calculated using Equation 2.1 and volume recovery was calculated using Equation 2.2.

$$(Volume\ expansion = \left(\frac{\text{Recovered diameter}}{\text{Compressed diameter}}\right)^2) \quad (2.1)$$

$$(Volume\ recovery = \left(\frac{\text{Recovered diamater}}{\text{Original diameter}}\right)^2 * 100\%) \quad (2.2)$$

2.3 Results and discussion

2.3.1 Chemical and mechanical characterization

2.3.1.1 Density and cell structure

The measured foam densities are provided in **Table 2.3**. Multiple foam batches maintained ultra-low densities which were consistently c*a.* 12.5 mg·cm^{-3}. With batch-to-batch standard deviations ranging from 0.1 to 0.3 mg·cm^{-3}, our method allows for reproducible synthesis of uniform-celled SMP foams.

Analysis of the foam morphology with SEM revealed homogenous cells throughout different compositions, as depicted by **Figure 2.2**. It was evident that each

foam composition consists of both open and closed-cell pores and mixed open and closed-cell pores. This would effectively provide initial reticulation of the foam and aid the removal of surfactants and catalysts during the cleaning process. Furthermore the uniform cross-linked foam network suggests good shape memory behavior as explained by Singhal et al. [56, 57]

Table 2.3: Summary of key physical properties of various foam compositions.

Composition	Density ($g \cdot cm^{-3}$)	Dry T_g (°C)	T'_{onset} (°C)	$T'_{1/2}$ (°C)	Tan δ_{max} (°C)
0% IPDI	0.0122 ± 0.0002	62 ± 1	55 ± 2	70 ± 2	105 ± 2
5% IPDI	0.0119 ± 0.0002	64 ± 0.5	61 ± 1	78 ± 2	111 ± 1
10% IPDI	0.0129 ± 0.0005	65 ± 0.5	65 ± 2	81 ± 3	118 ± 2
15% IPDI	0.0132 ± 0.0001	67 ± 0.2	71 ± 1	88 ± 2	125 ± 2
20% IPDI	0.0122 ± 0.0001	71 ± 2	76 ± 0.5	92 ± 2	131 ± 1

2.3.1.2 FTIR

Selected FTIR spectral regions for the various foam compositions are presented in **Figure 2.3**. The hydrogen-bonded urethane C=O stretch (1698 cm^{-1}) confirms a polyurethane system, (**Figure 2.4a**). [76, 77] A small amount of hydrogen-bonded urea can be observed on the urethane C=O shoulder (1647 cm^{-1}) due to the reaction of isocyanates with water during the foaming step (Figure 2.4a). [76] The amine a broad stretch (centered at 3330 cm^{-1}) represents a combination of secondary and tertiary amine and is readily

observed in all systems (Figure 2.4b). [77] The C-H peaks around 1465 cm^{-1} indicate a strong presence of methyl groups contributed from TMHDI and IPDI in each foam composition (Figure 2.3). [57] Lastly, the C-N peak (1307 cm^{-1}) is indicative of both IPDI and TMHDI incorporation into the matrix (Figure 2.4c). The C-N stretch (normally 1020 to 1250 cm^{-1}) is shifted to higher wavenumbers near-by methyl constituencies contributing to higher energy requirements for excitation. There is an initial C-N shoulder observed for 0 IPDI, however and increase in the peak intensity with additional IPDI incorporation implies slightly higher reaction efficiency than TMHDI in these formulations.

2.3.1.3 DSC

Thermal analysis of the foams shows an increase in T_g with higher IPDI content (Table 2.3 and **Figure 2.5**). The shift in T_g is significant from 62°C for the 100% TMHDI control to 71 °C for 20% IPDI, which has the highest concentration of IPDI in the series. The increase in T_g is due to the increase in foam stiffenss provided by the ring moiety of IPDI. Figure 2.5 shows the shift in T_g with increasing IPDI content. This indicates that the matrix is more constrained with additional IPDI content, delaying thermal actuation temperatures (*e.g.* T_g), which is reasonable given the sterics of the IPDI ring in comparison to semi-linear TMHDI. [78, 79]

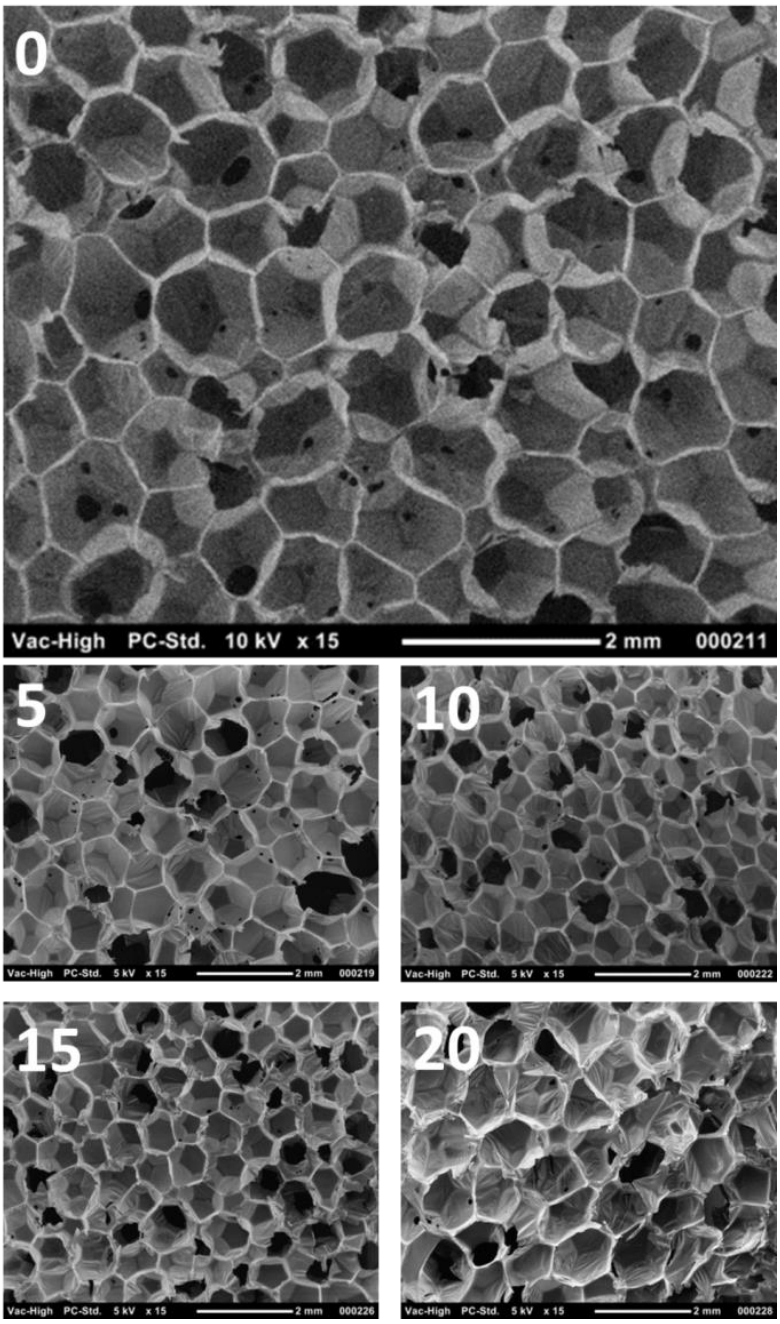

Figure 2.2: SEM images of various foam compositions at 15x magnification. Images 0, 5, 10, 15, and 20 represent 0% IPDI, 5% IPDI, 10% IPDI, 15% IPDI, and 20% IPDI, respectively.

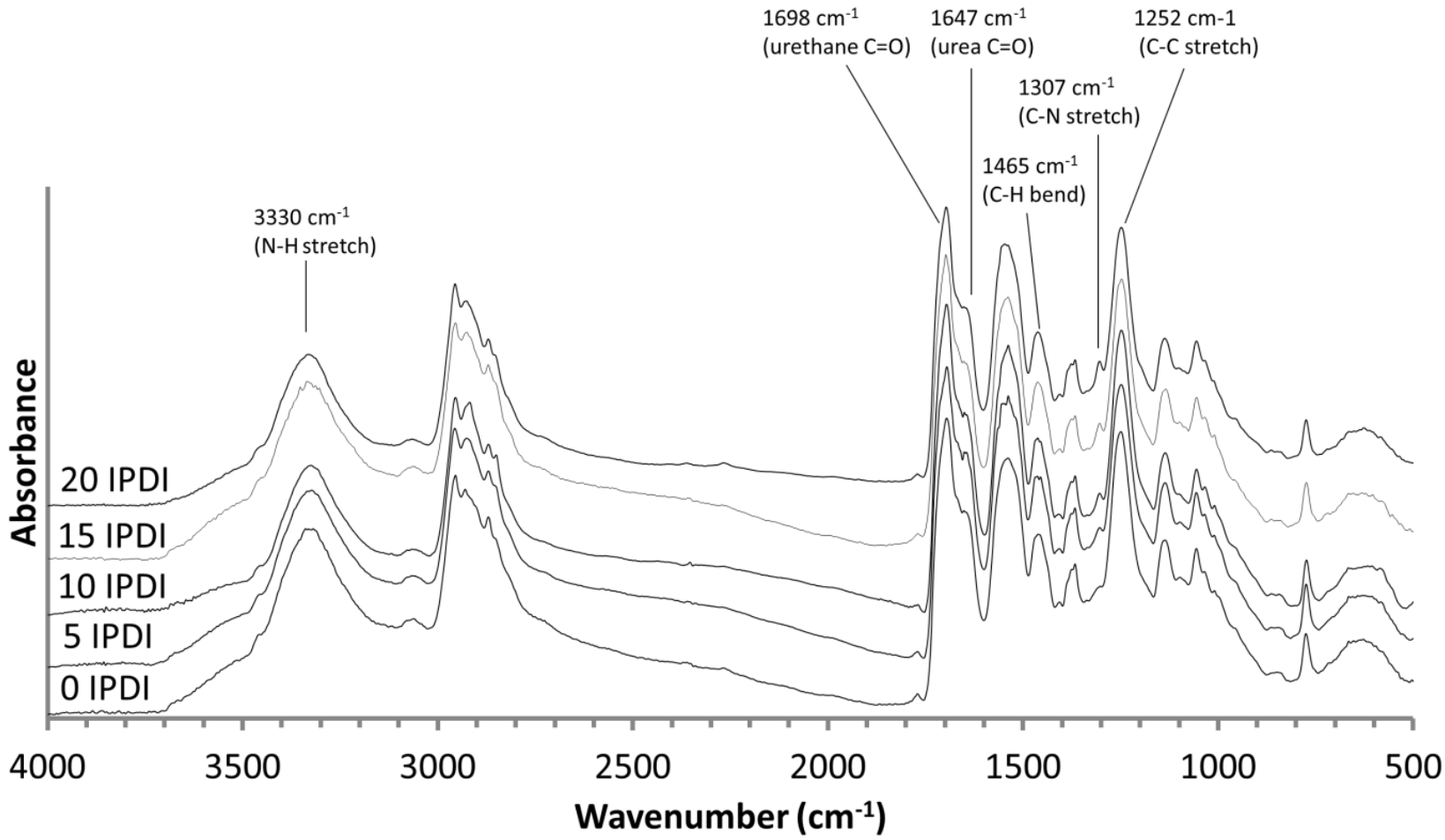

Figure 2.3: FTIR spectra of the IPDI-TMHDI SMP foam series.

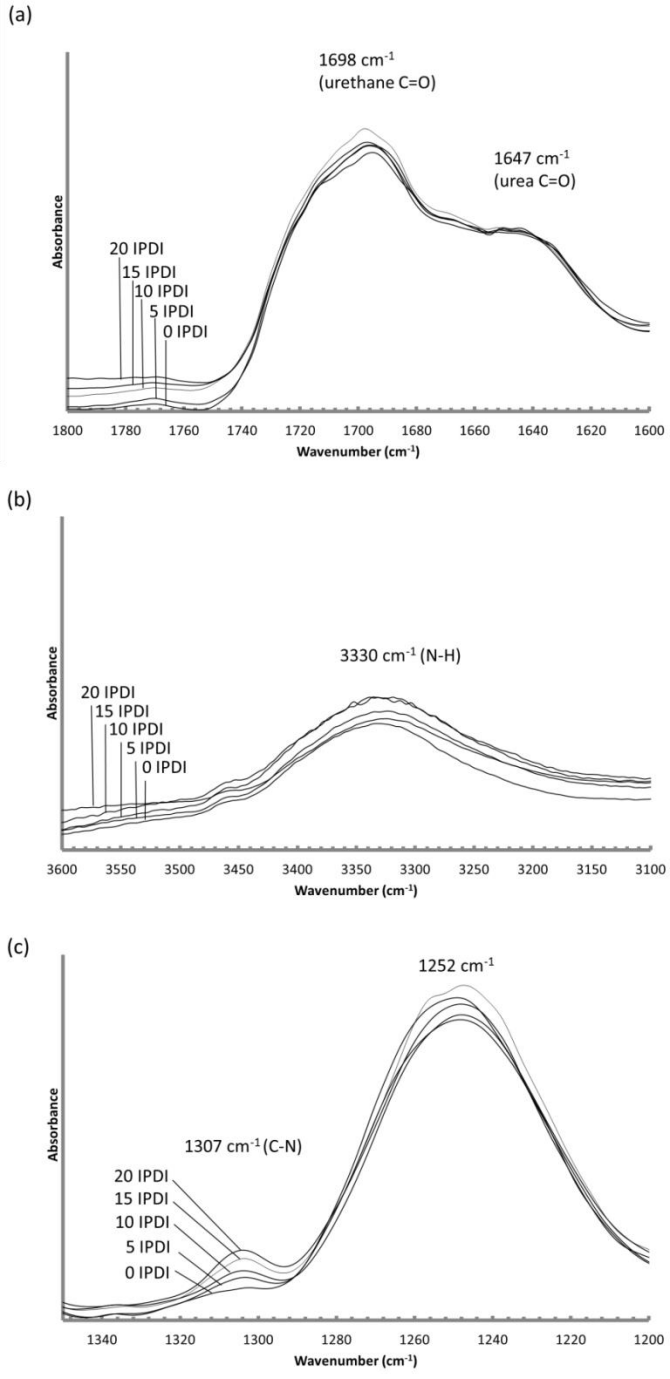

Figure 2.4: FTIR absorbance spectra for (a) hydrogen-bonded urethane and urea. (b) secondary and tertiary amines in SMP systems and (c) C-N groups contributed from IPDI and TMHDI.

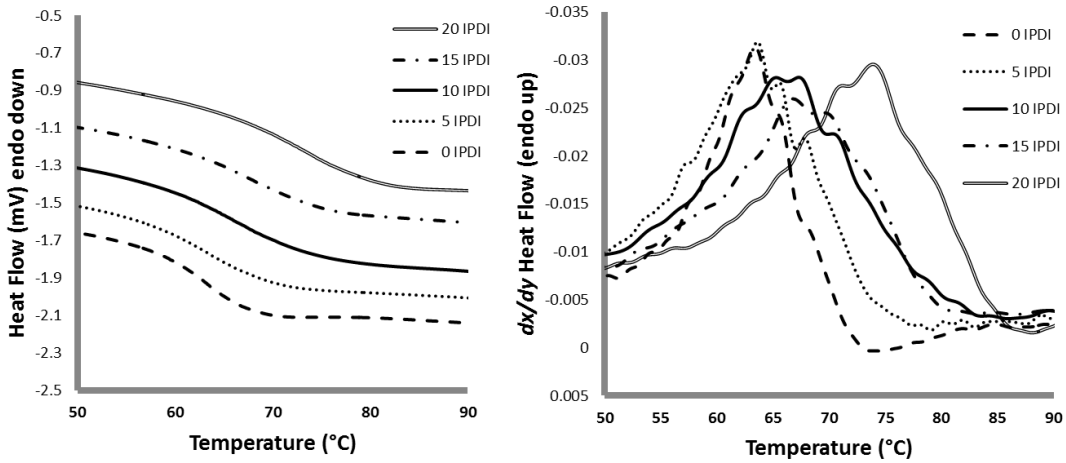

Figure 2.5: DSC thermogram of the IPDI-TMHDI SMP foam series (primary axis) and heat flow derivative (secondary axis). Glass transition temperature increases with increasing IPDI content.

2.3.1.4 DMA

Thermal analysis of the foams using DMA provided relationships between glass transition temperatures as IPDI content that are comparable to the DSC findings (**Figure 2.6)**. Maximum softening rate temperatures ($E'_{1/2}$) increased from 70°C to 91°C when transitioning from 0% IPDI to 20% IPDI. A transition from 105°C to 130°C for tan δ_{max} was similarly observed with increased IPDI content, Table 2.3.

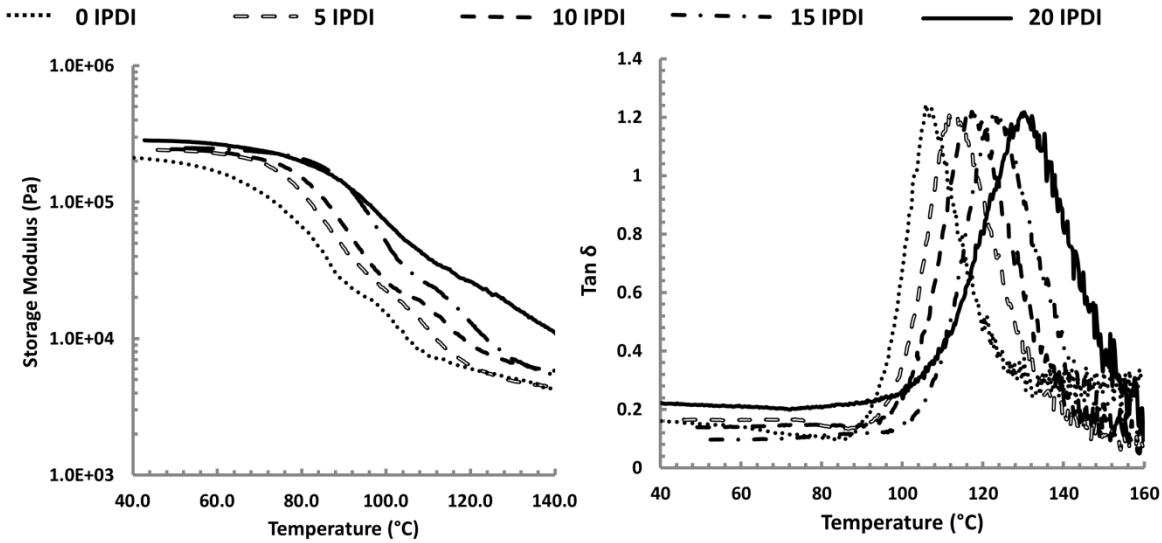

Figure 2.6: Storage modulus (E') and tan δ curves of the IPDI-TMHDI SMP foam series.

2.3.2 Characterization of hydrophobicity and foam actuation

2.3.2.1 Contact angle

Hydrostatic contact angles of the neat/non-porous polymer networks (**Table 2.4**) make evident that hydrophobicity (*e.g.* contact angle) is increasing with IPDI content. [80, 81] Ultimately the increase in contact angle (76° → 98°) with increased IPDI content indicates that the constrained, ring containing moiety is significantly reducing the rate of water intercalation into the matrix and is an appropriate formulation component for tuning kinetics from solvent plasticization.

2.3.2.2 Phase transition rates in water

For all of the SMP formulations investigated, actuation can be induced by conventional thermal means (heat to T_g) or at lower temperatures with moisture based plasticization. [57] Wet T_g's (from DSC) are provided in Table 2.4. For our entire array of foam compositions there is a significant decrease in T_g after exposure to RO water when compared to dry foams. For example, there is a drop in T_g from 62°C to 30°C for the control (0% IPDI) upon introduction to water. For the remaining foams containing IPDI, there is a trend of higher transition temperature as we increase the IPDI content, even after exposure to water. This displays that the hydrophobicity and increased steric restrictions to movement introduced with IPDI incorporation can successfully allow for application-tailored glass transition temperatures in the range of 30-57°C.

Table 2.4: Summary of the foam properties related to actuation and working time.

Composition	Dry Tg (°C)[a]	Wet T_g (°C)	Contact angle (°)	Volume Expansion (x)	Volume Recovery (%)	Working time at 37°C (sec)[b]	Working time at 50°C (sec)[b]
0% IPDI	62 ± 1	30 ± 1	76 ± 1	66 ± 8	148 ± 25	246 ± 33	54 ± 20
5% IPDI	64 ± 0.5	33 ± 1	80 ± 1	57 ± 9	105 ± 9	333 ± 59	58 ± 9
10% IPDI	65 ± 0.5	39 ± 3	84 ± 0.3	46 ± 8	88 ± 7	> 1200	81 ± 25
15% IPDI	67 ± 0.2	53 ± 1	94 ± 1	46 ± 8	87 ± 5	> 1200	135 ± 23
20% IPDI	71 ± 2	57 ± 0.5	98 ± 0.3	39 ± 8	83 ± 23	> 1200	135 ± 22

[a] T_g dry reproduced from Table 2.3 for comparative purposes.

[b] Working time defined as the time when the foam is exposed to an aqueous environment the catheter to the time when it is no longer retractable.

2.3.2.3 Immersion DMA

The working times derived from immersion DMA are shown in Table 2.4. The range of working times are 5 minutes, for 0 IPDI, to no actuation in 37°C PBS as IPDI concentrations are increased in the SMP foams (**Figure 2.7)**. The decay in storage modulus was the indicator for actuation and for foam compositions above 5 IPDI, there was no decay in E' during the 20 minute kinetic run. This displays that at body temperature the higher 10 IPDI, 15 IPDI and 20 IPDI foams will yield a working time greater than 20 minutes, though analysis at 50°C indicates rapid actuation for all systems Overall, the foams with higher IPDI content yielded a longer working time due to delayed actuation, though all systems are readily actuated in 50°C water.

2.3.2.4 Volume recovery and expansion

The volume recovery of the foams can be readily observed in **Figure 2.8**. The control samples of 0 IPDI experienced *ca.* 66-fold volume expansion upon submersion in 70°C RO water and higher IPDI compositions had volume expansions below 50-fold, Table 2.4. These results indicate that a degree of constraint exists with increased IPDI content, both in terms of ultimate compression above T_g and recovery, which is reasonable given the mechanical and hydrophobicity trends in our systems. Despite a decreased volume expansion, all foam samples recovered to 80%+ in water, Table 2.4. In terms of application, we envision these systems as application-tunable materials where one may select from 5% to 15% content based on working time needs. Also a fortuitous finding in terms of application, all systems have actuation times *ca.* 1-2 min. at 50°C; this means that, should a surgical application require rapid foam expansion after

placement/working time considerations are met, a rapid warm water actuation is possible.

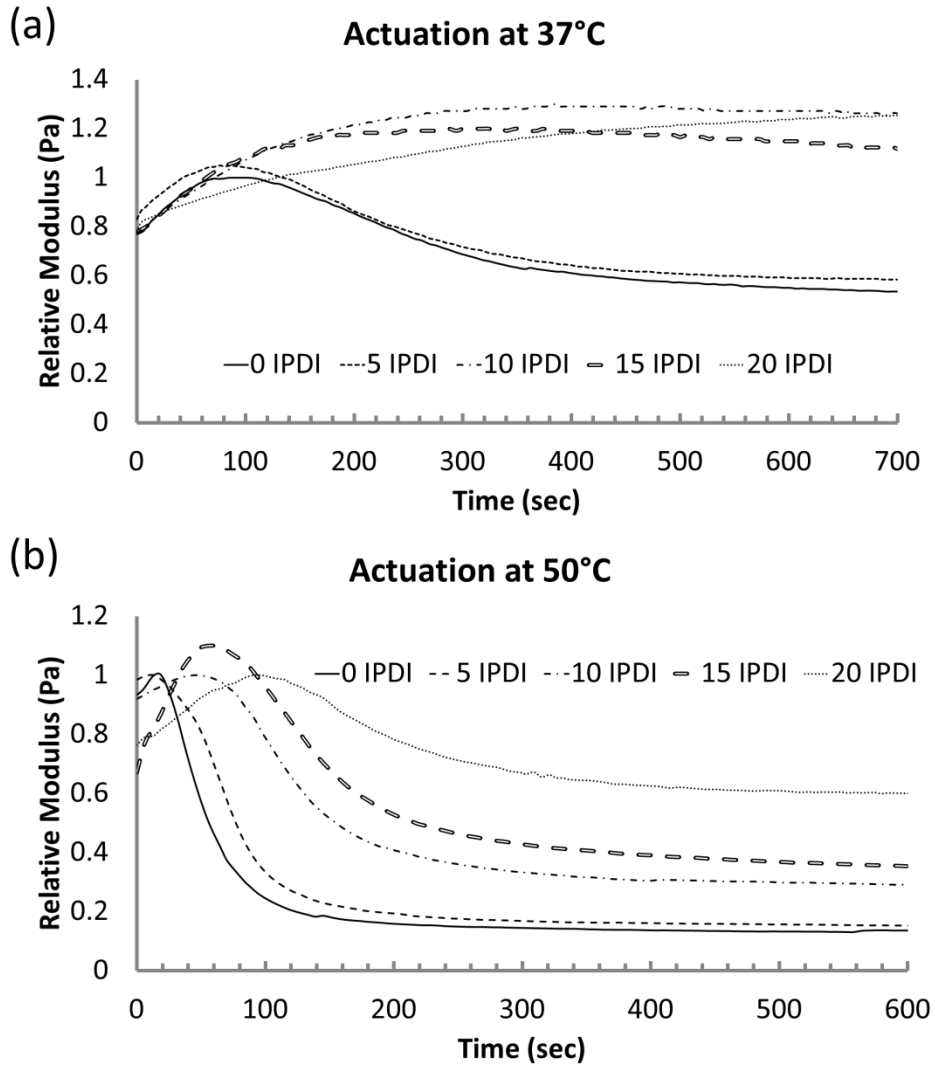

Figure 2.7: Actuation of the SMP foam depicted by a decay in E' in (a) 37°C and (b) 50°C PBS bath.

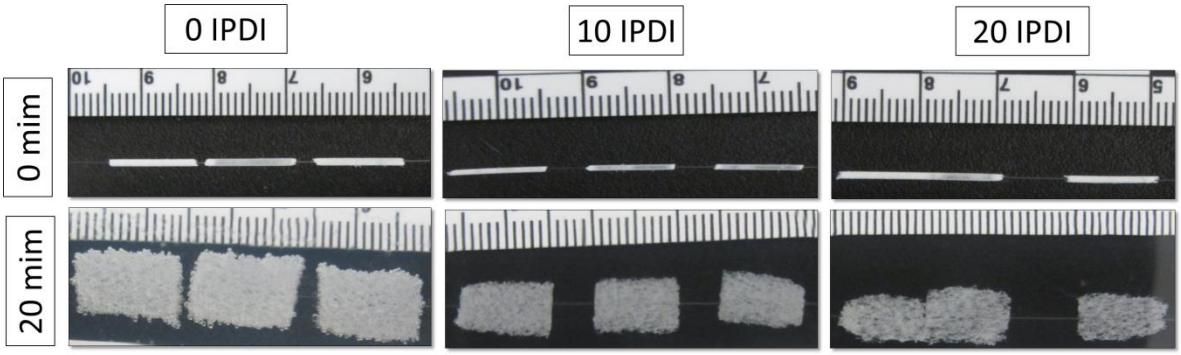

Figure 2.8: Volume expansion images for 0 IPDI, 10 IPDI, and 20 IPDI respectively. As IPDI content increases in the foams, the shape recovery to full expansion decreases.

An *ad hoc* assessment of surface availability was made using ChemDraw 13 for MM2 energy minimized 3D renderings of the space filling models of various monomer couplings. Given the differences observed in thermal, mechanical, kinetic and recovery response of these systems despite the similar empirical formulas of the system precursors, it is reasonable to have an *ad hoc* discussion of TMHDI and IPDI availability to when linked to TEA. Energy minimized structures of TEA bound to TMHDI versus IPDI revealed significantly different solvent availability (**Figure 2.9)**. Image 2.9a displays a urethane structure composed of TEA and IPDI that has a lower availability to the ternary amine and the urethane linkages (*e.g.* the non-aliphatic, polar regions of the structure) than that of the TEA and TMHDI structure (Figure 2.9b). In brief, the constrained nature of the IPDI cyclohexyl moiety does not allow the free rotation of the bonds along a methylene backbone (as in TMHDI) and enforce limited expansion, even with some water association at the polar regions.

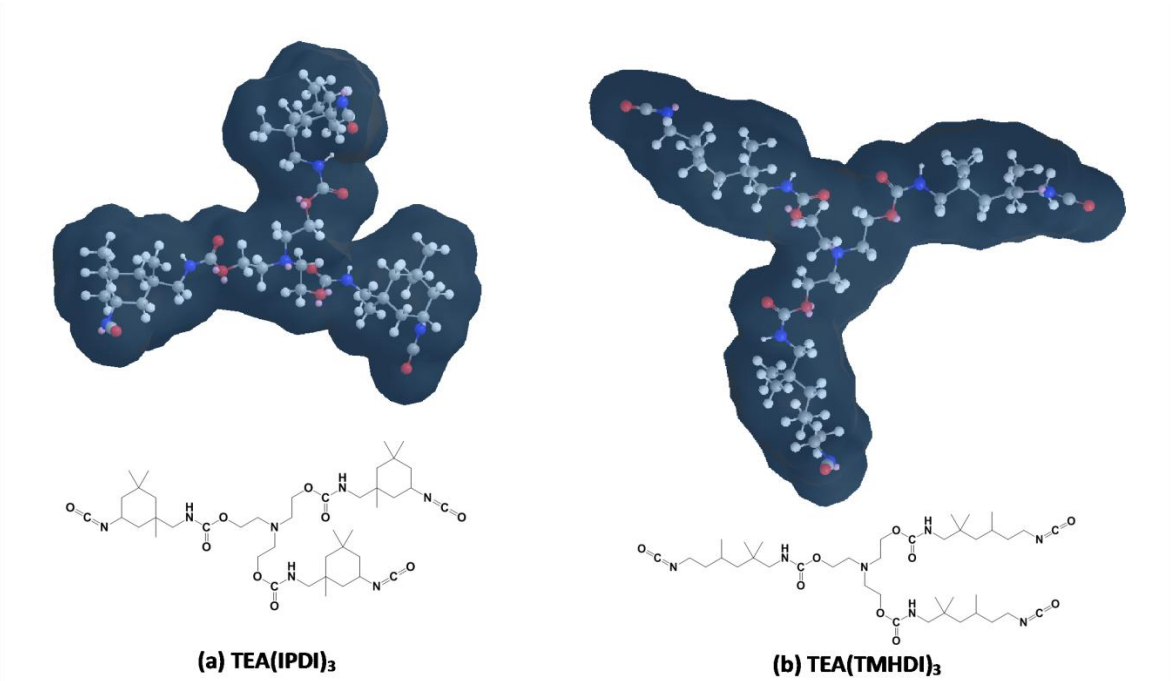

Figure 2.9: Molecular geometries and solvent interaction for (a) TEA(IPDI)3 and (b) TEA(TMHDI)3. The chains are more tightly packed due to restricted movement from IPDI in (a) while appear to have free rotation due to the linear backbone of TMHDI in (b).

Overall, incorporation of IPDI into our shape-memory foams increased the actuation time and therefore provided an elongated working time for the foams (Table 2.4). The glass transition temperature of the foams also increased with greater IPDI content due to the added stiffness from the IPDI aliphatic C-C ring (Figure 2.1 and Figure 2.5). As the material became stiffer, it was more difficult for the polymer chains to achieve mobility and become rubbery. Therefore higher temperatures were required to allow the material to transition from the glassy to the rubbery state. Using foams with higher IPDI content, such as 10 IPDI, can ensure that the crimped foam will not expand

immediately at physiological temperature while being delivered through the catheter. However, passive actuation will eventually occur once the foam has been deployed in the aneurysm (Figure 2.7). One tradeoff to consider is the percent volume recovery for the foam. Clearly, 10 IPDI only yields 46% volume recovery at 70°C, which indicates that the foam will passively actuate even slower at physiological temperature as shown in Table 2.4. However, upon reaching full actuation, the volume expansion of 88% will ensure full occlusion of the aneurysm space (Figure 2.8). Additionally, the computational solvent interaction images (Figure 2.9) suggest poor solvent interaction for urethanes synthesized with IPDI compared to TMHDI which supports decreased volume recovery of the foams in water. Nevertheless, the higher working time will be beneficial during foam delivery and the shape filling properties of the foam will be advantageous to promote occlusion and block blood flow to the aneurysm.

2.4 Conclusions

We have successfully synthesized shape-memory polymer foams with slower actuation times by incorporating isophorone diisocyanate (IPDI) into the foam matrix. The foams containing 10% IPDI remain crimped during the twenty minute test interval at physiological temperature, thus providing sufficient working time for the foam to be delivered to the aneurysm site without premature actuation in the catheter. Additionally, these systems showed rapid actuation (1-2 min.) under warmed water conditions that may serve as a potential for rapid actuation as surgical conditions require. Higher IPDI content for the foams also resulted in an increased glass transition temperature and foam hydrophobicity which helps elongate the working time and delay water plasticization of

the material. One drawback of delayed actuation was the decrease in volume recovery of the foam; however, all systems displayed total volume expansion to 80%+ of the pre-crimped state. We discuss these effects in terms of the molecular effects of IPDI incorporation, such as poor solvent interaction, decreased subunit mobility and the resultant mechanical, thermal and hydrophilic response.

CHAPTER III

INCORPORATING TUNGSTEN NANOPARTICLES TO INDUCE RADIOPACITY*

3.1 Introduction

Polymers have been utilized as medical implants for the last 30 years with much success. [48, 82] Some natural and synthetic polymers are known to be biocompatible, indicating their ability to perform with appropriate host response for biomedical applications. [82] These biocompatible polymers, commonly referred to as polymeric biomaterials, are known to have a wide range of applications due to their wide availability, ease of manufacturing, and tunable mechanical and thermal properties. [82, 83] Some of the most common biomaterials include polyethylene (PE), polyurethane (PU), polytetrafluoroethylene (PTFE), polymethylmethacrylate (PMMA), poly(lactic acid) (PLA), and poly(glycolic acid) (PGA). [82, 83], which currently have found uses as biodegradable sutures and fixation screws. While these materials can be fabricated into complex shapes and are available in a wide range of compositions, most tend to have low tensile strength and Young's modulus for applications that require mechanical robustness, such as orthopedic implants. [82] Additionally, polymers have similar properties to that of soft tissue, limiting their radiological detectability. [82, 84] Most polymeric materials lack radiopacity because their elements possess low electron density

* Reprinted with permission from "Tungsten-loaded SMP foam nanocomposites with inherent radiopacity and tunable thermo-mechanical properties," by Sayyeda M. Hasan, Garrett Harmon, Fang Zhou, Jeffery E. Raymond, Tiffany P. Gustafson, Thomas S. Wilson, Duncan J. Maitland, Polymers for Advanced Technologies 2015. Copyright (2015) John Wiley and Sons.

and low specific gravity. [48, 85, 86] Several steps have been taken to improve radiopacity of polymers by incorporating heavy-metal fillers as physical mixtures, attaching heavy-metal salts to the polymer backbone *via* chelation, and by covalently binding radiopaque elements to monomers prior to their polymerization. [48, 85]

Radiopaque polymeric blends consisted of heavy metal fillers physically mixed into the polymer matrix thus imparting radiopacity to the whole system due to the high Z-element nature of the filler. [85] Most commonly used fillers for this technique include iodine, barium, bismuth, zircon, and tantalum. [48, 86-90] While successful radiopacity was achieved, the composites generally suffered from reduced mechanical properties due to heterogeneous dispersion of the radiopaque filler from phase separation of metal fillers from resins. [48] This resulted in aggregate formation that ultimately caused crack formation and propagation in the polymer matrix leading to leakage of the radiopaque filler. [85]

Chithambara *et al*. synthesized radiopaque microspheres by dispersing tantalum within a polymer matrix synthesized using toluene diisocyanate and poly(tetramethylene glycol). [87] Their findings proved the microspheres to be radiopaque with potential as radiopaque embolization agents. [87] However, higher filler loadings resulted in greater aggregates within the polymer, inducing particle size variability. [87]

Barium has also been used to impart radiopaque properties for a variety of medical devices, including denture materials. [91-93] In one study, barium fluoride (BaF_2), at 30 wt %, was used to develop denture material due to its satisfactory radiopacity and minimal discoloration of the material overall. [91] However, BaF_2 leaching occurred within

seven days causing the filler to infiltrate the surrounding tissue. This induced toxicity and altered the mechanical properties of the material. [91]

Radiopaque polymer salt complexes were developed to improve homogeneity and reduce gradual filler leaching. [85, 94] A heavy metal salt was complexed to an appropriate polymer ligand *via* chelation resulting in a homogenous system with polymeric and ionic character. [48] The polymers used for this technique were ionic, meaning they had a charged polar section to bind to cations and a non-polar section which would allow solubilization in non-polar media. [85] Polymer salt complexes were advantageous because they result in limited heavy metal release and constant radiopacity due to entrapment of the salt in a complex network. [94] However, the binding of the salt to the polymer ligand was a result of non-covalent interactions which could easily be disrupted in acidic aqueous conditions, similar to some physiological conditions. [85] Additionally, the halogenated functional groups in these systems may degrade *via* hydrolysis and result in potentially toxic leachables. [85]

Radiopaque polymerized monomers were also used to impart radiopacity to polymers by synthesizing radiopaque monomers that could covalently be incorporated into the polymer backbone. [86, 95, 96] This technique resulted in homogenous, non-leachable materials that retained similar mechanical properties to that of the non-radiopaque parent polymer. [48, 85] However, a major disadvantage of utilizing these systems is the high production cost, which may not be practical for all medical applications. [85]

In this work, the authors developed radiopaque composite materials using shape memory polymers (SMPs) for their use as biomedical implants. Thermally actuated shape memory polymers are a special class of materials that are capable of switching between a primary and a secondary shape upon a heat stimulus. [4, 5, 43, 47, 97] These versatile materials are used for a wide range of applications such as biomaterials, textiles, and automotive. [1, 6] Hasan *et al*. developed aliphatic polyurethane/urea SMP foams for embolic occlusion applications due to their ability to retain a programmed shape and passively actuate inside the body over a given time. [98] Previously synthesized SMP foams have proven to rapidly occlude aortic aneurysms and the resulting clot is stable up to 90 days. [38, 46] These SMP foams can further be utilized for a neurovascular occlusion device due to their ultra-low density, which allows for the material to be crimped to a small geometry and delivered to the aneurysm *via* catheter. [46]

X-ray visualization of the device, however, is a challenge, because the polyurethane SMP material has a density similar to soft tissue and cannot be observed during x-ray fluoroscopy. [38] Therefore delivery of the foam to the aneurysm in a safe and reliable manner is a significant challenge, as guidance by x-ray contrast cannot be used. The purpose of this work was to introduce radiopacity to the foam using heavy metal nanoparticles, which can be incorporated into the polymer using physical mixing. Tungsten has been used as a radiopaque agent previously for embolic coils with much success. [38, 99-102] Kampmann *et al.* studied tungsten biocompatibility in human subjects showing minimal inflammatory response invoked by the radiopaque coils. [99] Additionally, Peuster *et al*. evaluated in vitro cytotoxic effects of tungsten on various

human cells. Their studies concluded that while tungsten may be elevated in the blood serum, there were no cytotoxic effects on the local tissue. [100]

Based on the established biocompatibility of tungsten, Rodriguez *et al*. synthesized SMP foams for embolic applications with tungsten microparticles to induce x-ray visualization and achieved sufficient opacity with foam geometries up to 6 mm diameter cylinders. [38] While the SMP microcomposites were visible under x-ray fluoroscopy, radiopacity was highly dependent on the diameter of the foam cylinders. Larger diameter cylinders would limit the accessibility of the embolic devices to peripheral blood vessels only therefore small geometry radiopaque materials need to be developed for neurovascular applications. Additionally, high filler loading disrupted foam synthesis. Previously, 4% by volume was the maximum tungsten loading that could be achieved with microparticles which would also require the use of large geometry foam cylinders for visualization. This study aims to increase filler loading by using nanoparticles, allowing for improved particle dispersion resulting in visualization of smaller geometry materials for neurovascular devices that require radiopacity through soft and hard tissue. The materials developed by Hasan *et al*. had optimal actuation profiles of 5 to 10 minutes for device delivery and served as the core chemistry for this research.

3.2 Materials and methods

N,N,N’,N’-Tetrakis(2-hydroxypropyl)ethylenediamine (HPED, 99%; Sigma-Aldrich Inc., St. Louis, MO), triethanolamine (TEA, 98%; Sigma-Aldrich Inc., St. Louis, MO), trimethyl-1,6-hexamethylene diisocyanate, 2,2,4- and 2,4,4- mixture (TMHDI,

TCI America Inc., Portland, OR), DC 198 (Air Products and Chemicals, Inc., Allentown, PA), DC 5943 (Air Products and Chemicals, Inc., Allentown, PA), T-131 (Air Products and Chemicals, Inc. Allentown, PA), BL-22 (Air Products and Chemicals, Inc, Allentown, PA), Enovate 245fa Blowing Agent (Honeywell International, Inc., Houston, TX), 0.1 N hydrochloric acid (HCl) (Sigma-Aldrich Inc., St. Louis, MO), 2-propanol 99% (IPA) (VWR, Radnor, PA) and deionized (DI) water (> 17 MΩ cm purity; Millipore water purifier system; Millipore Inc., Billerica, MA) were used as received. Tungsten nanoparticles (W, 99.95%, 40-60 nm) (US Research Nanomaterials Inc., Houston, TX) were dried for 12 hours, under vacuum, prior to foam synthesis.

SMP foam synthesis was conducted using the protocol described by Hasan *et al*. Isocyanate (NCO) pre-polymer was first synthesized and cured for 32 hours at 50°C. TMDHI comprised the NCO pre-polymer along with 35% of alcohols (HPED and TEA). [98] W nanoparticles (40-60 nm) were dispersed in the NCO pre-polymer, prior to foam blowing, at 4% to 11% by volume. Molar equivalent of the remaining hydroxyls was added to the hydroxyl (OH) pre-polymer. The resulting OH pre-polymer was combined with the NCO-W mixture, along with catalysts, surfactants, and Enovate. [98] The foam was cured at 90°C under vacuum at -10 mmHg for 10 minutes. [98] The SMP foam was allowed to cool to room temperature before further characterization. [98] Post-cure purification of the SMP included acid etching the nanocomposites using 0.1N HCl for 2 hours followed by two 15 minute sonication cycles in IPA. The SMP foams were then rinsed using reverse osmosis (RO) water using four 15 minute sonication cycles. The purified foams were dried overnight at 55°C under vacuum. **Table 3.1** shows the

weight percent of each component used in foam blowing. 3 foams batches were synthesized and characterized for duplicity. Foams with 11% W loading were not reproducible and therefore their thermo-mechanical properties were not characterized.

3.2.1 Density and porosity

Density measurements were conducted on foam blocks acquired from the top, middle, and bottom section of the foam. Mass of the foam block was recorded and length, width, and height values were measured three times using a digital caliper. Porosity was calculated using Equation 3.1. Density of the non-porous neat polymer was calculated without accounting for foaming agents such as catalysts, surfactants, DI water, and Enovate.

$$Porosity\ (\%) = \left(\frac{\rho_{neat} - \rho_{foam}}{\rho_{neat}}\right) * 100 \qquad \text{(Eq. 3.1)}$$

3.2.2 SEM and pore sizes

Cell structure was determined by cutting thin slices of the bulk foam in the axial and transverse direction. The samples were mounted onto a stage and sputter coated for 60 seconds at 20 mA with gold using Cressington Sputter Coater (Ted Pella, Inc., Redding, CA). The samples were then imaged using Joel NeoScope JCM-5000 Scanning Electron Microscope (Nikon Instruments, Inc., Melville, NY) at 10-13x magnification under high vacuum and 5-10 kV current. Pore sizes were calculated by measuring the cell diameter, using Image J software (NIH, Bethesda, MD), in the axial and transverse direction for each SEM image.

Table 3.1: Composition of foams using 100% trimethylhexamethylene diisocyanate (TMHDI) for the isocyanate component of the urethane foam and increasing volume percent concentration of W nanoparticles. Three foam batches were synthesized and the average weight percent of the monomers and volume percent of tungsten nanoparticles was determined for all batches.

Composition	W (vol %)	TMHDI (wt %)	HPED (wt %)	TEA (wt %)	Water (wt %)	T-131 (wt %)	BL-22 (wt %)	DC 198 (wt %)	DC 5943 (wt %)	Enovate (PPH)
100 TMDHI 0% W	0.00 ± 0	66.70 ± 0.1	17.11 ± 0.02	5.74 ± 0.01	2.35 ± 0	0.26 ± 0	0.65 ± 0	2.62 ± 0.1	4.59 ± 0.01	14.88 ± 0
100 TMDHI 4% W	4.00 ± 0.001	66.72 ± 0.03	17.10 ± 0.04	5.75 ± 0.03	2.35 ± 0.01	0.26 ± 0.01	0.65 ± 0.01	1.71 ± 1	5.45 ± 1	14.57 ± 2
100 TMHDI 5% W	4.99 ± 0.002	66.69 ± 0.1	17.13 ± 0.02	5.74 ± 0	2.36 ± 0	0.26 ± 0	0.65 ± 0	2.56 ± 0.03	4.61 ± 0.1	14.55 ± 2
100 TMHDI 6% W	5.99 ± 0.01	66.72 ± 0.04	17.12 ± 0.02	5.74 ± 0	2.35 ± 0	0.26 ± 0.01	0.66 ± 0.01	2.55 ± 0.02	4.60 ± 0.04	14.55 ± 2
100 TMHDI 7% W	6.99 ± 0.01	66.75 ± 0.04	17.12 ± 0.02	5.74 ± 0	2.34 ± 0.01	0.26 ± 0.01	0.65 ± 0.01	2.54 ± 0.02	4.60 ± 0.03	17.00 ± 0.1
100 TMHDI 8% W	7.98 ± 0.01	66.71 ± 0.1	17.13 ± 0.03	5.74 ± 0.03	2.35 ± 0.01	0.26 ± 0.01	0.65 ± 0.01	2.54 ± 0	4.61 ± 0.01	16.98 ± 0.04
100 TMHDI 9% W	8.98 ± 0.01	66.76 ± 0.1	17.12 ± 0	5.74 ± 0.03	2.35 ± 0.01	0.26 ± 0	0.64 ± 0	2.56 ± 0.02	4.58 ± 0.02	17.00 ± 0.04
100 TMHDI 10% W	9.98 ± 0.01	66.73 ± 0.03	17.13 ± 0	5.74 ± 0.02	2.35 ± 0.01	0.26 ± 0	0.64 ± 0	2.55 ± 0.01	4.61 ± 0.02	16.99 ± 0.02
100 TMHDI 11% W	10.97	66.72	17.11	5.74	2.36	0.25	0.65	2.60	4.58	17.00

3.2.3 Transmission electron microscopy (TEM)

A small piece (2mm x 4mm) of the sample was cut and embedded in the flat mold with Polybed 812 (Polysciences, Inc., Warrington, PA) and polymerized at 60°C, overnight. The sample resin block was sectioned at room temperature, using Leica UC6 microtome (Leica Microsystems, Wetzlar, Germany) and DiATOME diamond knives (DiATOME, Hatfield, PA). Ultra-thin sections (70 nm) were examined by JEOL 1200EX II electron microscopy (Jeol, Peabody, MA).

3.2.4 X-ray imaging

An opacity frame was developed by mounting filler-loaded foam samples onto a clear polycarbonate sheet. 2 mm foam cylinders were threaded over an 89 μm diameter nickel-titanium (Nitinol) wire (NDC, Fremont, CA). A Guglielmi Detachable Coil (GDC) (Boston Scientific, Marlborough, MA) used as the control for this experiment because it is a platinum coil which is considered the current gold standard for aneurysm treatment. The opacity frame was placed under a porcine head and imaged using a Philips Allura Xper FD 20 C-arm System (Koninklijke Philips N.V., Amsterdam, Netherlands) at 63 kV and 382 mA through soft and hard tissue. Images of the opacity frame were collected under porcine jaw and neck for evaluating foam visibility at multiple sites compared to the control.

3.2.5 X-ray density (X.D.)

X-ray images of the opacity frame were acquired on a Bruker In-Vivo Xtreme multimodal preclinical imaging system (Bruker BioSpin Corp., Billerica, MA) outfitted with a 4 MP back-thinned, back-illuminated 4MP CCD detector. X-rays were collected

with an exposure time of 1.0 s, where the f-stop = 1.40, FOV = 153.0 mm, vertical and horizontal resolution = 377 ppi and X-ray energy = 45 KVP. Images were edited using Bruker molecular imaging software. The background was subtracted using an illumination correction reference. To quantify the x-ray density for each sample, a length of 0.50 cm was selected along each sample in the X-ray image as the region of interest. Greater than 70 pixels of X-ray density (X.D.) were taken within the region of interest for each foam utilizing Bruker Molecular Imaging Software (Bruker BioSpin Corp., Billerica, MA). From these measurements, a mean and standard deviation of the X.D. was calculated.

3.2.6 DSC

The glass transition temperature (T_g) of the foams (n=5) was determined under dry and wet conditions. For dry T_g, foam samples (3-8 mg) were used which were stored in a dry container with desiccant, prior to analysis. A Q-200 DSC (TA Instruments, Inc., New Castle, DE) was used to attain the thermogram for our foams. The first cycle consisted of decreasing the temperature to -40°C at $10°C \cdot min^{-1}$ and holding it isothermal for 2 minutes. The temperature was then increased to 120°C at $10°C \cdot min^{-1}$ and held isothermal for 2 minutes. In the second cycle, the temperature was reduced to -40°C at $10°C \cdot min^{-1}$, held isothermal for 2 minutes, and raised to 120°C at $10°C \cdot min^{-1}$. T_g was recorded from the second cycle based on the inflection point of the thermal transition curve using TA instruments software (TA Instruments, Inc., New Castle, DE). The aluminum tin was not vented during this step. For wet T_g, foam samples (3-8 mg) were submerged in RO water at 50°C for 5 minutes to allow full plasticization. After the

samples were removed from water, they were pressed dry with Kim Wipes (Kimberly-Clark Professionals, Roswell, GA), weighed, and placed in an aluminum pan sealed with an aluminum lid that was vented. Q-200 DSC was used to cool the samples to -40°C, hold them isothermal for 2 minutes, and heat them to 80°C at 10°C·min^{-1}. TA instruments software (TA Instruments, Inc., New Castle, DE) was used to generate the thermogram and acquire the T_g, after water plasticization, using the average inflection point of the thermal transition.

3.2.7 Tensile testing

Uniaxial tensile loading tests were carried out using an Insight 30 Material Tester (MTS Systems Corporation, Eden Prairie, MN) at a constant strain rate of 5 mm/min at room temperature. 10 foam samples with (L= 25mm, W= 15mm, H= 3mm) were cut from the bulk material. Wood tabs were secured on each end of the foam, using epoxy, to prevent sample deformation in the grips during testing. Tensile strength (kPa), Young's modulus (kPa), toughness (J·m^{-3}) and strain at break (%) were determined per sample using the stress-strain curve.

3.2.8 Actuation studies

Cylindrical foam samples (n=3) with a diameter of 2 mm and a height of 1 cm were cut. A 203.20 μm diameter nickel-titanium (Nitinol) wire (NDC, Fremont, CA) was inserted through the center of the sample along its length to serve as a stabilizer. The foam samples were radially compressed to their smallest possible diameter using ST 150-42 stent crimper (Machine Solutions, Flagstaff, AZ) by heating the material to 100°C, holding it isothermal for 15 minutes, and programming the foams to the crimped

morphology. Initial foam diameter was measured and recorded for each sample using Image J software. The foams were placed in a water bath at 37°C and images were taken at 30 seconds, 1 minute and every minute thereafter till 15 minutes, followed by one image every 5 minutes thereafter till 30 minutes. Foam diameter was measured, at each time point, using Image J software. The foams were then placed in a 70°C RO water bath, removed after 20 minutes, and allowed to cool to room temperature. The final diameter of the samples was measured and recorded using Image J software. Percent volume recovery was calculated using Equation 3.2 and volume expansion was calculated using Equation 3.3.

$$\%\, Volume\ Recovery = \left(\frac{Recovered\ diameter}{Original\ diameter}\right)^2 * 100 \qquad \text{(Eq. 3.2)}$$

$$Volume\ Expansion = \left(\frac{Recovered\ diameter}{Compressed\ diameter}\right)^2 \qquad \text{(Eq. 3.2)}$$

3.3 Results and discussion

3.3.1 Density and porosity

Foam density increased markedly, from 0.013 to 0.060 g·cm^{-3}, with greater W incorporation due to the added mass within the foam struts per block, **Table 3.2**. All compositions, however, maintained low densities, indicative of the foams retaining high surface area to volume ratios. SMP nanocomposites containing 10%W had significantly lower density than 9%W foams due to changes in pore sizes which are discussed in the next section. Neat polymer density also increased with W addition (Table 3.2), from 1.0 to 3.0 g·cm^{-3}, indicating the material became heavier with filler content without variation from foaming agents. Porosity calculations (Table 3.2) showed high porosity (> 98%)

for all compositions with low standard deviation, indicating cell uniformity throughout the bulk foam. These results confirm the development of lightweight foams with high surface area suitable for embolic occlusion devices.

3.3.2 SEM and pore sizes

SEM images of the foams, **Figure 3.1a**, indicate smaller pore sizes with greater tungsten incorporation. Nanoparticles serve as nucleating sites during the gas blowing foaming process, which increases the number of bubbles generated in the polymer matrix. This, in turn, causes smaller bubble generation and ultimately smaller pore sizes throughout the bulk foam. Note that, while pore density and volume change with loading, overall porosity remains relatively constant. Additionally, pore diameter measurements, **Figure 3.2**, show the pores are becoming more isotropic compared to the control foam where the pores are larger in the axial foaming direction than the transverse direction. 10%W nanocomposites had more isotropic pores compared to the other nanocomposites and the increase in pore size in the transverse direction had an inverse effect on foam density. Nanofiller addition increased the polymer viscosity prior to foam blowing which translates to smaller pore sizes of the bulk foam due to slower gas release within the increasingly viscous polymer solution. Tungsten nanoparticles can therefore be used to control foam morphology and serve as a tool to regulate pore sizes.

Table 3.2: Key physical and thermal properties of the SMP foam nanocomposites.

W (vol %)	ρ_{foam} ($g \cdot cm^{-3}$)	ρ_{neat} ($g \cdot cm^{-3}$)	Porosity (%)	Dry T_g (°C)	Wet T_g (°C)	Volume Recovery (%)	Volume Expansion (x)
0% W	0.013 ± 0.001	1.0 ± 0.02	99 ± 0.1	58 ± 2	34 ± 1	108 ± 24	63 ± 14
4% W	0.033 ± 0.004	1.8 ± 0.03	98 ± 0.2	63 ± 1	28 ± 1	82 ± 15	21 ± 4
5% W	0.041 ± 0.000	2.0 ± 0.04	98 ± 0.0	65 ± 1	35 ± 0	89 ± 19	29 ± 11
6% W	0.045 ± 0.002	2.2 ± 0.04	98 ± 0.1	67 ± 0	38 ± 1	93 ± 17	41 ± 8
7% W	0.045 ± 0.004	2.4 ± 0.05	98 ± 0.2	66 ± 1	39 ± 1	94 ± 19	36 ± 11
8% W	0.054 ± 0.009	2.6 ± 0.05	98 ± 0.4	67 ± 1	41 ± 0	99 ± 13	35 ± 7
9% W	0.060 ± 0.011	2.8 ± 0.06	98 ± 0.4	66 ± 1	41 ± 1	105 ± 17	32 ± 10
10% W	0.048 ± 0.003	3.0 ± 0.06	98 ± 0.1	68 ± 1	41 ± 1	98 ± 16	36 ± 10

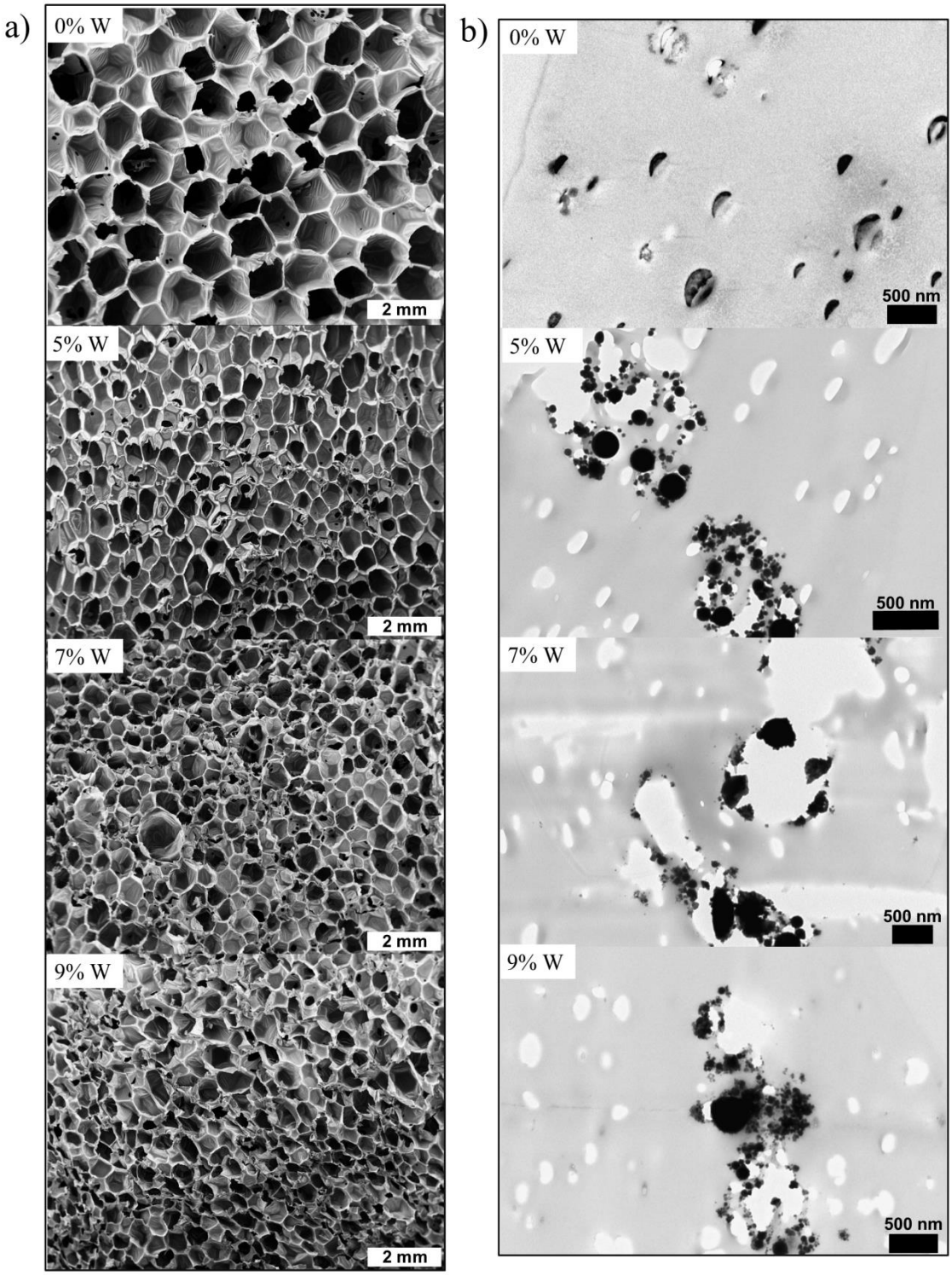

Figure 3.1: a) SEM images of the SMP nanocomposites at 10-11x magnification. b) TEM images of the SMP nanocomposties showing filler aggregates.

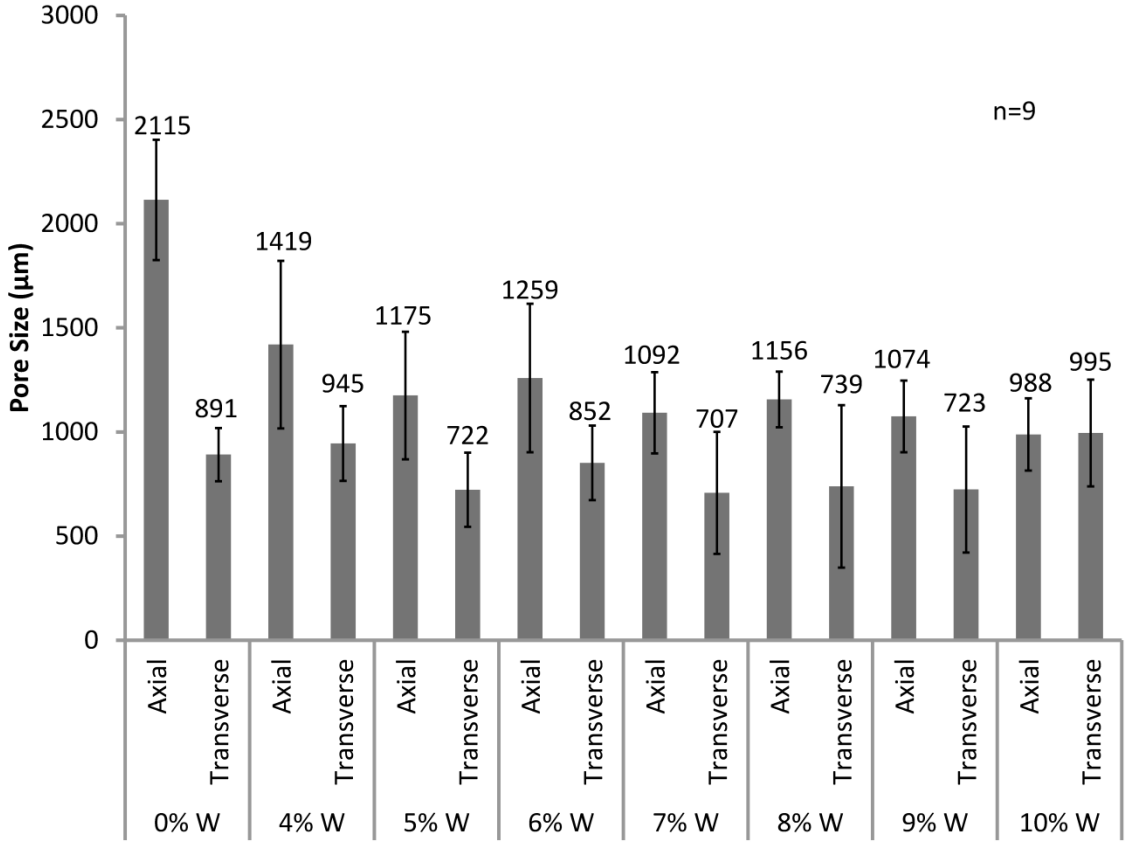

Figure 3.2: Pore sizes in the axial and transverse direction of SMP foams with increasing W content.

3.3.3 TEM

Incorporation of W nanoparticles into the SMP system resulted in aggregate formation at the nanoscale even at low concentrations, **Figure 3.1 b**. TEM image of the control (0%W) foam shows nanopores within the polymer struts which indicate the occurrence of these defects as a part of the foaming process rather than as a result of filler incorporation. However, 5%W, 7%W, and 9%W composites have filler aggregates

in the polymer struts that imply poor dispersion of the nanoparticles with physical mixing.

3.3.4 X-ray imaging

Sufficient x-ray visibility was achieved for SMP nanocomposites with W loading greater than 6%, **Figure 3.3**. Crimped foams attenuated x-rays through soft and hard tissue of the porcine head at various locations, suggesting acceptable visibility through qualitative analysis.

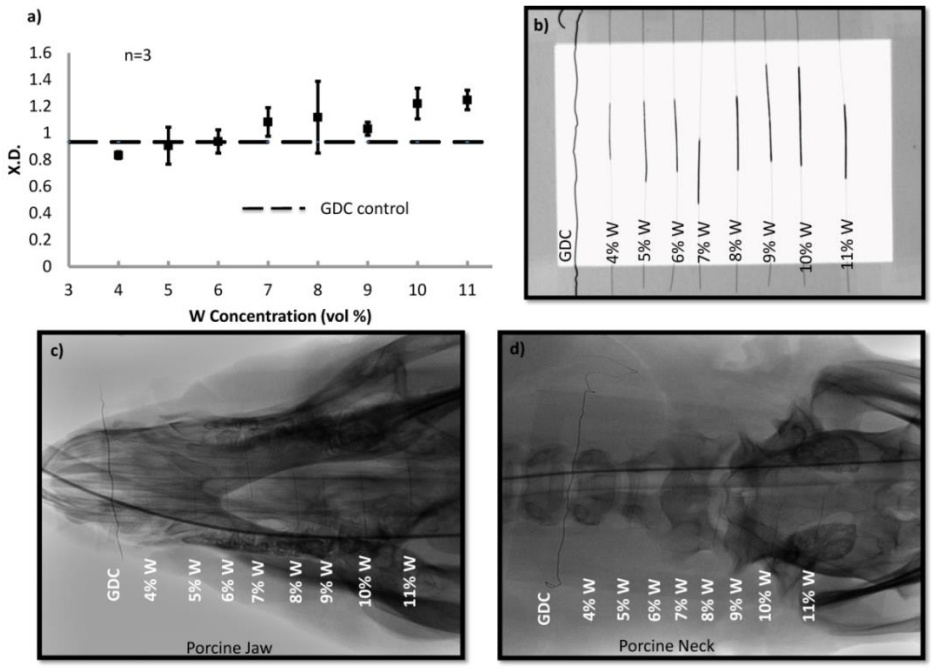

Figure 3.3: a) X-ray density of the SMP foams with increasing W content. b) Design of the frame mounted with crimped SMP foam over nitinol wire. c) X-ray image of the SMP foams through porcine jaw. d) X-ray image of the SMP foams through porcine neck. Panels a) and b) were acquired *via* collaboration with the Laboratory for Synthetic-Biologic Interactions using a Bruker In-Vivo Xtreme multimodal preclinical imaging system. Panels c) and d) were acquired *via* collaboration with Texas Institute of Preclinical Studies using a Philips Allura Xper FD 20 C-arm System

3.3.5 X-ray density (X.D.)

Quantitative evaluation of foam visibility was conducted *via* X.D. analysis (Figure 3.3). With increasing W loading, the crimped SMP attenuates x-ray more effectively, increasing from 0.8 to 1.2 at 45 KV. For SMP foams with greater than 6% W, average X.D. was larger than the GDC control (0.9). Filler addition successfully imparted radiopacity to the polymer system such that it will allow for use of smaller foam diameters without compromising x-ray visibility.

3.3.6 DSC

Thermal characterization of the foams revealed increasing transition temperatures with greater W loading (Table 3.2). Dry T_g of the SMP foams increased by 10°C while wet T_g increased by 7°C with higher filler content. Nanoparticle incorporation restricted polymer mobility at the molecular level and increased the number of physical crosslinks within the SMP network. The addition of these physical crosslinks requires greater heat input for the polymer to transition from the glassy to the rubbery state therefore shifting the T_g towards higher temperatures. This finding serves as a method for tuning thermal properties of the system for other applications that require a specific actuation temperature.

3.3.7 Tensile testing

Increasing W concentration in SMP foams changed mechanical properties compared to the control (**Table 3.3**, **Figure 3.4**). An increase in Young's modulus can be observed, from 2600 ± 200 kPa to 10100 ± 400 kPa, for 4%W foams, indicating greater material stiffness. However, higher filler content resulted in decreasing stiffness

due to disruption of the polymer matrix. Similarly, the tensile strength of the foams increased at 4%W, from 96 ± 2 kPa to 120 ± 20 kPa, however beyond this concentration the mechanical properties decrease as a result filler agglomerates replacing the polymer within the foam struts. Filler agglomerates within the foam struts resulted from poor dispersion due to relatively agglomerated starting materials, *e.g.* tungsten nanopowder. At high filler concentrations, W agglomerates caused particle bridging which resulted in weak planes in the nanocomposite. Toughness and strain at break of the SMP material also decreased compared to the control foam because of increased stiffness and aggregate formation due to high filler loading (Figure 3.4). Overall, with higher W nanoparticle loading the foams became harder due to increased stiffness and decreasing polymer content within the struts. Additionally, variation in tensile strength and Young's modulus of the higher loaded foams occurred due to changes in foam morphology as a result of heterogeneous pore sizes.

Table 3.3: Key mechanical properties of the SMP foam nanocomposites.

W (vol %)	Modulus (kPa)	Ultimate Tensile Strength (kPa)	Toughness ($J \cdot m^{-3}$)	Strain at Break (%)
0% W	2598 ± 197	96 ± 23	97 ± 29	20 ± 1
4% W	10103 ± 439	117 ± 16	46 ± 7	9 ± 1
5% W	6293 ± 415	107 ± 18	60 ± 12	12 ± 0
6% W	5698 ± 1107	90 ± 5	48 ± 10	10 ± 4
7% W	3098 ± 258	78 ± 3	40 ± 6	11 ± 1
8% W	5472 ± 1909	82 ± 27	26 ± 9	7 ± 0
9% W	2495 ± 1037	60 ± 6	27 ± 9	11 ± 2
10% W	4075 ± 1567	67 ± 12	20 ± 13	9 ± 2

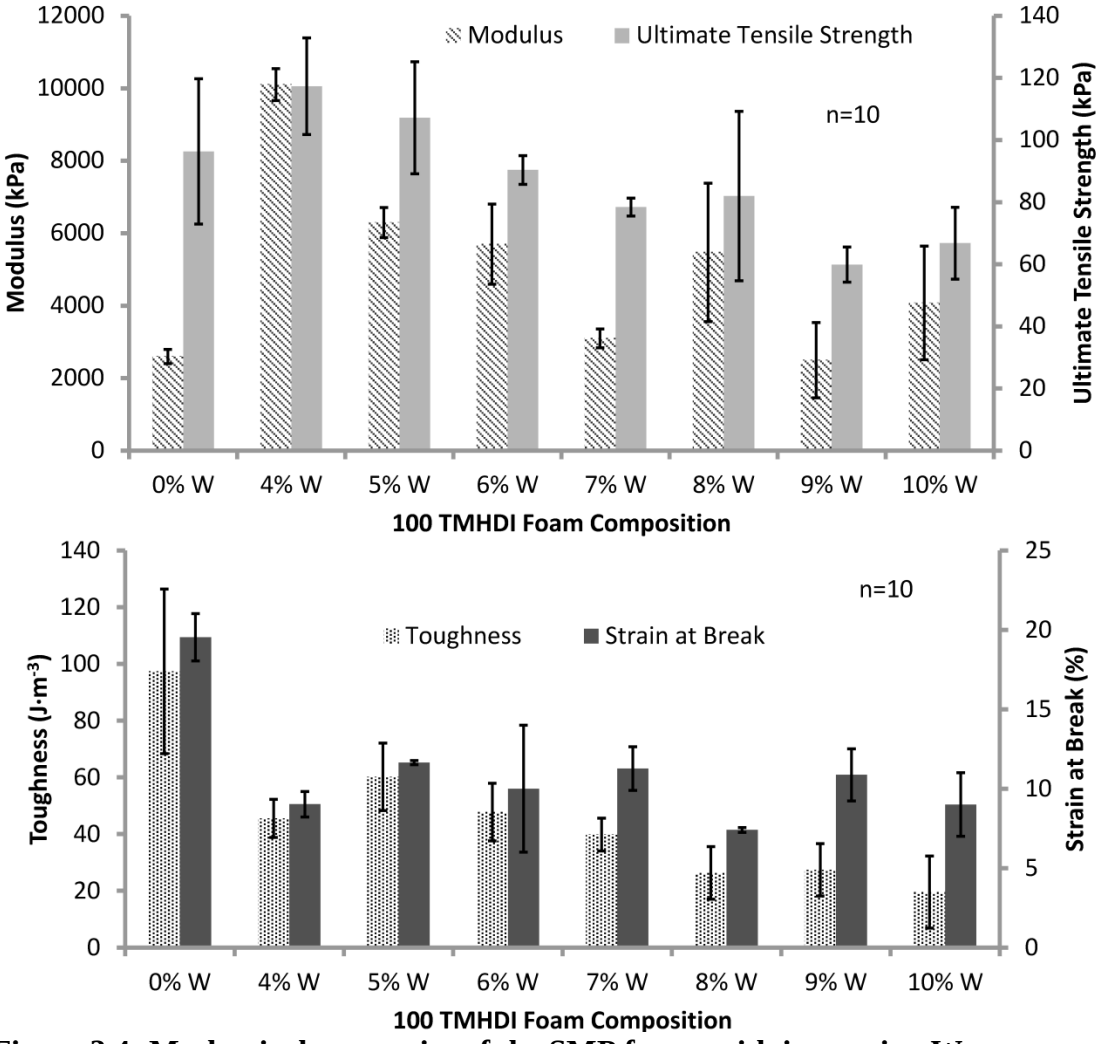

Figure 3.4: Mechanical properties of the SMP foams with increasing W content.

3.3.8 Actuation studies

Nanoparticle addition altered passive actuation kinetics of SMP foams at physiological temperature (**Figure 3.5)**. The control foam actuated within 4 minutes, as indicated by the inflection point of the plot. However, with increasing W loading the SMP experienced longer actuation times of 6, 8, and 10 minutes for 5% W, 7%W, and 9% W foams, respectively, which is reasonable given their increasing thermal

transitions. Volume recovery (Table 3.2) of the foams remained greater than 80% for all foams, however, considerably less than the control foam due to increased molecular restrictions on the network mobility. Similarly, volume expansion of the foams decreased with W addition, from 63x ± 14 to 21x ± 4, for the control foams and 4% W loaded foams, respectively.

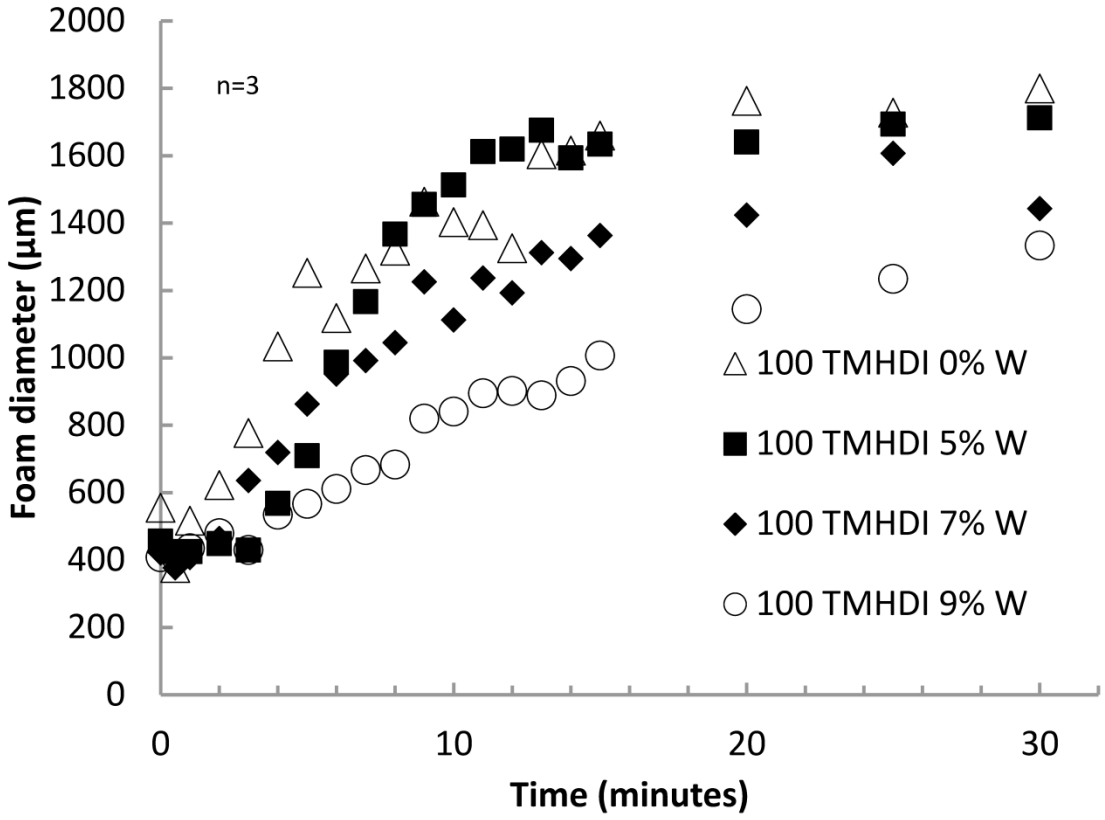

Figure 3.5: Actuation time of the SMP foams with increasing W content.

SMP foam nanocomposites were synthesized with inherent radiopacity by incorporating W nanoparticles within the polymer matrix during OH premix synthesis. W is a high Z number element which allowed it to effectively attenuate x-rays and impart visibility to SMP foams through soft and hard tissue. A smaller foam geometry was used for neurovascular applications, therefore higher filler loading was required to make the foams radiopaque. W concentrations greater than 6% resulted in sufficient foam visibility, when crimped, and had greater X.D. compared to the GDC control. Additionally, the SMP foams maintained their low density and high porosity, making them desirable for aneurysm occlusion devices due to their large volume expansion and high surface area. W nanoparticles served as a tool for controlling viscosity of the foam mixture and provided nucleation sites, which resulted in smaller and more isotropic pores with greater filler loading. This finding is critical for controlling the overall foam morphology and serves as a platform for material development for new medical applications that require specific pore sizes in polyurethane scaffolds. Filler dispersion improved significantly with nanoparticle content compared to the microcomposites developed by Rodriguez *et al*. W nanoparticles dispersion within the foam matrix was more homogeneous, compared to W microparticles, as seen by the lack of filler agglomerates within the struts and the foam membranes in the SEM images (Figure 3.1a). However, filler aggregation still occurred on the nanoscale (Figure 3.1b), indicating the need for further optimization of nanoparticle mixing into the foam matrix.

Thermal characterization of the foams showed increasing transition temperature, under dry and wet conditions, for foams with W loading greater than 5%. The

nanoparticles restricted network mobility, thereby increasing polymer stiffness, and required higher temperature for the polymer to transition from the glassy to rubbery state. W addition provided greater control over the thermal properties of the SMP system. This functions as a potential tool for further tuning of the foams and prevention of premature water plasticization of foams in the catheter during device delivery. Similarly, passive actuation time of the foams increased with filler addition due to slower foam plasticization by water. Fortuitously, W nanoparticles have potential use providing greater control over the actuation kinetics of SMP foams, similar to altering the chemical backbone as studied by Hasan *et al.*, to achieve longer working times for clinical applications. Volume recovery and expansion of the SMP foams decrease with greater W loading. However, the foams recover to 80% of their original diameter and expand up to 40x their original volume, maintaining their efficacy for aneurysm occlusion.

Lastly, mechanical properties of the SMP nanocomposites diminished with filler addition due to a large percentage of the polymer strut being replaced by W. While nanoparticles increased material stiffness and strength up to 4% W loading, an opposite effect was observed on toughness and strain-to-failure at all concentrations. W is traditionally used in low concentrations to develop mechanically robust composites, therefore lower toughness was expected for high filler concentration. Furthermore, the foams were tested below T_g. This could have a negative effect on mechanical properties as, above T_g, the rubbery polymer would align around the filler particles and provide higher toughness and strain-to-failure response. Additionally, increasing the crosslink

density of the material due to filler loading would further lower material toughness and strain at break.

3.4 Conclusions

In conclusion, radiopaque SMP foam nanocomposites were developed with high W loading, up to 10% by volume, and high porosity for aneurysm occlusion applications. W nanoparticles successfully introduced radiopacity of the foams, using x-ray fluoroscopy, and made the device visible during transcatheter delivery and deployment within the aneurysm. Additionally, thermal properties of the composites were controlled by filler content with greater W concentrations resulting in higher T_g. Actuation profiles of the SMP composites were tailored with filler content due to increased stiffness which delayed actuation and mechanical properties were modified compared to unloaded foams. The new SMP nanocomposites provide a greater control over device visibility and actuation kinetics compared to the previously developed SMP systems by Rodriguez *et al*. and Hasan *et al*. Nanoparticles afforded uniform filler dispersion and minimal foam destabilization compared to microparticles. Nanoparticles also served as a nucleating agent during foam synthesis and resulted in smaller cell sizes with increasing filler loading. Overall, the SMP foams have comparable radiopacity to current GDC coils and variable thermo-mechanical properties that make them optimal for use as embolic agents for neurovascular applications.

CHAPTER IV

USE OF NANOPARTICLES TO MODIFY MECHANICAL PROPERTIES AND SHAPE MEMORY BEHAVIOR*

4.1 Introduction

Shape-memory polymers (SMPs) are materials that have the ability to switch between a primary and a secondary shape upon the input of an external stimulus, such as heat, electrical impulse, or change in pH. [2, 12, 103] The SMPs utilized in the current study can be synthesized in a primary shape, heated above their glass transition temperature (T_g), and programmed into a secondary shape. Upon cooling, the material will maintain this secondary geometry until the system is exposed to a thermal stimulus, allowing the SMP to recover to its original shape. This thermo-responsive nature can be harnessed to develop devices for embolization of cerebral aneurysms. [19, 33, 47, 98] We previously fabricated SMP foams that demonstrate rapid, stable aneurysm occlusion, comparable to the Guglielmi Detachable Coils, which are the current gold standard. [104] Additionally, SMP foam-over-wire devices can be implanted in an aneurysm *via* minimally invasive surgery through the femoral artery. Passive actuation of the foam under physiological conditions results in stable clot formation, which is replaced by inert scar tissue over 3-6 weeks. [38] The healed aneurysm has potential for minimizing the chance of recanalization

---

*Reprinted with permission from "Modification of Shape Memory Polymer Foams Using Tungsten, Aluminum Oxide, and Silicon Dioxide Nanoparticles," by Sayyeda M. Hasan, Robert S. Thompson, Adam L. Nathan, Andrew C. Weems, Fang Zhao, Mary Beth Browning Monroe, Duncan J. Maitland, RSC Advances 2016, 6, 918-927. Reproduced by permission of The Royal Society of Chemistry (2016).

and clot migration into the parent vessel due to the restored endothelial tissue at the aneurysm neck. [38]

While our SMP foams have significant advantages over current treatments, a potential drawback could occur from the ultra-low density of the porous polymer system, resulting in foam shearing and particulate generation during device fabrication and implantation. Particle generation after implantation is especially hazardous and can cause unintended ischemia and small vessel occlusion, both of which are negative side effects of this treatment. Additionally, the SMP foam may fracture during device delivery through tortuous vasculature, which may result in device failure. Developing tougher, wear-resistant polymer systems could mitigate foam fracture and particulate generation while preserving device function during processing and handling.

Nanofillers have been used to improve mechanical properties of various polymer composites. [105-108] Most composites only require small filler concentrations to achieve drastic improvements in mechanical toughness and strength. [109] The nanoparticles act as physical crosslinks within the polymer network, which limit chain mobility, but improve shock absorption and tear resistance. [110] Silica (SiO_2) nanoparticles have been used to improve the mechanical and thermo-mechanical properties of epoxy resins as well as to control their viscosity. [111] Alumina (Al_2O_3) has also been utilized in various polymer composites and ceramics to increase hardness and toughness. [112] This inert nanofiller is known to improve load-bearing capabilities of implantable biomaterials while maintaining excellent biocompatibility. [113] Tungsten nanoparticles have previously been used by our group to impart radiopacity to SMP foams. High filler loading decreases

mechanical toughness due to disruption of the polymer matrix, [114] but other groups have reported that low concentrations of tungsten improve the mechanical properties of composites. [115] Tungsten coils have been extensively tested for biocompatibility in human and animal subjects, with minimal toxic indications. [99-101]

The goal of this research was to develop SMP foams with reinforcing nanofillers to improve mechanical properties. Aluminum oxide (Al_2O_3), silicon dioxide (SiO_2) and tungsten (W) nanoparticles were used due to their pre-established use in medical implants and their contribution to developing tough, wear-resistant materials.

4.2 Materials and methods

4.2.1 Materials

N,N,N',N'-Tetrakis(2-hydroxypropyl)ethylenediamine (HPED, 99%; Sigma-Aldrich Inc., St. Louis, MO), triethanolamine (TEA, 98%; Sigma-Aldrich Inc., St. Louis, MO), trimethyl-1,6-hexamethylene diisocyanate, 2,2,4- and 2,4,4- mixture (TMHDI; TCI America Inc., Portland, OR), DC 198 (Air Products and Chemicals, Inc., Allentown, PA), DC 5943 (Air Products and Chemicals, Inc., Allentown, PA), T-131 (Air Products and Chemicals, Inc. Allentown, PA), BL-22 (Air Products and Chemicals, Inc, Allentown, PA), Enovate 245fa Blowing Agent (Honeywell International, Inc., Houston, TX), 2-propanol 99% (IPA; VWR, Radnor, PA) and deionized (DI) water (> 17 MΩ cm purity; Millipore water purifier system, Millipore Inc., Billerica, MA) were used as received. Tungsten standard for AAS (1000 mg/L; Sigma Aldrich Inc., St. Louis, MO), aluminium standard for ICP (1000 mg/L; Sigma Aldrich Inc., St. Louis, MO), and

silicon standard for ICP (1000 mg/L; Sigma Aldrich Inc., St. Louis, MO) were mixed into nitric acid (70% purity, 99.999% trace metal basis; Sigma Aldrich Inc., St. Louis, MO) before characterization. Tungsten nanoparticles (W, 99.95%, 40-60 nm; US Research Nanomaterials Inc., Houston, TX), aluminum oxide nanoparticles (Al_2O_3, alpha, 99+%, 80 nm, hydrophilic; US Research Nanomaterials Inc., Houston, TX), and silicon dioxide nanoparticles (SiO_2, 98+%, 60-70 nm, amorphous; US Research Nanomaterials Inc., Houston, TX) were dried for 12 hours under vacuum prior to use in foam synthesis.

4.2.2 Synthesis and characterization of SMP nanocomposites

4.2.2.1 General procedure for SMP foam synthesis

SMP foams were synthesized with nanoparticles using the procedure described by Hasan *et al.*[114] Isocyanate (NCO) pre-polymer was synthesized with appropriate molar ratios of HPED, TEA, and TMHDI, with a 35 wt% hydroxyl (OH) content. Nanoparticles were physically mixed into the NCO pre-polymer at the appropriate concentrations prior to foam blowing. A OH mixture was prepared with the remaining molar equivalent of HPED and TEA. During foam blowing, foaming agents, including catalysts, surfactants, DI H_2O, and Enovate, were mixed with the NCO-prepolymer and the OH mixture using a FlackTek speedmixer (FlackTek, Inc., Landrum, SC). The resulting foams were cured at 90°C for 20 minutes. The SMP foam nanocomposites were cooled to room temperature (21 ± 1°C) before further characterization. Post-cure purification of the SMP foams included sonication in IPA or reverse osmosis (RO) water

in 15 minute cycles. The purified foams were dried overnight at 55°C under vacuum. **Table 4.1** shows the chemical components and filler concentrations of the SMP nanocomposites characterized in this study.

4.2.2.2 Density and porosity

SMP foam density (n=3) was quantified using foam blocks from the top, middle, and bottom section of the foam, as required by ASTM standard D-3574. Foam block mass was measured and recorded, and length, width, and height values were measured three times using a digital caliper. Porosity was calculated using Equation 4.1. Density of the non-porous neat polymer was calculated without contribution from foaming agents, such as catalysts, surfactants, DI water, and Enovate.

$$\textbf{Porosity}\ (\%) = \left(\frac{\boldsymbol{\rho_{neat} - \rho_{foam}}}{\boldsymbol{\rho_{neat}}}\right) * \mathbf{100} \qquad \text{(Eq. 4.1)}$$

4.2.2.3 Filler dispersion

A small sample section (2 mm x 4 mm) was cut and embedded into a flat mold with Polybed 812 (Polysciences, Inc., Warrington, PA), which was then polymerized at 60°C for 24 hours. The sample resin block was sectioned under ambient conditions, using a Leica UC6 microtome (Leica Microsystems, Wetzlar, Germany) and DiATOME diamond knives (DiATOME, Hatfield, PA). Ultra-thin sections (70 nm) were examined by JEOL 1200EX II electron microscopy (Jeol, Peabody, MA). Transmission electron microscope (TEM) images were processed and analyzed using Image J software (NIH, Bethesda, MD) to quantify average particle diameter (nm) and nearest neighbor distance

(nm). The dispersion parameter (D) was quantified using the average particle area (μ) and the standard deviation of the particle area (σ), as shown in Equation 4.2. [116]

$$\mathbf{D} = \frac{\mathbf{0.2}}{\sqrt{\mathbf{2\pi}}} \cdot \frac{\boldsymbol{\mu}}{\boldsymbol{\sigma}} \qquad \text{(Eq. 4.2)}$$

4.2.2.4 Thermal analysis

The glass transition temperature (T_g) under wet and dry conditions was evaluated for each SMP foam composition (n=5). For dry T_g, 3-8 mg foam samples were cut and stored in a dry container with desiccant prior to analysis. A Q-200 DSC (TA Instruments, Inc., New Castle, DE) was used to obtain the thermogram for each composition. In the first cycle, the temperature was decreased to -40°C at 10°C·min^{-1} and held isothermally for 2 minutes. The temperature was then increased to 120°C at 10°C·min^{-1} and held isothermally for 2 minutes. In the second cycle, the temperature was reduced to -40°C at 10°C·min^{-1}, held isothermally for 2 minutes, and raised to 120°C at 10°C·min^{-1}. T_g was recorded from the second cycle using the inflection point of the thermal transition curve analyzed with TA instruments software (TA Instruments, Inc., New Castle, DE). The aluminum pan was not vented during this step. For wet T_g, 3-8 mg foam samples were submerged in RO water at 50°C for 5 minutes to allow full plasticization. After the samples were removed from water, they were pressed dry with Kim Wipes (Kimberly-Clark Professionals, Roswell, GA), weighed, and placed in an aluminum pan sealed with a vented aluminum lid. Q-200 DSC was used to cool the samples to -40°C and hold them isothermally for 2 minutes. The samples were then heated to 80°C at 10°C·min^{-1}. TA instruments software (TA Instruments, Inc., New

Castle, DE) was used to generate the thermogram and acquire the T_g after water plasticization using the average inflection point of the thermal transition.

4.2.2.5 SMP foam actuation

Cylindrical foam samples (n=3) were prepared with a diameter of 4 mm and a height of 10 mm. A 203.20 μm diameter nickel-titanium (Nitinol) wire (NDC, Fremont, CA) was threaded through the center of the sample along its length to serve as a stabilizer. The foam samples were radially crimped to their smallest possible diameter using an ST 150-42 stent crimper (Machine Solutions, Flagstaff, AZ) by heating the material to 100°C, holding it isothermally for 15 minutes, and programming the foams to the crimped morphology. Initial foam diameter was measured for each sample and SMP foam composition using Image J software (NIH, Bethesda, MD). The foams were placed in a water bath at 50°C, and images were taken at 30 seconds, 1 minute, each minute thereafter up to 15 minutes, and every 5 minutes up to 30 minutes. Foam diameter was measured at each time point using Image J. Percent volume recovery (%) was calculated using Equation 4.3, and volume expansion was calculated using Equation 4.4.

$$\%\ \text{Volume Recovery} = \left(\frac{\text{Recovered diameter}}{\text{Original diameter}}\right)^2 * 100 \qquad \text{(Eq. 4.3)}$$

$$\text{Volume Expansion} = \left(\frac{\text{Recovered diameter}}{\text{Compressed diameter}}\right)^2 \qquad \text{(Eq. 4.4)}$$

4.2.2.6 Thermal stability

Thermal stability of the SMP nanocomposites was determined using thermogravimetric analysis (TGA). 15-20 mg samples (n=3) were prepared from the

cleaned foams. An alumina pan was used to hold all samples and tared before each run. The samples were heated from 25°C to 600°C at 10°C·min^{-1} under nitrogen flow of 50 mL·min^{-1} using a TGA Q 50. At 600°C, the gas was switched to air flow at 50 mL·min^{-1}, and the samples were heated to 800°C. The thermograms were evaluated using TA Universal Analysis software, and percent mass loss (%) versus temperature (°C) curves were graphed for each nanocomposite.

4.2.2.7 Mechanical analysis

Uniaxial tensile loading tests were conducted to determine tensile strength (kPa), toughness (J·m^{-3}) and strain at break (%) of all nanocomposites. The tests were carried out using an Insight 30 Material Tester (MTS Systems Corporation, Eden Prairie, MN) at a constant strain rate of 5 mm·min^{-1} at room temperature. Ten foam samples per foam composition (L= 25 mm, W= 15 mm, H= 3 mm) were cut from the bulk material. Wood tabs were secured on each end of the foam using epoxy to prevent sample deformation in the grips during testing. The resulting stress-strain curves were used to evaluate the mechanical properties of SMP nanocomposites.

4.2.2.8 Particulate analysis

Evaluation of particulate content was conducted in accordance with USP 788, a guidance document for particulate matter in injections. The particulate levels were measured using the light obscuration method with ChemTrac PC5000 (Chemtrac Inc., Norcross, GA). Foam cylinders (n=5) with 8 mm diameter and 3 cm length were cut from each SMP nanocomposite. The samples were tumbled 20x in 100 mL DI water,

and the resulting suspension was processed with the particle counter to acquire a particle count for each composition. Due to the high sensitivity of the particle counter, baseline counts were taken prior to each experiment.

4.2.2.9 Leachable analysis.

Inductively coupled plasma mass spectrometry (ICP-MS) was used to determine the concentration of extractable metals from SMP composites. Approximately 1 g of SMP composite foams were completely immersed in 500 mL of RO water at 37°C. At 1, 4, 8, 12 and 16 days, the solute was removed and concentrated down to approximately 30 mL. After removal, another 500 mL was added to the samples. To prepare samples for ICP, 150 µL of nitric acid was added to each extraction, and standard solutions ranging from 0.1 ppb to 100 ppm were used to generate standard curves for silicon, aluminium and tungsten, respectively. Analysis was performed using a Perkin Elmer DRCII ICP-MS (Perkin Elmer, Waltham, Massachusetts). The concentration of each respective extractable was determined and subtracted from the total concentration of leachables per sample.

4.3 Results and discussion

4.3.1 Density and porosity

All SMP nanocomposites maintained ultra-low densities and high porosity (>98%) which allow the foam to be compressed to small configurations, Table 4.1. There was minimal variation in densities with changing filler type and concentration, indicating uniformity in the foam morphology. The foam density for all compositions

remained close to that of the control, within the range 0.012-0.017 $g \cdot cm^{-3}$, and a neat density of approximately 1 $g \cdot cm^{-3}$ was obtained for the control and all nanocomposites. These results indicate that the fillers do not have a drastic effect on foam cell uniformity at the low concentrations employed in these studies.

Table 4.1: Physical properties of the SMP foam nanocomposites. The SMP consisted of 67 mol% HPED, 33 mol% TEA, and 100 mol% TMHDI.

Composition	ρ_{foam} ($g \cdot cm^{-3}$)	ρ_{neat} ($g \cdot cm^{-3}$)	Porosity (%)	Dry T_g (°C)	Wet T_g (°C)
Control	0.015 ± 0.001	1.019	99	58 ± 2	34 ± 1
0.5% Al_2O_3	0.016 ± 0.001	1.024	98	63 ± 3	36 ± 1
1% Al_2O_3	0.014 ± 0.001	1.024	99	64 ± 1	35 ± 1
2% Al_2O_3	0.015 ± 0.001	1.029	99	64 ± 2	36 ± 1
3% Al_2O_3	0.013 ± 0.001	1.039	99	63 ± 1	35 ± 1
4% Al_2O_3	0.012 ± 0.001	1.049	99	62 ± 1	36 ± 1
5% Al_2O_3	0.015 ± 0.001	1.022	99	62 ± 1	35 ± 1
0.5% SiO_2	0.013 ± 0.001	1.026	99	68 ± 2	36 ± 2
1% SiO_2	0.013 ± 0.001	1.032	99	65 ± 1	35 ± 1
2% SiO_2	0.017 ± 0.001	1.023	98	65 ± 1	35 ± 1
0.5% W	0.017 ± 0.001	1.027	98	59 ± 3	36 ± 1
1% W	0.013 ± 0.001	1.034	99	60 ± 1	37 ± 1
2% W	0.014 ± 0.001	1.042	99	58 ± 1	38 ± 0
3% W	0.013 ± 0.001	1.050	99	56 ± 1	36 ± 1

4.3.2 Filler dispersion

Dispersion of the nanoparticles was heavily dependent on the concentration and filler type. **Table 4.2** shows the dispersion parameter (D) values for a range of nanocomposites. Higher D values were indicative of better particle dispersion with fewer aggregates. [116]

Table 4.2: Dispersion parameter values of the SMP nanocomposites.

Composition	Dispersion Parameter (D)
Control	-
1% Al_2O_3	0.025
3% Al_2O_3	0.012
5% Al_2O_3	0.021
0.5% SiO_2	0.014
1% SiO_2	0.007
2% SiO_2	0.010
0.5% W	0.008
1% W	0.037
3% W	0.028

For Al_2O_3-loaded polymer, low filler concentration (1%) showed the greatest improvement in dispersion while the D values for W-loaded SMPs improved with higher filler concentrations (≥1%). SiO_2-loaded foams had low D values, which indicated high aggregate formation and poor mixing of the nanoparticles within the polymer matrix. The formula for D only takes into account the greyscale area of nanoparticles in an image relative to the background and the standard deviation of the area. Larger areas are indicative of both individual nanoparticles with good dispersion and aggregates with poor dispersion. To address this issue, qualitative analysis of aggregate size was performed using transmission electron micrographs, **Figure 4.1**.

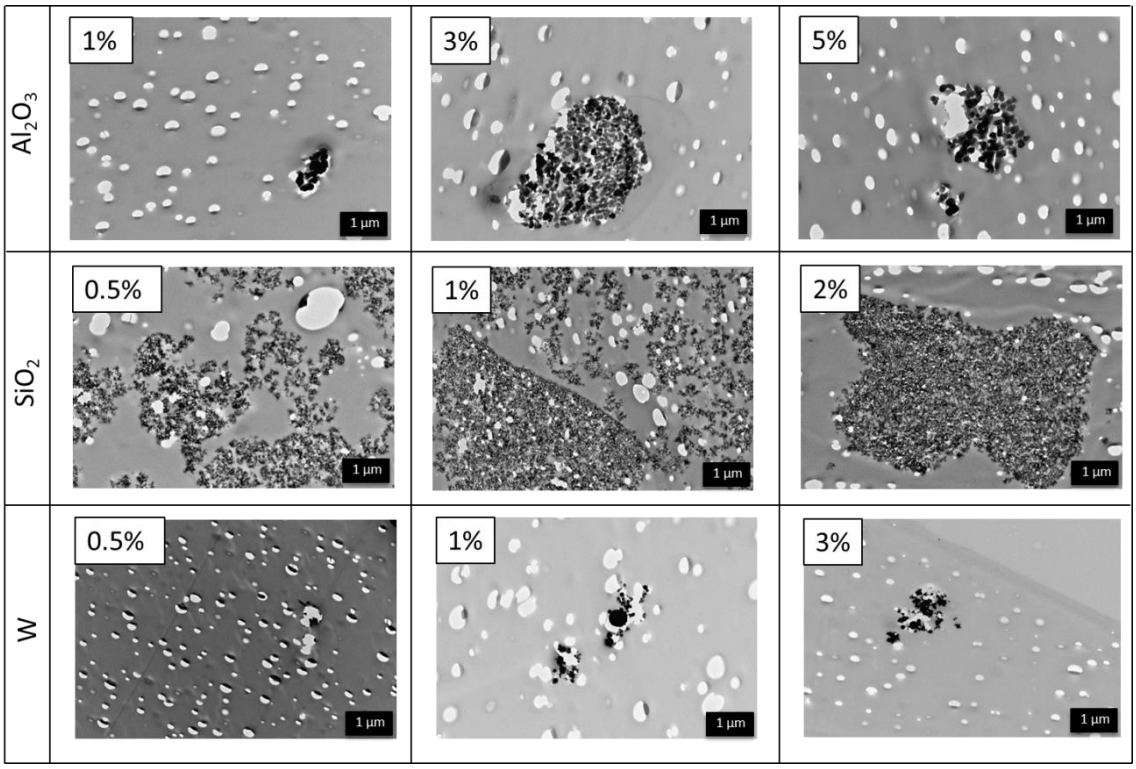

Figure 4.1: TEM images of various SMP nanocomposites at 10x magnification.

At low filler concentration, W and Al_2O_3-loaded systems have small particle aggregates. The aggregate size increased with increasing concentration. SiO_2-loaded systems exhibited aggregate formation even at low concentrations due to phase separation and poor mixing of the hydrophilic nanoparticles into the polymer matrix. **Figure 4.2** shows the average aggregate diameter and nearest neighbor distance of the three different nanoparticle types in all SMP composites. Large aggregate diameters (≥200 nm) and nearest neighbor distances (≥ 100 nm) are indicative of poor dispersion. Approximately 80% of all the Al_2O_3 nanoparticle aggregates were 50 nm in diameter, close to the original particle size of 80 nm, while less than 20% were ≥200 nm.

Furthermore, approximately 80% of all Al_2O_3 nanoparticles had a nearest neighbor distance of ≤100 nm, while approximately 20% were farther apart than 1000 nm. These results suggest uniform dispersion of Al_2O_3 within the various SMP composites. Comparatively, ~40% of all the SiO_2 and W aggregates were 50 nm, while the remaining aggregates (~60%) were ≥200 nm. These larger aggregates indicate non-homogenous dispersion, as the original particle size was 40-60 nm and 60-70 nm for W and SiO_2, respectively. All compositions experienced filler agglomeration, as shown by the aggregate size of ≥500 nm; however Al_2O_3-loaded nanocomposites had the least aggregate formation. Nearest neighbor distance for all SiO_2 and W-loaded foams was within 100-1000 nm, suggesting poor filler dispersion within the polymer matrix. Overall, Al_2O_3 served as the better filler with uniform dispersion and reduced aggregate formation compared to W and SiO_2.

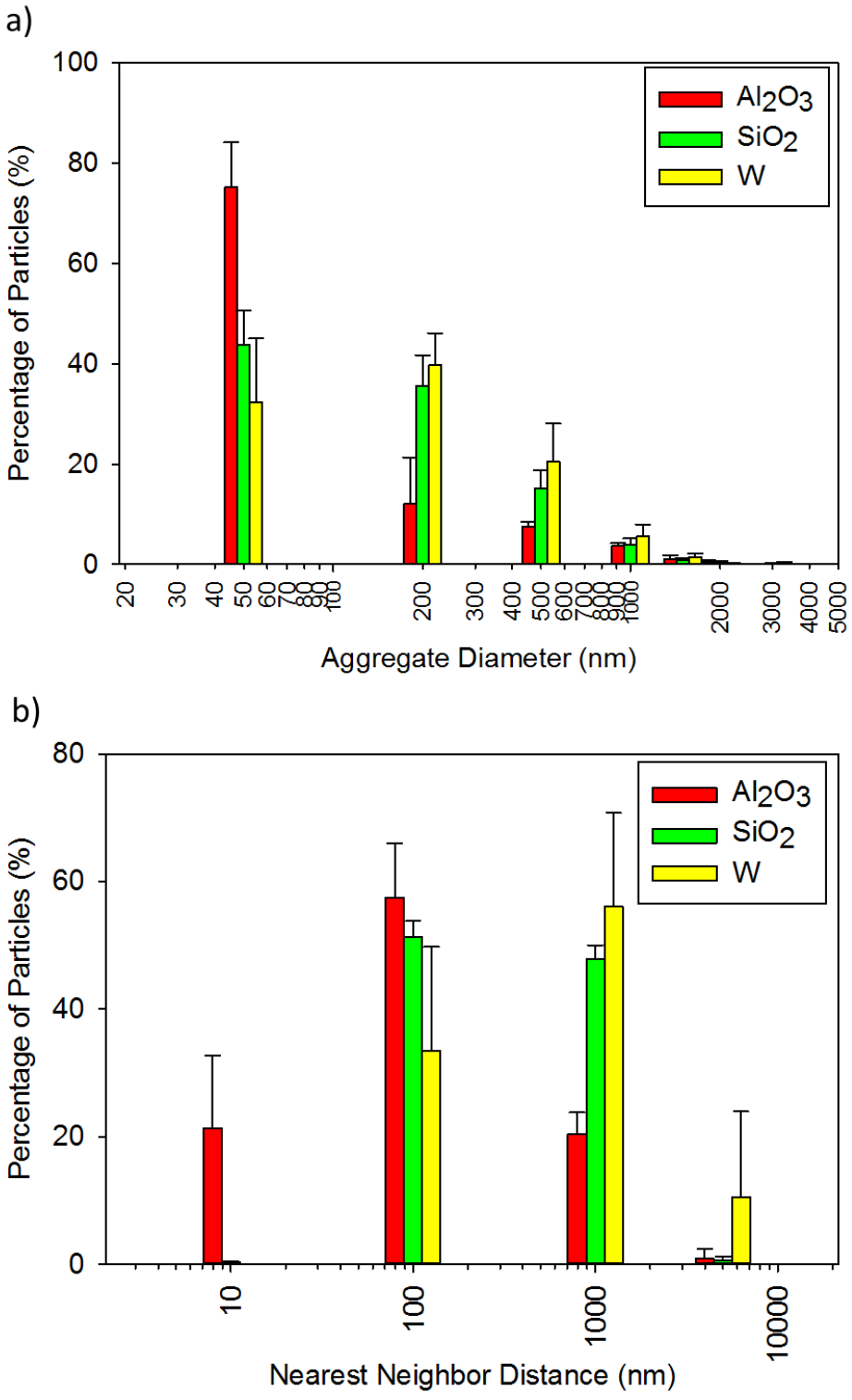

Figure 4.2: Average aggregate diameter (a) and nearest neighbor distance (b) for the selected nanoparticles.

4.3.3 Thermal transitions and foam actuation

Filler addition had minimal effect on the dry thermal transitions of the W and Al_2O_3 nanocomposites as indicated by differential scanning calorimetry (DSC), Table 4.1. These foams had glass transition temperatures (T_g's) within 5°C of the control foam. However, 0.5% SiO_2-loaded foams showed a 10°C increase in T_g, suggesting restricted chain mobility due to an increase in the physical net points of the polymer. The wet T_g's of all nanocomposites were similar to that of the control due to increased chain flexibility upon water plasticization of the polymer system.

Actuation kinetics of the SMP nanocomposites were dependent on the concentration and filler type. **Figure 4.3** shows changes in foam diameter upon exposure to heat in an aqueous environment. For Al_2O_3 nanocomposites, the foams underwent faster actuation (< 5 minutes) with higher filler loadings (>3%), compared to the control, as indicated by the inflection point of the curves. The Al_2O_3-loaded SMP systems also showed greater diameter recovery with increased filler content. Similarly, W nanocomposites had faster actuation profiles and greater diameter recovery for the higher-loaded foams, as indicated by a 3 minute actuation time with 3% W versus an 8 minute actuation time for the control. Increasing filler content resulted in more physical crosslinks in the system to serve as net points that play a critical role in SMP shape recovery and shape memory. Entropic recovery of SMPs is dependent on the net points within the system hence, increasing net points and good nanoparticle/polymer bonding allowed for greater material recovery and expansion. [117, 118] Within the SiO_2-loaded nanocomposites, the fastest actuation was observed with 0.5% filler. At higher

concentrations (>1%), diameter recovery and shape memory of the composite decreased. Due to its reduced molar mass, relatively high numbers of SiO_2 nanoparticles were required to achieve similar weight compositions to that of to Al_2O_3 and W, which disrupted the polymer matrix and limited mobility at the nanoscale.

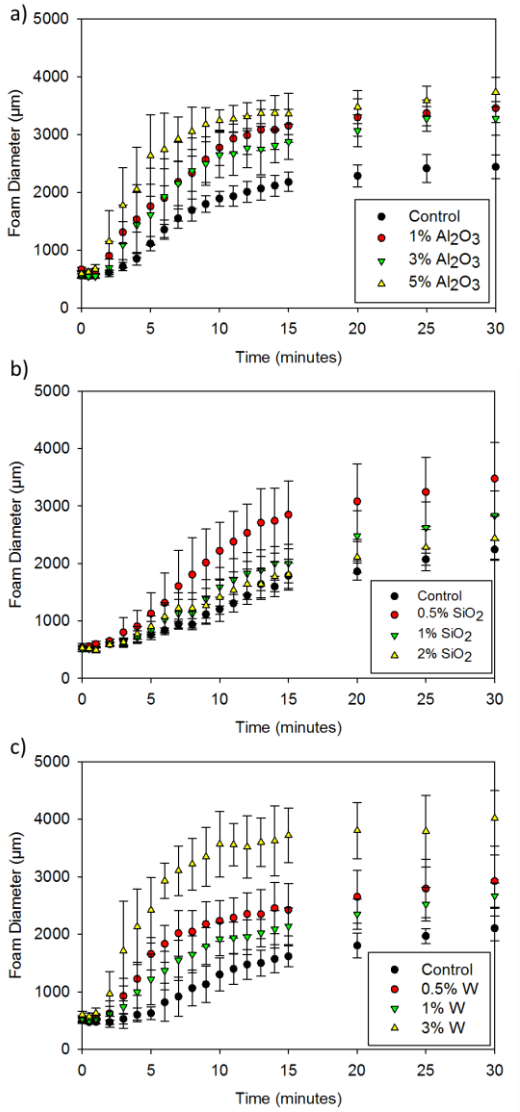

Figure 4.3: Actuation profiles of a) Al_2O_3, b) SiO_2, and c) W nanocomposites in 50°C RO water. Original diameter of all foam cylinders was 4000 µm.

Volume recovery (%) and volume expansion (x) of the nanocomposites, **Table 4.3**, support the variations in shape memory behavior observed as a result of particle type and concentration. Higher filler content SMP foams had greater shape recovery relative to the uncompressed geometry and higher volume expansion compared to the compressed foam. Low concentration (0.5%) W-loaded foams had a volume recovery of 53 ± 16% and volume expansion of 35 ± 16x. Increased filler concentration (3%) resulted in greater recovery (96 ± 20%) and expansion (47 ± 17x). Similarly, Al_2O_3-loaded foams had an increase in volume recovery from 23 ± 5% to 82 ± 13% at 0.5% and 5% loadings, respectively. SiO_2-loaded foams had the greatest volume recovery and expansion for 0.5% at 77 ± 27% and 43 ± 11x, respectively. Bonding of SiO_2 to the polymer was decreased due to differences in hydrophobicity of the two components, resulting in aggregate formation within the SMP foam. The presence of aggregates disrupted the polymer matrix and resulted in lower shape recovery and longer actuation times. Higher SiO_2 filler loading restricted chain mobility and disrupted polymer-polymer interactions, causing a diminished shape memory effect, as demonstrated by the actuation profiles.

Table 4.3: Volume expansion (%) and volume recovery of various SMP nanocomposites.

Composition	Volume Recovery (%)	Volume Expansion (x)
Control	32 ± 5	18 ± 1
0.5% Al_2O_3	23 ± 5	17 ± 6
1% Al_2O_3	75 ± 12	27 ± 5
2% Al_2O_3	68 ± 13	41 ± 6
3% Al_2O_3	66 ± 12	36 ± 7
4% Al_2O_3	58 ± 11	33 ± 7
5% Al_2O_3	82 ± 13	42 ± 12
0.5% SiO_2	77 ± 27	43 ± 11
1% SiO_2	52 ± 16	31 ± 10
2% SiO_2	40 ± 12	22 ± 6
0.5% W	53 ± 16	35 ± 16
1% W	45 ± 6	26 ± 7
2% W	83 ± 15	57 ± 7
3% W	96 ± 20	47 ± 17

4.3.4 Thermal stability and mechanical properties

Thermal characterization of the nanocomposites using TGA suggested improved thermal stability of the SMP systems with the addition of Al_2O_3 and SiO_2 fillers. **Figure 4. 4** shows weight change (%) as a function of temperature for all SMP nanocomposites. Al_2O_3 nanocomposites exhibited greater thermal stability with the addition of nanoparticles, as compared to the control foam. The thermal decomposition temperature of the alumina composites increased by 30°C, as shown by the midpoint of the weight change curve, indicating improved thermal sensitivity of the polymer system. Silica-loaded composites had a filler concentration-dependent increase in thermal decomposition temperature. The control (unloaded) foam experienced decomposition at 300°C, which increased to 350°C with the 2% SiO_2 nanocomposites. A 50°C increase in

thermal decomposition temperature is indicative of improved thermal resistance. W-loaded SMP systems had minimal change in thermal stability compared to the control, suggesting the requirement of higher filler loading to achieve thermally-resistive nanocomposites.

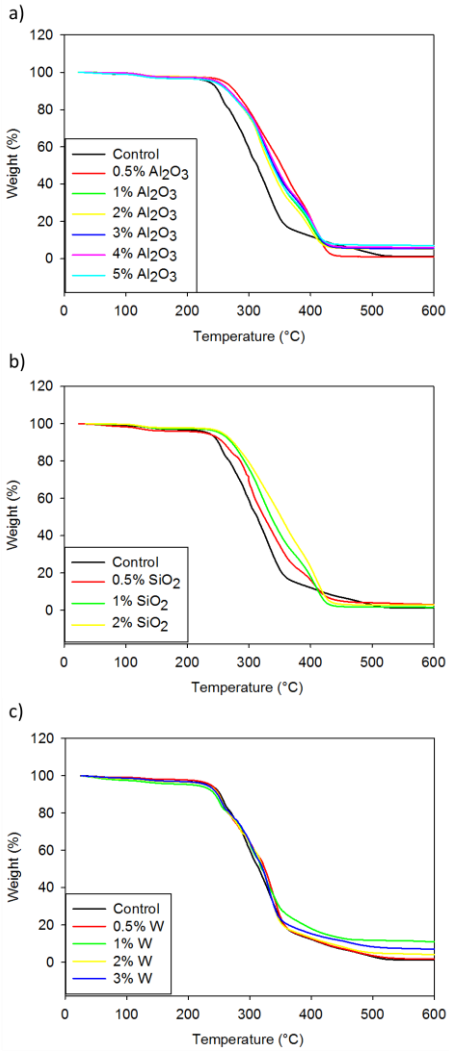

Figure 4.4: Weight (%) versus temperature (°C) curves for a) Al_2O_3, b) SiO_2 and c) W nanocomposites. Al_2O_3 and SiO_2 nanocomposites had increased thermal stability, as indicated by an increase in thermal degradation temperature, while W nanocomposites had minimal thermal improvement.

Mechanical analysis of the foams revealed improved toughness and composite strength at low filler concentrations. **Figure 4.5** shows ultimate tensile strength, toughness, and strain at break for nanocomposites with the three fillers. SMP foams with 0.5% Al_2O_3 had the highest tensile strength (127 kPa) and toughness (347 $J \cdot m^{-3}$) compared to the control, which had a tensile strength and toughness of 84 kPa and 230 $J \cdot m^{-3}$, respectively. Improved strength and toughness can be attributed to the nanoparticle/polymer bonding where increased bonding results in greater mechanical stability. [119, 120] The interactions between Al_2O_3 and the SMP allowed for the generation of physical net points that resisted mechanical deformation more effectively than the control systems. Additionally, 0.5% Al_2O_3-loaded foams had the highest strength and toughness compared to all other nanocomposites. Higher concentrations ($\geq$ 2%) of Al_2O_3 resulted in decreased strain at break compared to the control and other nanocomposite systems. SiO_2 and W-loaded foams had improved mechanical properties compared to the control. In general, higher nanoparticle concentrations resulted in decreased strength and toughness. However, toughness improved from 217 $J \cdot m^{-3}$ to 302 $J \cdot m^{-3}$ as SiO2 concentration increased from 0.5% to 1%.These results indicate that filler incorporation into the SMP systems improved mechanical properties by reinforcing the polymer matrix. Filler particles serve as physical crosslinks that improve thermal stability and toughness of the composites, which is beneficial for the development of viable biomedical implants. Furthermore, the nanocomposites were more resistant to tear compared to control foams, indicating their potential for improved resilience to fracture and shearing during device processing.

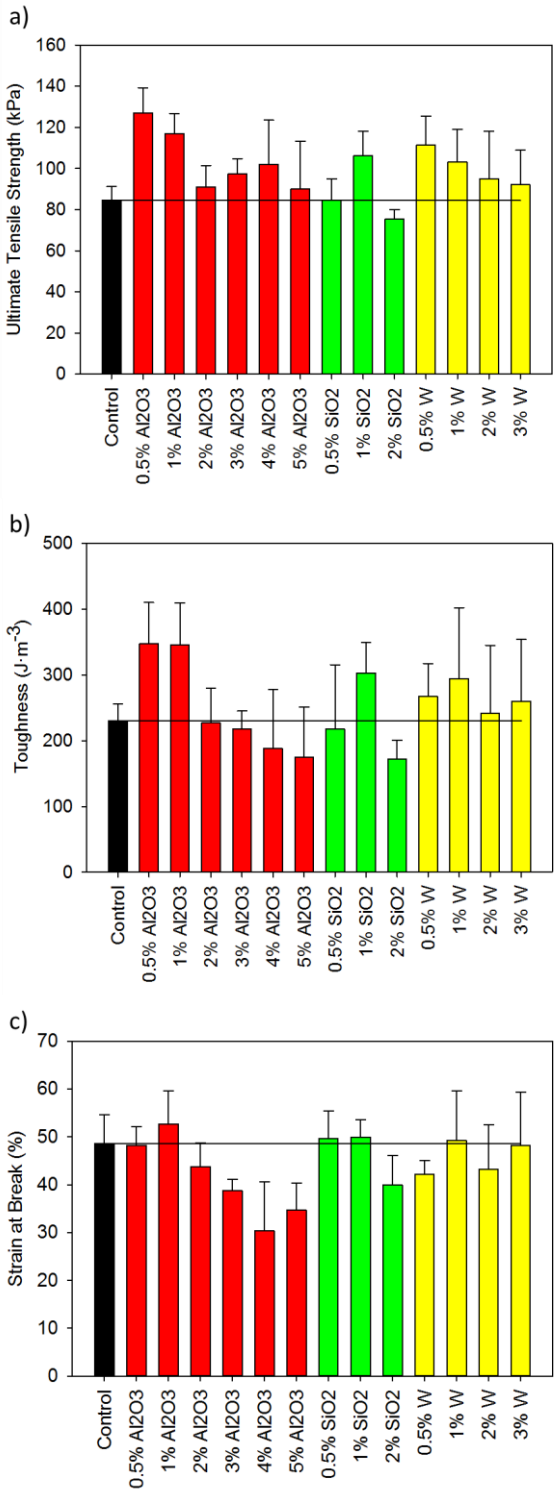

Figure 4.5: Mechanical properties of SMP foams. a) Ultimate tensile strength (kPa), b) toughness ($J \cdot m^{-3}$) and c) strain at break (%) of SMP nanocomposites compared to non-loaded foams.

4.3.5 Particulates and leachables

Quantification of particulate matter is shown in **Figure 4.6**. Particulate analysis of the nanocomposites indicated that the particulate levels were below the limits stated in USP 788 for particles ≥10 μm and ≥25 μm. [121] Specifically, the limit for particles ≥10 μm is 6000, and the maximum value from any nanocomposite was 812 ± 201. Similarly, the maximum value recorded for particles ≥25 μm was well below the threshold value of 600. This data indicates that there is minimal risk of producing dangerous levels of emboli in the parent vessel of the aneurysm. Figure 4.6 shows that SiO_2 nanocomposites exhibited a general increase in particulate generation as weight percentage was increased, while W and Al_2O_3 nanocomposites showed no discernible trend in particulate generation for all size ranges. When compared to the control, the 0.5% nanocomposites had lower or equivalent counts of particulates ≥10 μm. Assuming that low particulate generation is associated with less brittle fracture and improved mechanical properties, the results in Figure 4.6a agree with those in Figure 4.5a. For both the Al_2O_3 and W nanocomposites, 0.5% concentrations resulted in increased ultimate tensile strength and reduced particulates ≥10 μm (271 ± 61 and 340 ± 90 for Al_2O_3 and W, respectively) compared to the control (360 ± 50). At low concentrations, the nanoparticles provided mechanical reinforcement to the polymer system and yielded comparable particulate counts to that of the control foams for particles ≥10 μm and ≥25 μm. Conversely, increased filler concentration lowered material toughness and resulted in larger particulate counts.

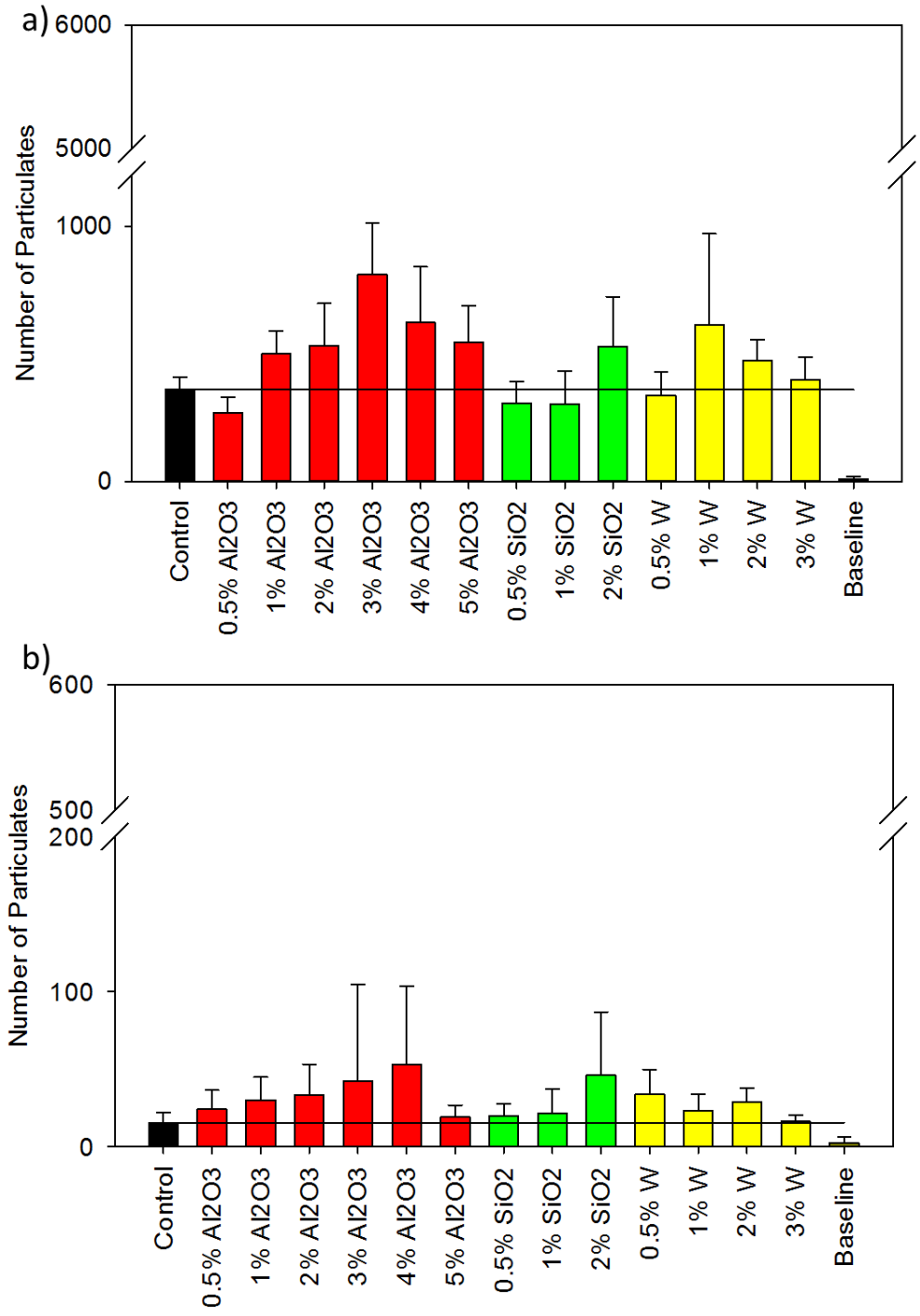

Figure 4.6: Particulate count of SMP nanocomposites and control. a) Threshold: 6000 particles ≥10 µm. b) Threshold: 600 particles ≥25 µm. All particulate testing was conducted in compliance with USP 788.

Quantification of metal leachables from the SMP foams is shown in **Figure 4.7**. Our previous work shows that the foam occludes within the first 30 minutes *in vivo* and should therefore not be exposed to additional flow that induces leaching after this time frame. However, leachables were evaluated for 16 days, as that is the critical time period for nanoparticle release from the foam and into the blood stream. Al_2O_3 nanocomposites (Figure 4.7a) had minimal filler leaching over 16 days with the highest recorded leachable concentration of 1.48 μg/mL. According to Virgilio *et al*., aluminium nanoparticles had a cytotoxic and genotoxic effect on Chinese hamster ovary cells (CHO-K1) at concentrations of 100 μg/mL. [122] The leachable concentration of Al_2O_3 from SMP foams was well below this toxicity threshold, and is therefore unlikely to affect material cytocompatibility. Similarly, SiO_2-loaded SMPs experienced minimal filler leaching with the exception of a peak release of 5.33 μg/mL from the 0.5% silica foam at 12 days (Figure 4.7b). SiO_2 concentrations released from the foams remain below the toxic thresholds found by Hashimoto *et al*. Namely, SiO_2 nanoparticle concentrations greater than 200 μg/mL resulted in cytotoxicity and genotoxcity in murine macrophages. [123] The concentrations of SiO_2 leachables remained below 6 μg/mL throughout this study, indicating their likely safety for biomedical applications.

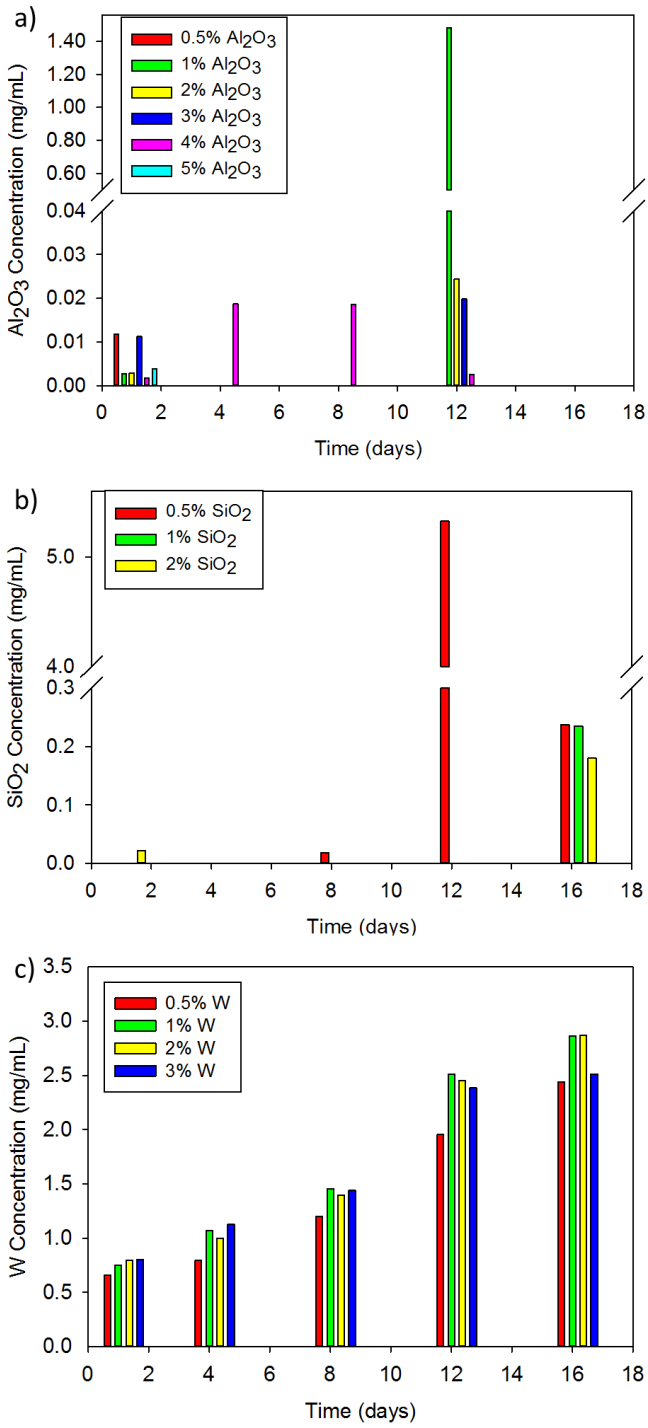

Figure 4.7: Leachable analysis of various concentrations of a) Al_2O_3 b) SiO_2 and c) W nanoparticles from SMP foams over 16 days.

W nanoparticles were increasingly released over 16 days with the maximum concentration of 2.87 μg/mL (Figure 4.7c). Hussain *et al*. evaluated the cytotoxic effects of W nanoparticles on rat liver cells. Nanoparticle concentrations below 100 μg/mL had minimal effects on mitochondrial function and cellular morphology. [124] W release from SMP foams are therefore unlikely induce cytotoxicity at the low concentrations recorded here (< 3 μg/mL). While the leachable analysis is promising, further biocompatibility studies are required with various cell types and animal models to fully understand the effects of each of the three fillers on the metabolic activity of cells and their accumulation in various organs.

The SMP nanocomposites developed in this study would serve as porous polymer scaffolds for a foam-over-wire neurovascular embolic device. The nanocomposites demonstrated tunable thermo-mechanical properties with minimal filler leaching and particulate generation, well below the accepted threshold values, making them optimal for implantable devices. Due to the low particulate count for all nanocomposites, there is minimal risk of downstream embolization of the parent vessel after foam-over-wire device deployment. Additionally, all nanocomposites maintained their ultra-low densities and high porosities for large volumetric filling of the aneurysms along with controllable actuation profiles that provide another degree of control over device specification. Overall, these nanocomposites serve as a platform for device design for neurovascular embolization and have strong indications as implantable biomaterials.

4.4 Conclusions

SMP foams were fabricated with three different filler types (Al_2O_3, SiO_2, W) at varied concentrations to achieve tunable shape recovery, mechanical properties, and thermal stability. Higher filler concentrations resulted in increased aggregate formation in the polymer; however, the foams maintained the ultra-low density and high porosity required for volumetric occlusion. Toughness and strain at break improved for the SMP nanocomposites at low nanoparticle loadings with selected filler types (Al_2O_3 and SiO_2). Particulate generation increased at high filler concentrations, but all particulate counts remained below the acceptable thresholds for USP 788. Filler leaching from the nanocomposites was minimal relative to cytotoxic concentrations reported in literature, indicating the safety of these SMP foams as biomaterials. The SMP nanocomposites developed through this research have a potential to improve medical implants, pending further investigation of *in vivo* biocompatibility and particle generation.

CHAPTER V

DEVELOPMENT OF SILOXANE-POLYETHYLENE GLYCOL SURFACTANTS TO CONTROL SMP FOAM MORPHOLOGY

5.1 Introduction

Shape memory polymers (SMPs) are "smart" materials that have the capability of shape change from a programmed secondary shape to a primary shape upon the input of an external stimulus, such as heat, light, or electricity. [1-3] For thermal actuation, the polymer can be synthesized in a primary shape, heated above its transition temperature (T_{trans}), and mechanically programmed into a secondary shape. [4] Once cooled below the transition temperature, the material will remain in the secondary shape until it is heated again to return to its original shape. [4] Shape fixity occurs when the polymer chains are forced to align into conformations with net orientation and cooled below the actuation transition to restrict chain mobility. [5] Entropic recovery to the polymer chain equilibrium random orientation then drives the return to original shape. [5] Due to this shape memory behavior, SMPs have a wide range of uses in medical and industrial applications, such as vascular stents, occlusion devices, and self-controlled actuators. [1, 6]

Polyurethanes are an extremely versatile class of polymers that have the capability to be biocompatible, biodegradable, and have tunable mechanical properties. [36] These characteristics make polyurethanes optimal for use *in vivo.* Wilson *et al*. developed highly crosslinked, amorphous SMPs using aliphatic polyurethanes for use in medical devices. [5] These materials have high recovery stresses due to a high level of crosslinking, tunable T_g's, and good shape recovery. [5] In an effort to increase the surface

area, Singhal *et al*. synthesized the polyurethane SMPs developed by Wilson as foams with low density and high porosity. [19] Open-celled SMP foams provide a substrate for increased cellular infiltration and adhesion, as well as flow stagnation and recirculation zones, resulting in rapid formation of a stable thrombus upon contact with blood. [6, 37] Rodriguez *et al*. evaluated the biocompatibility of the SMP foams in a porcine model and observed minimal inflammation at 90 days. [38] These properties make SMP foams ideal for use as three-dimensional tissue scaffolds for biomedical applications.

Surfactants allow spreading at the polymer air interface *via* the Gibbs-Marangoni effect. [125, 126] Namely, surfactants lower the surface tension at the polymer interface, thereby causing flow from high surface tension areas to low surface tension areas. In polyurethane foaming, surfactants stabilize individual foam cells through a change in the surface tension gradient. [125] Polyurethane foams are fabricated by addition polymerization of diisocyanates with alcohols. [49, 127] This foaming process occurs in four steps: (i) bubble generation and growth, also known as the cream time; (ii) bubble packing and cell stabilization; (iii) polymer stiffening and cell opening, or gel time; and (iv) final curing, or tack-free time. Typically, surfactants used in flexible polyurethane foaming systems do not alter the reaction kinetics of the process. However, in the absence of surfactants, the foaming system will experience coalescence and eventual collapse. [49] During foaming, the bubbles introduced into the system by mechanical mixing will grow. As the volume fraction of the gas bubbles exceeds 74%, the spherical bubbles distort into multisided polyhedrals with struts. Due to capillary pressure, the pressure within the struts is lower than that in the cells. The pressure difference causes

the polymer liquid in the struts to drain. Without surfactants, this drainage rate will be very fast, causing cell rupture and bubble coalescence. The surfactants are adsorbed at the air-alcohol interface and have a significant effect on bubble generation, cell stabilization, strut thickness, and final cell size, in addition to foam porosity. These physical foam properties are of concern due of their effect on the mechanical properties of the resulting polymer scaffold.

Silicone surfactants were first introduced in the 1950s for the development of industrial-grade polyurethane foam. [50] They are surface active agents that lower the interfacial surface tension and allow spreading. [50, 128] Typically, surfactants contain a hydrophobic siloxane group attached to a hydrophilic polar molecule. [49, 129, 130] Siloxane-based surfactants have three unique properties: (i) they maintain surface activity in both water and non-aqueous systems, such as oil and polyols; (ii) they are able to lower surface tension to as low as 20 mN/m; and (iii) they remain liquid at very high molecular weights. [50] These unique properties are imparted by the siloxane backbone due to its low glass transition temperature (T_g), its ability to stay liquid at high molecular weights, and the presence of methyl groups that reduce surface tension. Hydrocarbon surfactants containing alkyl hydrophobic groups with primarily $–CH_2–$ groups only lower surface tension to 30 mN/m, making them less effective at allowing spreading at the interface. [50] Additionally, silicone surfactants have different aggregation properties from those of hydrocarbon surfactants, such that they form bilayer phases and vesicles rather than micelles and gel phases. [50, 131]

This research focuses on developing linear surfactants for reliable production of SMP foams with reproducible thermo-mechanical properties and cell structure. Siloxane units served as the hydrophobic components, and polyethylene glycol (PEG) allyl methyl ether acted as the hydrophilic constituent. Hydrosilylation was used to synthesize the amphiphiles, which were then chemically and physically characterized. [50, 132-135] Then, polyurethane foams were fabricated with various surfactant concentrations, and the effects of surfactant structure on foam morphology and thermal properties were evaluated.

5.2 Materials and methods

1,1,1,3,5,5,5-heptamethyltrisiloxane (TS, 97%; Sigma-Aldrich Inc., St. Louis, MO), poly(dimethylsiloxane), hydride terminated (PDMS, M_n ~580 Da; Sigma-Aldrich Inc., St. Louis, MO), toluene (anhydrous, 99.8%; Sigma-Aldrich Inc., St. Louis, MO), chloroform-d ($CDCl_3$, 100%; Sigma-Aldrich Inc., St. Louis, MO), polyethylene glycol allyl methyl ether – Polyglykol AM 350 (PEG-350, n = 8; Clariant, Charlotte, NC), polyethylene glycol allyl methyl ether – Polyglykol AM 1100 (PEG-1100, n = 25; Clariant, Charlotte, NC), platinum(0)-1,3-divinyl-1,1,3,3-tetramethyldisiloxane complex solution (Karstedt's catalyst, Pt; Sigma-Aldrich Inc., St. Louis, MO), tris(triphenylphosphine)rhodium(I) chloride (Wilkinson's catalyst, Rh; Sigma-Aldrich Inc., St. Louis, MO), Fisherbrand™ activated carbon charcoal, 6 to 14 mesh (Fisher Scientific, Pittsburgh, PA), N,N,N',N'-tetrakis(2-hydroxypropyl)ethylenediamine (HPED, 99%; Sigma-Aldrich Inc., St. Louis, MO), triethanolamine (TEA, 98%; Sigma-Aldrich Inc., St. Louis, MO), trimethyl-1,6-hexamethylene diisocyanate, 2,2,4- and

2,4,4- mixture (TMHDI; TCI America Inc., Portland, OR), hexamethylene diisocyanate (HDI; TCI America Inc., Portland, OR), T-131 (Air Products and Chemicals, Inc. Allentown, PA), BL-22 (Air Products and Chemicals, Inc, Allentown, PA), Enovate 245fa blowing agent (Honeywell International, Inc., Houston, TX), 2-propanol 99% (IPA; VWR, Radnor, PA) and deionized (DI) water (> 17 MΩ cm purity; Millipore water purifier system, Millipore Inc., Billerica, MA) were used as received.

All reactions were conducted under a N_2 atmosphere with a Teflon-covered stir bar to agitate the reaction mixture. Chemical structures were confirmed using proton nuclear magnetic resonance (^{1}H NMR) spectroscopy using a Mercury 300 MHz spectrometer operating in the Fourier transform mode with $CDCl_3$ as the standard.

5.2.1 Synthesis of siloxane-polyethylene glycol ether amphiphiles

Siloxane-PEG amphiphiles were synthesized using the protocol detailed by Murthy *et al.* [136] **Figure 5.1** shows the reaction mechanism for the two siloxane units with the appropriate synthetic parameters. Equimolar ratios of TS and PEG allyl methyl ether (n = 8 or 25) were reacted to yield a siloxane-PEG amphiphile using Pt-catalyzed hydrosilylation. Similarly, equimolar ratios of PDMS and PEG allyl methyl ether (n = 8 or 25) were reacted using Rh-catalyzed hydrosilylation. The reaction components were added to a round-bottom (rb) flask equipped with a rubber stopper and heated to 80°C. The reaction progressed for 12 hours, after which its completion was monitored with Fourier transform infrared (FTIR) spectroscopy. An aliquot of the reaction solution was placed on a KBr plate, and the FTIR spectrum was obtained. The disappearance of the Si-H peak at 2155 cm^{-1} suggested complete functionalization. The catalyst was removed

from the product by refluxing the reaction mixture with activated charcoal for 12 hours. The final product was isolated by vacuum filtration and removal of volatiles under reduced pressure.

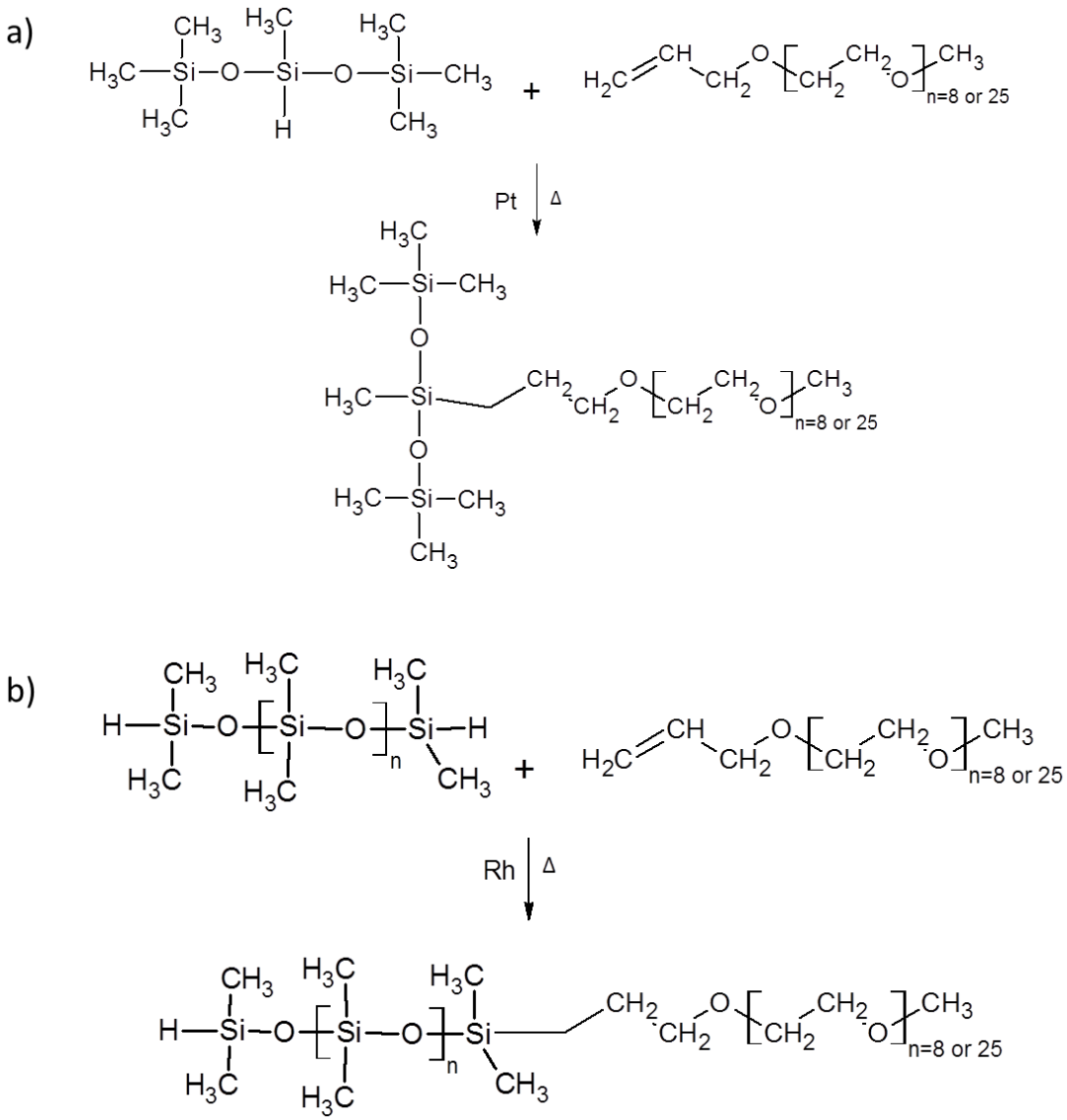

Figure 5.1: Hydrosilyation reaction schematic of a) trisiloxane and b) poly(dimethylsiloxane) hydride terminated with poly(ethylene glycol) allyl methyl ether (n = 8 or 25).

TS (1 mol eq.), PEG allyl methyl ether (n = 8) (1 mol eq.), and 0.003 mol eq. of Karstedt's catalyst were reacted using hydrosilylation in 0.0006 M toluene. The final liquid product, TS-PEG(350), was purified with a yield of 93%. ^{1}H NMR (δ, ppm): -0.2-0.26 (m, 3H, SiC***H₃***), 0.42 (m, 2H, $SiCH_2C$***H₂***), 1.59 (m, 2H, SiC***H₂***CH_2), 3.4 (t, 3H, OC***H₃***), 3.5-3.8 (m, 2H, OC***H₂***C***H₂***).

TS (1 mol eq.), PEG allyl methyl ether (n = 25) (1 mol eq.), and 0.004 mol eq. of Karstedt's catalyst were reacted using hydrosilylation in 0.0003 M toluene. The final solid product, TS-PEG(1100), was purified with a yield of 93%. ^{1}H NMR (δ, ppm): -0.01-0.26 (m, 3H, SiC***H₃***), 0.42 (m, 2H, $SiCH_2C$***H₂***), 1.59 (m, 2H, SiC***H₂***CH_2), 3.4 (t, 3H, OC***H₃***), 3.5-3.8 (m, 2H, OC***H₂***C***H₂***).

PDMS (1 mol eq.), PEG allyl methyl ether (n = 8) (1 mol eq.), and 0.0007 mol eq. of Wilkinson's catalyst were reacted using hydrosilylation in 0.0002 M toluene. The final liquid product, PDMS-PEG(350), was purified with a yield of 93%. ^{1}H NMR (δ, ppm): -0.15-0.65 (m, 3H, SiC***H₃***), 0.95 (m, 2H, $SiCH_2C$***H₂***), 1.6 (m, 2H, SiC***H₂***CH_2), 3.4 (m, 3H, OC***H₃***), 3.5-4.6 (m, 2H, OC***H₂***C***H₂***).

PDMS (1 mol eq.), PEG allyl methyl ether (n = 25) (1 mol eq.), and 0.0007 mol eq. of Wilkinson's catalyst were reacted using hydrosilylation in 0.0001 M toluene. The final solid product, PDMS-PEG(350), was purified with a yield of 97%. ^{1}H NMR (δ, ppm): -0.18-0.56 (m, 3H, SiC***H₃***), 0.50 (m, 2H, $SiCH_2C$***H₂***), 1.59 (m, 2H, SiC***H₂***CH_2), 3.4 (m, 3H, OC***H₃***), 3.5-4.34 (m, 2H, OC***H₂***C***H₂***).

5.2.2 FTIR

1-2 drops of the product were placed on a KBr plate, and FTIR spectra were collected using a Bruker ALPHA Infrared Spectrometer (Bruker, Billerica, MA). Thirty-two background scans of the blank KBr plate were taken followed by sixty-four sample scans of the various surfactant compositions. FTIR spectra were collected in absorption mode at a resolution of 4 cm^{-1}. OPUS software (Bruker, Billerica, MA) was utilized to subtract the background scans from the spectra, to conduct a baseline correction for IR beam scattering, and to perform an atmospheric compensation to remove carbon dioxide peaks. Each composition was measured three times.

5.2.3 Rheometry

A simple shear test was conducted on 1 mL of each surfactant type using a Physica MCR 301 (Anton Paar USA Inc., Ashland, VA). Viscosity was measured under a controlled shear rate of 50 s^{-1} for 120 seconds (6 second intervals, 20 points) for each surfactant. For solid surfactants, the rheometer plate was heated to 40 ± 0.03°C during each run. Viscosity (η) was evaluated using the RheoCompass software (Anton Paar USA Inc., Ashland, VA).

5.2.4 Surface tension

Hydrostatic surface tension measurements of surfactants were carried out using a KSV CAM-2008 Contact Angle Analyzer (KSV Instruments, Ltd., Helsinki, Finland). A 5 μL drop of surfactant was ejected from the tip of the syringe. The drop was allowed to reach equilibrium for 60 seconds, and surface tension was measured using an Attension Tensometer and the Attension Theta software package (Biolin Scientific, Stockholm,

Sweden). Surface tension measurements were collected (n = 3) and presented as the measurement average.

5.2.5 Mass spectrometry

Matrix-assisted laser desorption ionization (MALDI) experiments were performed on a Voyager DE-STR mass spectrometer (Applied Biosystems, Foster City, CA) under optimized conditions in positive linear mode. Ions were generated by a pulsed nitrogen laser at 337 nm and accelerated through 25 kV and 100 laser shots were used per spectrum. trans-2-[3-(4-t-Butylphenyl)-2-methyl-2-propenylidene]malononitrile (DCTB) and potassium trifluoroacetate (KTFA) were used as a matrix and cationization reagent, respectively. The surfactant samples, KTFA, and matrix were prepared at concentration of 1, 10, and 20 mg/mL, respectively. The sample solution was mixed with the matrix and KTFA at a volume ratio of 1:5:1. About 0.5 μL of this mixture was deposited on a stainless steel sample holder. After being allowed to air-dry, the sample was analyzed using MALDI-TOF MS. Mass spectra for all samples were analyzed using

5.2.6 Synthesis of SMP foams

SMP foams were synthesized using the three-step protocol described in previous work. [98, 114] First, an isocyanate (NCO) prepolymer was synthesized with appropriate molar ratios of HPED, TEA, HDI, and TMHDI. These prepolymers were allowed to react for 32 hours with a temperature ramp from room temperature to 50°C and back to room temperature. Next, a hydroxyl (OH) mixture was blended with the remaining molar equivalants of HPED and TEA. This mixture also contained DI water and catalysts. The NCO prepolymer and the OH mixture were combined along with a

physical blowing agent, Enovate, and each of the newly synthesized surfactants, TS-PEG(350), TS-PEG(1100), PDMS-PEG(350), and PDMS-PEG(1100). This mixture was mixed in a FlackTek speedmixer (FlackTek, Inc., Landrum, SC) and poured into a mold. The foam was allowed to cure at 90°C for 20 minutes before cooling to room temperature for further processing. **Table 5.1** shows the weight percent of each component used for foam synthesis. Multiple foams were synthesized with varied concentrations of each surfactant type.

Foams were mechanically programmed by heating them to 90°C and compressing them using a Carver press (Carver, Inc., Wabash, IN). Once cooled, the foams were cleaned using two 15 minute cycles of isopropyl alcohol and four 15 minute cycles of reverse osmosis water under sonication. The foams were placed in aluminum pans and frozen overnight at -20°C. A FreeZone 6 (Labconco, Kansas City, MO) freeze-dryer was used to remove all water from the cleaned foams, after which they were dried overnight under vacuum at 50°C prior to characterization.

5.2.7 Density

Density measurements were conducted on foam blocks acquired from the top, middle, and bottom sections of foams, as outlined in ASTM standard D-3574. [137] The length, width, and height of the cube was measured, the mass of the sample was recorded, and density was calculated in $g \cdot cm^{-3}$. Each foam block was measured three times.

Table 5. 1: Composition of foams synthesized with 100% HDI and 100% TMHDI with various surfactant types and concentrations.

Foam Composition	Surfactant Type	Surfactant (wt %)	TMHDI (wt%)	HDI (wt%)	T-131 (wt%)	BL-22 (wt%)	HPED (wt%)	TEA (wt%)	DI H_2O (wt%)	Enovate (PPH)
100 HDI H67	TS-PEG(350)	0.5	-	65	0.4	1.0	23	8	3	4
		1	-	65	0.4	1.0	23	8	3	4
		4	-	63	0.4	1.0	22	7	3	4
		7	-	61	0.4	0.9	21	7	3	4
100 HDI H67	TS-PEG(1100)	0.5	-	65	0.4	1.0	23	8	3	4
		1	-	65	0.4	1.0	23	8	3	4
		4	-	63	0.4	1.0	22	7	3	4
		7	-	61	0.4	0.9	21	7	3	4
100 HDI H67	PDMS-PEG(350)	0.1	-	65	0.4	1.0	23	8	3	4
		0.25	-	65	0.5	1.4	23	8	3	4
		0.5	-	65	0.5	1.4	23	8	3	4
100 HDI H67	PDMS-PEG(1100)	0.5	-	65	0.5	1.3	23	8	3	4
		1	-	64	0.5	1.3	22	8	3	4
		4	-	62	0.5	1.3	22	7	3	4
		7	-	61	0.5	1.2	21	7	3	4
100 TMHDI H60	PDMS-PEG(1100)	6	66	0	0.3	0.7	17	8	2	1

5.2.8 SEM

Cell structure was determined by cutting thin slices of the bulk foam in the axial and transverse direction. Samples were acquired from the top, middle, and bottom sections of each foam. The samples were mounted onto a stage and sputter coated with gold for 60 seconds at 20 mA using a Cressington sputter coater (Ted Pella, Inc., Redding, CA). The samples were then visualized using a Joel NeoScope JCM-5000 scanning electron microscope (Nikon Instruments, Inc., Melville, NY) at 15x magnification under high vacuum and 5-10 kV.

5.2.9 Strut thickness

Strut thickness was measured by cutting thin slices of bulk foams in the axial direction and imaging the samples in the brightfield mode using a Leica MZ8 microscope (Leica Microsystems, Wetzlar, Germany) with RSImage software (Photometrics, Tucson, AZ). Foam images were analyzed using ImageJ software (NIH, Bethesda, MD) where strut thickness was measured in microns for each foam composition.

5.2.10 Thermal transition

The glass transition temperature (T_g) of the foams (n = 5) was determined under dry and wet conditions. For dry T_g, foam samples (3-8 mg) were stored in a dry container with desiccant prior to analysis. A Q-200 differential scanning calorimeter (DSC) (TA Instruments, Inc., New Castle, DE) was used to obtain foam thermograms. The first cycle consisted of decreasing the temperature to -40°C at 10°C·min^{-1} and holding it isothermally for 2 minutes. The temperature was then increased to 120°C at

10°C·min^{-1} and held isothermally for 2 minutes. In the second cycle, the temperature was reduced to -40°C at 10°C·min^{-1}, held isothermally for 2 minutes, and raised to 120°C at 10°C·min^{-1}. T_g was recorded from the second cycle based on the inflection point of the thermal transition curve using TA Instruments software (TA Instruments, Inc., New Castle, DE). The aluminum tin was not vented during this step. For wet T_g, foam samples (3-8 mg) were submerged in RO water at 50°C for 5 minutes to allow full plasticization. After the samples were removed from water, they were pressed dry with Kimwipes (Kimberly-Clark Professionals, Roswell, GA), weighed, and placed in an aluminum pan sealed with a vented aluminum lid. A Q-200 DSC was used to cool the samples to -40°C, hold them isothermally for 2 minutes, and heat them to 80°C at 10°C·min^{-1}. TA Instruments software (TA Instruments, Inc., New Castle, DE) was used to generate the thermogram and acquire the T_g after water plasticization using the average inflection point of the thermal transition.

5.2.11 Actuation studies

Cylindrical foam samples (n = 3) with a diameter of 4 mm and a height of 1 cm were cut. A 203.20 μm diameter nickel-titanium (Nitinol) wire (NDC, Fremont, CA) was inserted through the center of the sample along its length to serve as a stabilizer. The foam samples were radially compressed to their smallest possible diameter using a ST 150-42 stent crimper (Machine Solutions, Flagstaff, AZ) by heating the material to 100°C, holding it isothermally for 15 minutes, and programming the foams to the crimped morphology. Initial foam diameter was measured and recorded for each sample using Image J software. The foams were placed in a water bath at 37°C, and images

were taken at 30 seconds, 1 minute and every minute thereafter until 15 minutes, followed by one image every 5 minutes thereafter until 30 minutes. Foam diameter was measured at each time point using Image J software. The final diameter of the samples was measured and recorded using Image J software. Percent volume recovery was calculated using Equation 5.1, and volume expansion was calculated using Equation 5.2.

$$\%\, Volume\ Recovery = \left(\frac{Recovered\ diameter}{Original\ diameter}\right)^2 * 100 \quad \text{(Eq. 5.1)}$$

$$Volume\ Expansion = \left(\frac{Recovered\ diameter}{Compressed\ diameter}\right)^2 \quad \text{(Eq. 5.2)}$$

5.3 Results and discussion

5.3.1 Siloxane-PEG ether amphiphiles

Four surfactants were successfully synthesized with high yield and appropriate siloxane to PEG coupling, as demonstrated by ^{1}H NMR (**Figure 5.2**). The siloxane groups for TS and PDMS appeared around 0.1 PPM, as shown in Figure 5.2a and 5.2b. The allyl hydrogens for PEG appeared at 0.3 and 1.6 PPM, Figure 5.2a and 5.2b. The presence of Si—CH_2 peaks indicated successful coupling of siloxane units to PEG.

FTIR analysis, **Figure 5.3**, provided further characterization of the amphiphile functionality. The presence of Si—CH_3 groups was indicated by strong, sharp peaks at approximately 1260 cm^{-1}. [138] Dimethyl units on the siloxanes usually appear as bands around 800 cm^{-1}; however, copolymers containing alternating or random dimethyl units have shifted bands at 841 cm^{-1} with stronger absorbance. [138] The shifting and increased intensity of dimethyl bands can be seen for amphiphiles containing PDMS. The ether

functionality (C—O) from PEG appears around 1111 cm^{-1} while additional methyl (C—H) peaks occur at 2877 cm^{-1} (PEG) and 2957 cm^{-1} (siloxanes).

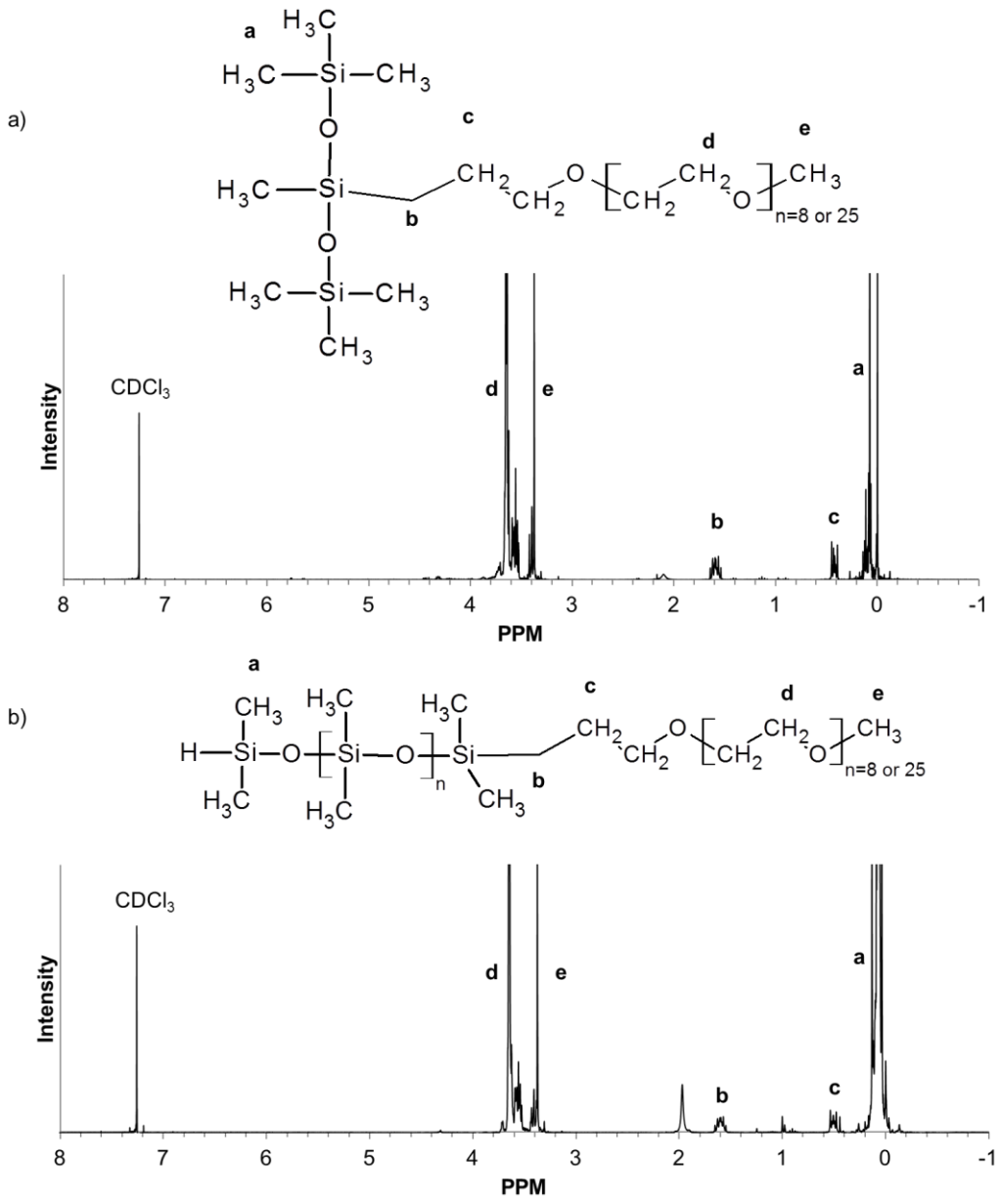

Figure 5.2: ^{1}H NMR spectra of the siloxane-PEG surfactants. a) TS-PEG (n = 8 or 25) and b) PDMS-PEG (n = 8 or 25).

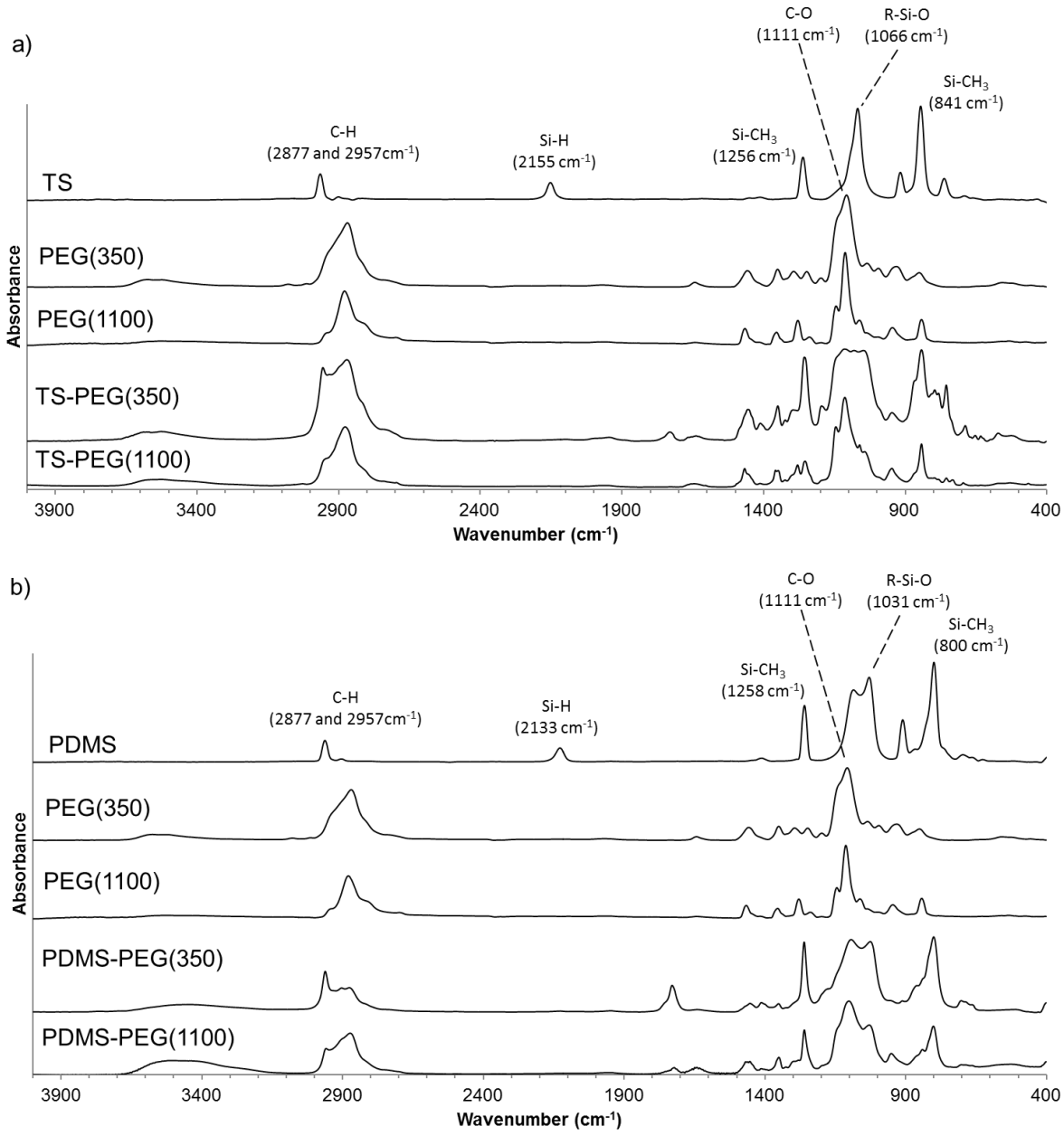

Figure 5.3: Transmission FTIR spectra of the four siloxane-PEG surfactants. a) TS-based and b) PDMS-based surfactants with key peaks highlighting siloxane and PEG coupling.

Figure 5.3a shows successful coupling of TS to PEG due to the Si-H peak removal at 2155 cm^{-1} for TS-PEG(350) and TS-PEG(1100) along with presence of C—O and R—Si—O peaks at 1111 and 1031 cm^{-1}, respectively. PDMS-based surfactants demonstrate similar peak shifts that indicate coupling, Figure 5.3b.

Characterization of the rheological changes for each amphiphile is shown in **Table 5.2**. Molecular weight played a major role in changing the surfactant viscosity. Lower molecular weight amiphiphiles, TS-PEG(350) and PDMS-PEG(350), had lower viscosities of 9.60 ± 0.02 mPa·s and 66.27 ± 0.03 mPa·s, respectively. The sharp increase in viscosity for PDMS-PEG(350) compared to its trisiloxane counterpart is attributed to the high molecular weight of (~580 Da) of PDMS relative to that of trisiloxane (222 Da). Furthermore, TS-PEG(1100) and PDMS-PEG(1100) have higher viscosities of 75.69 ± 0.10 mPa·s and 169.00 ± 0.12 mPa·s, respectively. The long chain lengths of PEG(1100) and PDMS contributed to the higher viscosities compared to lower molecular weight counterparts.

Table 5. 2: Rheological and surface tension properties of the various siloxane-PEG surfactants.

Surfactant	Viscosity (mPa·s)	Surface Tension (mN/m)
TS-PEG(350)	9.6 ± 0.1	21.0 ± 0.1
TS-PEG(1100)	75.7 ± 0.1	20.1 ± 0.3
PDMS-PEG(350)	66.3 ± 0.1	21.3 ± 0.1
PDMS-PEG(1100)	169.0 ± 0.1	20.3 ± 0.1

Surfactant surface tensions were comparable to that of commercially-available surfactants utilized in polyurethane foam synthesis, with values ranging between 20-21 mN/m, Table 5.2. These surface tension values are indicative of the ability of these surfactants to generate a surface tension gradient and thereby serve as cell stabilizers for polyurethane foam blowing.

Mass spectrometry (**Figure 5.4**) provided an additional measure to evaluate amphiphile generation from siloxane-PEG coupling. Figure 5.4a shows the typical mass-to-charge (m/z) peaks for the polyether units that are prevalent in PEG. Hydrosilyation of trisiloxane to PEG resulted in a shift in the m/z peaks to higher weights of 626 Da compared to the original weight of 417 Da for PEG(350). Similarly, trisiloxane coupling generated an increased molecular weight of TS-PEG(1100) (1286 Da) compared to that of PEG(1100) (1080 Da), Figure 5.4b. Trisiloxane is a low molecular weight monomer which ionized while coupled to PEG, resulting in peak shifts to higher molecular weights. In contrast, PDMS-coupled surfactants did not demonstrate molecular weight shifts due to the high molecular weight of PDMS which ionized separately from the PEG constituents. However, peaks for PEG still appear for PDMS-based surfactants (Figure 5.4c and 5.4d), indicating successful coupling of the two surfactant components.

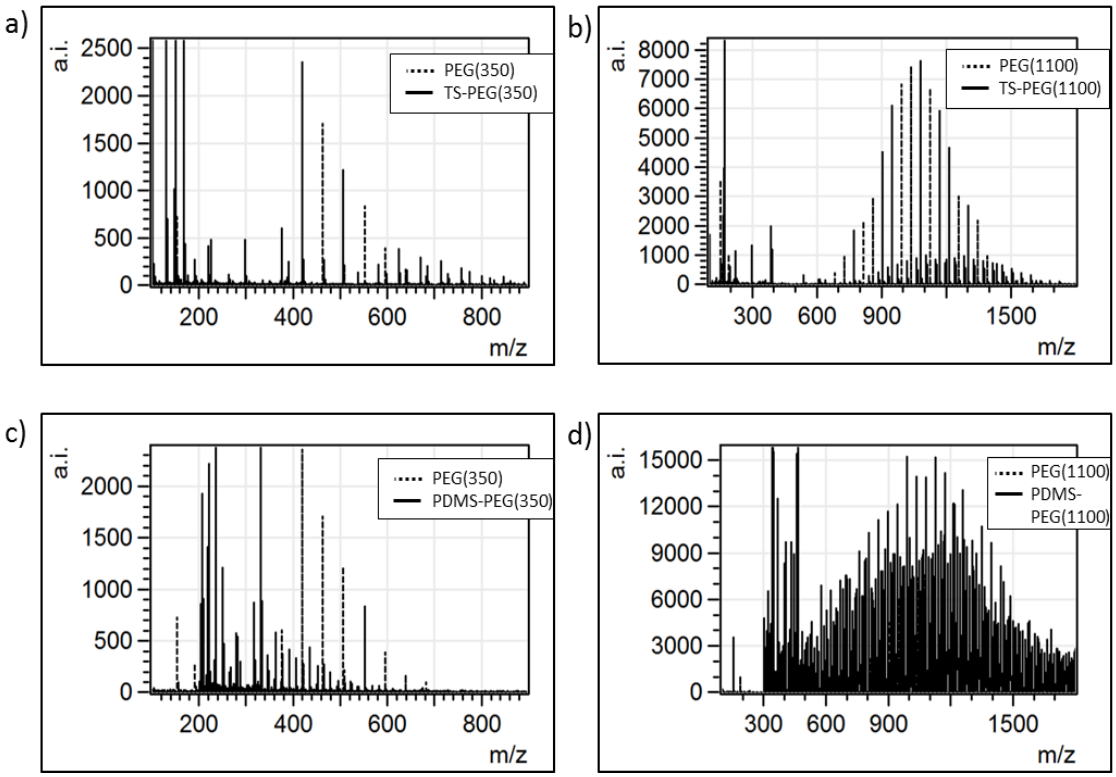

Figure 5.4: MALDI spectra of the surfactants showing shifts in molecular weights due to siloxane-PEG coupling. a) TS-PEG(350), b) TS-PEG(1100), c) PDMS-PEG(350), and d) PDMS-PEG(1100).

5.3.2 Synthesis of SMP foams

SMP foams were synthesized using each of the four surfactants, and their physical properties were characterized, as shown in **Table 5.3**. Stable foam formulations with consistent densities of approximately 0.02-0.03 $g \cdot cm^{-3}$ were obtained for all surfactant types at varied concentrations. The SMP foams had minimal variation in density, which indicates the crucial role of cell stabilizers in developing homogenous, ultra-low density porous systems. It should be noted that higher concentrations (> 0.5%) of PDMS-PEG(350) resulted in bubble coalescence and foam collapse. It can be

hypothesized that above 0.5% concentration, PDMS-PEG(350) reached the critical micelle concentration (CMC). Above the CMC, surfactant/polymer interactions are disrupted, and surfactant molecules interact with each other, causing micelle formation that prevents the surfactants from providing phase stability. Alternatively, incomplete functionalization of the PDMS-based surfactants could result in irregular pore sizes due to varying polymer interfacial surface tension. Further work characterizing potential side products must be conducted on the PDMS-PEG surfactants to determine purity.

Table 5. 3: Key physical properties of SMP foams synthesized using siloxane-PEG surfactants.

Surfactant Type	Foam Composition	Surfactant (wt %)	Density ($g \cdot cm^{-3}$)	Dry T_g (°C)	Wet T_g (°C)	Volume Recovery (%)	Volume Expansion (x)
TS-PEG(350)	100 HDI H67	0.5 4 7	0.017 ± 0.001 0.024 ± 0.002 0.028 ± 0.004	52 ± 2	16 ± 2	103 ± 11	23 ± 3
TS-PEG(1100)	100 HDI H67	0.5 4 7	0.019 ± 0.001 0.028 ± 0.002 0.026 ± 0.004	51 ± 2	16 ± 2	100 ± 18	22 ± 4
PDMS-PEG(350)	100 HDI H67	0.1 0.25 0.5	0.018 ± 0.009 0.025 ± 0.002 0.019 ± 0.001	53 ± 3	17 ± 2	77 ± 5	21 ± 6
PDMS-PEG(1100)	100 HDI H67	0.5 4 7	0.022 ± 0.003 0.016 ± 0.001 0.017 ± 0.001	48 ± 1	17 ± 1	93 ± 14	32 ± 10
	100 TMHDI H60	6	0.024 ± 0.002	57 ± 1	32 ± 1	110 ± 1	17 ± 4

Physical properties of the SMP foams fabricated with the four siloxane-based surfactants had minimal variation as a function of surfactant type, Table 5.3. 100% HDI

foams had a dry and wet T_g of approximately 52°C and 17°C, respectively, for all surfactant types. Lack of variation in T_g indicates that the surfactants serve only as cell stabilizers without added plasticization of the polymer. The transition temperature of 100% HDI SMP foams synthesized using commercial surfactants, DC 4000 and DC 5169, was reported by Singhal et al. to be 55°C under dry conditions for H60 compositions. [19] The 100 TMHDI foams, synthesized using siloxane-PEG surfactants maintain a transition temperature value of 57 ± 1°C, which is close to the T_g reported in literature (58 ± 1°C for 100 TM formulations). [47] The siloxane-PEG surfactants generated in this study had a minimal effect on thermal properties of SMP foams and provided materials that may be competitive with commercially available products.

Qualitatively, SEM micrographs of the various SMP foams show changes in pore uniformity with different surfactant types, **Figure 5.5**. TS-PEG(350) and TS-PEG(1100) yield foams with uniform pores and some open pores. PDMS-PEG(350) yields foams with non-homogenous pores with both large and small bubbles. The pore irregularity further suggests the role of CMC in foam morphology as small bubbles coalesce to foam larger, irregular pores.

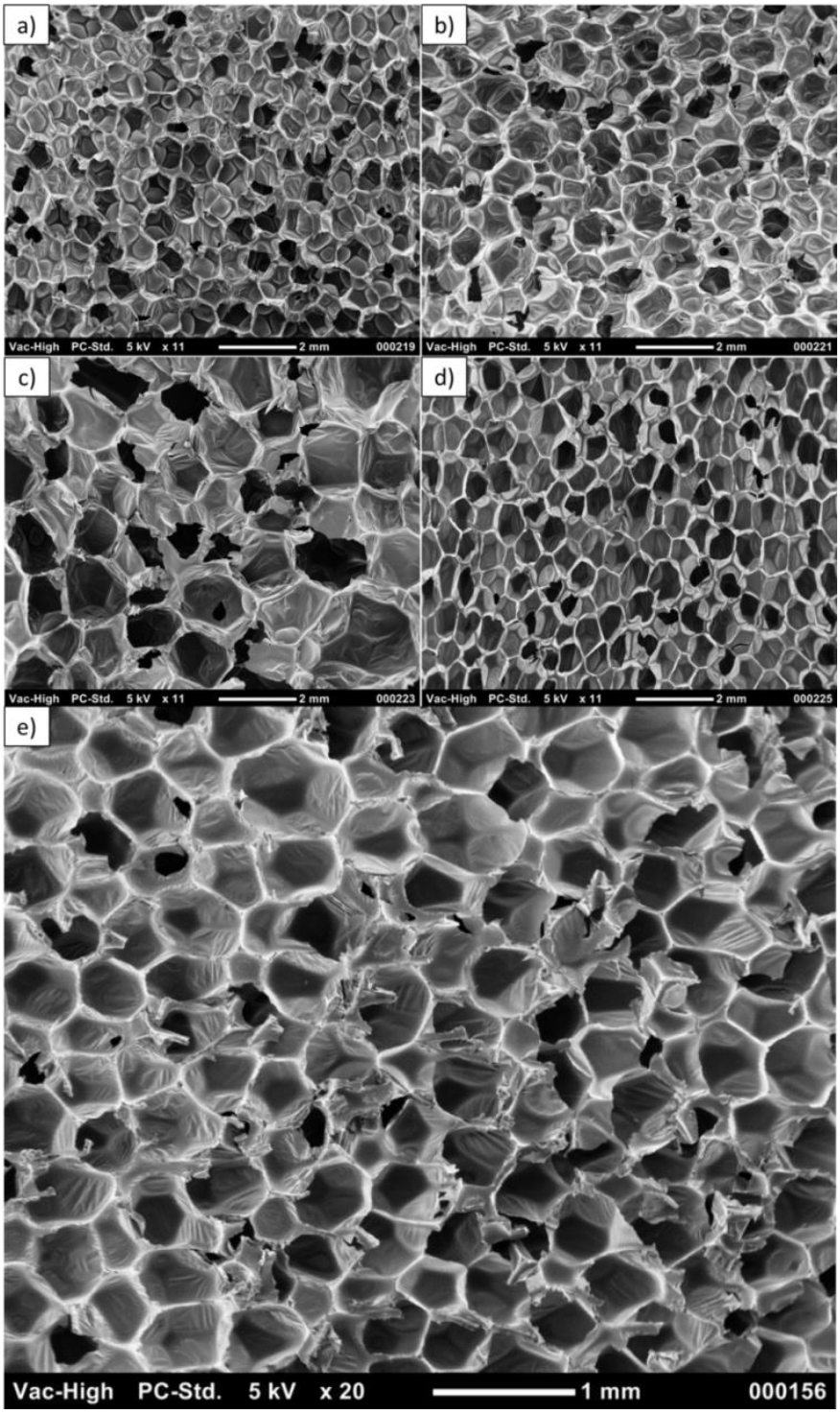

Figure 5.5: SEM images of SMP foams with varying pore sizes based on surfactant type. a) 100 HDI TS-PEG(350), b) 100 HDI TS-PEG(1100), c) 100 HDI PDMS-PEG(350), d) 100 HDI PDMS-PEG(1100), and e) 100 TM PDMS-PEG(1100).

PDMS-PEG(1100) also yielded uniform pores with mostly closed cells. Surfactants that resulted in smaller pores provided more consistent bulk foams. Smaller pores are potentially a result of improved cell stability during foam blowing, as the surfactant stabilizes the small pores upon generation and prevents them from coalescing into larger pores. Due to the desirable foam morphology of PDMS-PEG(1100)-based foams, alternative polymer compositions, containing 100% TMHDI, were pursued to test surfactant viability for different systems. Ultra-low densities are maintained with the TMHDI foam compositions, and SEM images demonstrate uniform pores (Table 5.3, Figure 5.5e). These results indicate the suitability of PDMS-PEG(1100) as a surfactant for various polyurethane systems. Foam pore sizes were also affected by surfactant type and concentration, **Figure 5.6**. At low trisiloxane-based surfactant concentrations (0.5-1%), the foam pore sizes are larger (> 3000 μm) compared to higher concentrations of 4% and 7%, where the pore sizes decrease to approximately 2000 μm, Figure 5.6a and 5.6b. Alternatively, for PDMS-based surfactants, the pore sizes remain fairly consistent around 1500-2000 μm with no discernable trend, Figure 5.6c and 5.6d.

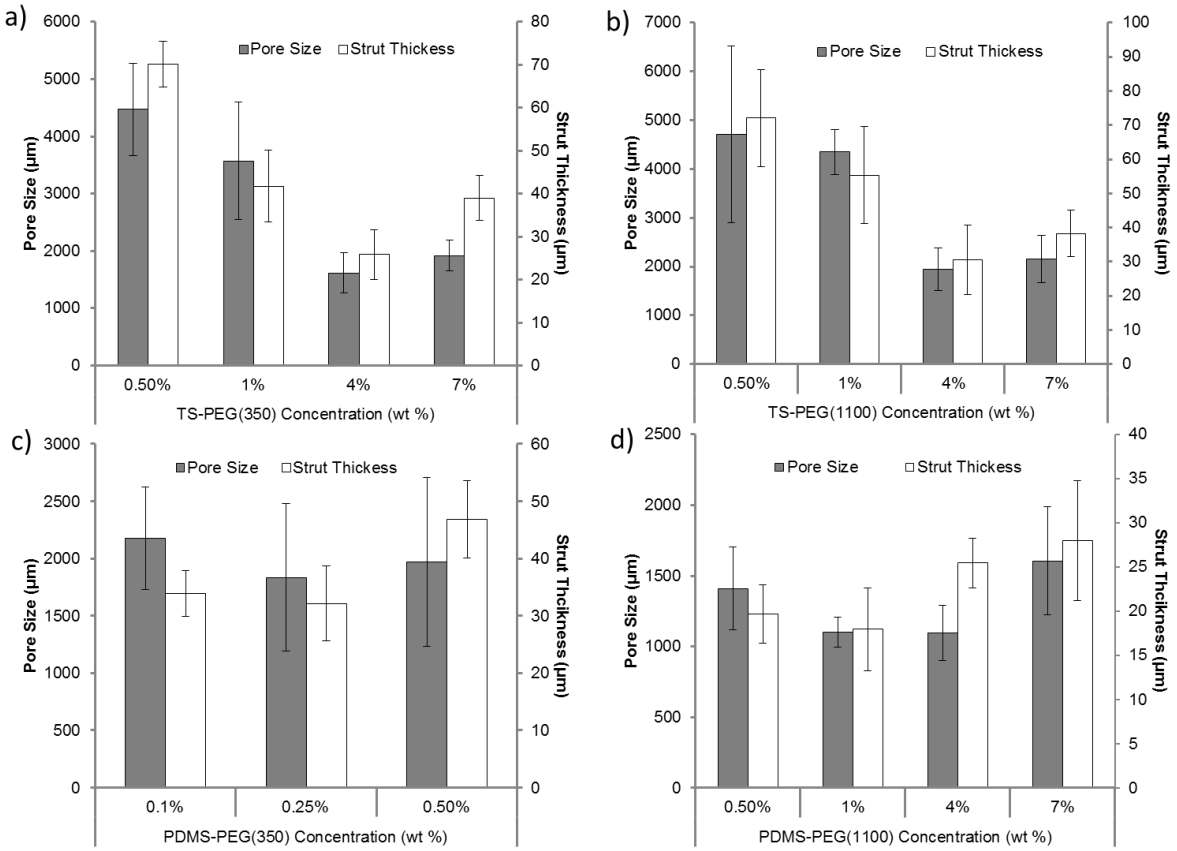

Figure 5.6: Pore size and strut thickness of SMP foams fabricated using the siloxane-PEG surfactants. a) TS-PEG(350), b) TS-PEG(1100), c) PDMS-PEG(350), and d) PDMS-PEG(1100).

Strut thickness of the porous SMP systems was also dependent on the surfactant type and concentration. Lower concentrations of trisiloxane-based surfactants resulted in thicker pore struts due to the lack of polymer spreading at the air-liquid interface. As surfactant concentration increased, the struts became thinner due to polymer mixture stabilization during bubble growth. Quantitative results in Figure 5.6a demonstrate changes in strut thickness, and visual assessment of strut thickness is shown in the microscopic images in **Figure 5.7**. Namely, low surfactant concentrations (0.5% and

1%) (Figure 5.6a) of TS-PEG(350) yielded foams with strut diameters of 70 μm ± 5 and 42 μm ± 8, respectively. At higher concentrations of 4% and 7%, the strut thicknesses were reduced to approximately 30 μm (Figure 5.6a). Similar trends were noted with TS-PEG(1100) foams. At 0.5% PDMS-PEG(350), the strut thickness slightly increased due to cell destabilization, however no definite trend could be established. (Figure 5.6c and 5.7c). As shown in Figures 5.6d and 5.7d, minimal changes in strut diameter were observed with increasing concentration for PDMS-PEG(1100), where struts were approximately 22 μm over the range of surfactant concentrations. There was no trend in strut thickness for SMP foams synthesized using PDMS-based surfactants. However, controlling the strut thickness could potentially provide an alternative route to tuning the mechanical properties of the scaffolds, as thicker struts are hypothesized to result in mechanically robust systems.

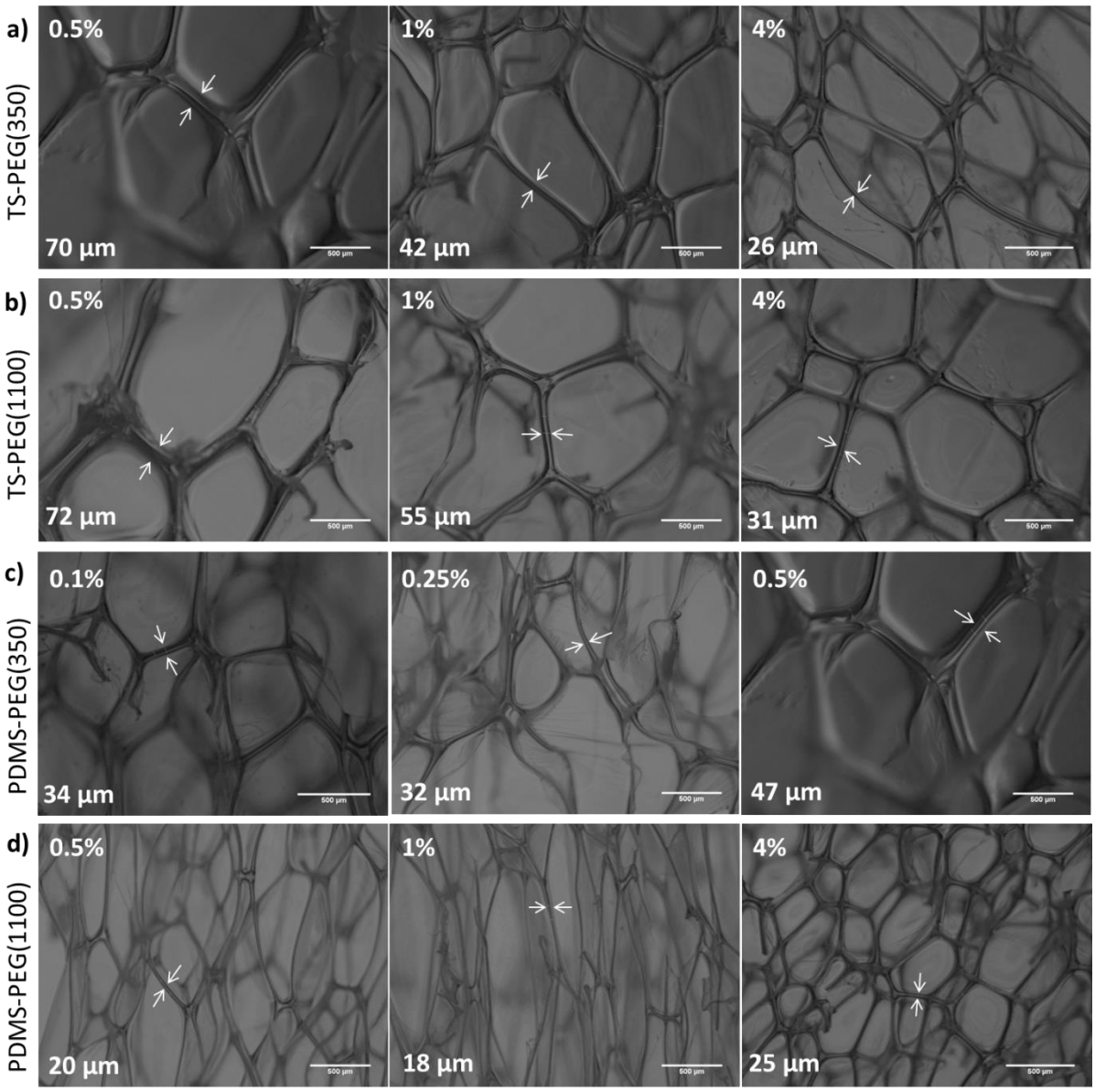

Figure 5.7: Micrographs of SMP foams with varying strut thickness based on surfactant type and concentration. a) TS-PEG(350), b) TS-PEG(1100), c) PDMS-PEG(350), and d) PDMS-PEG(1100).

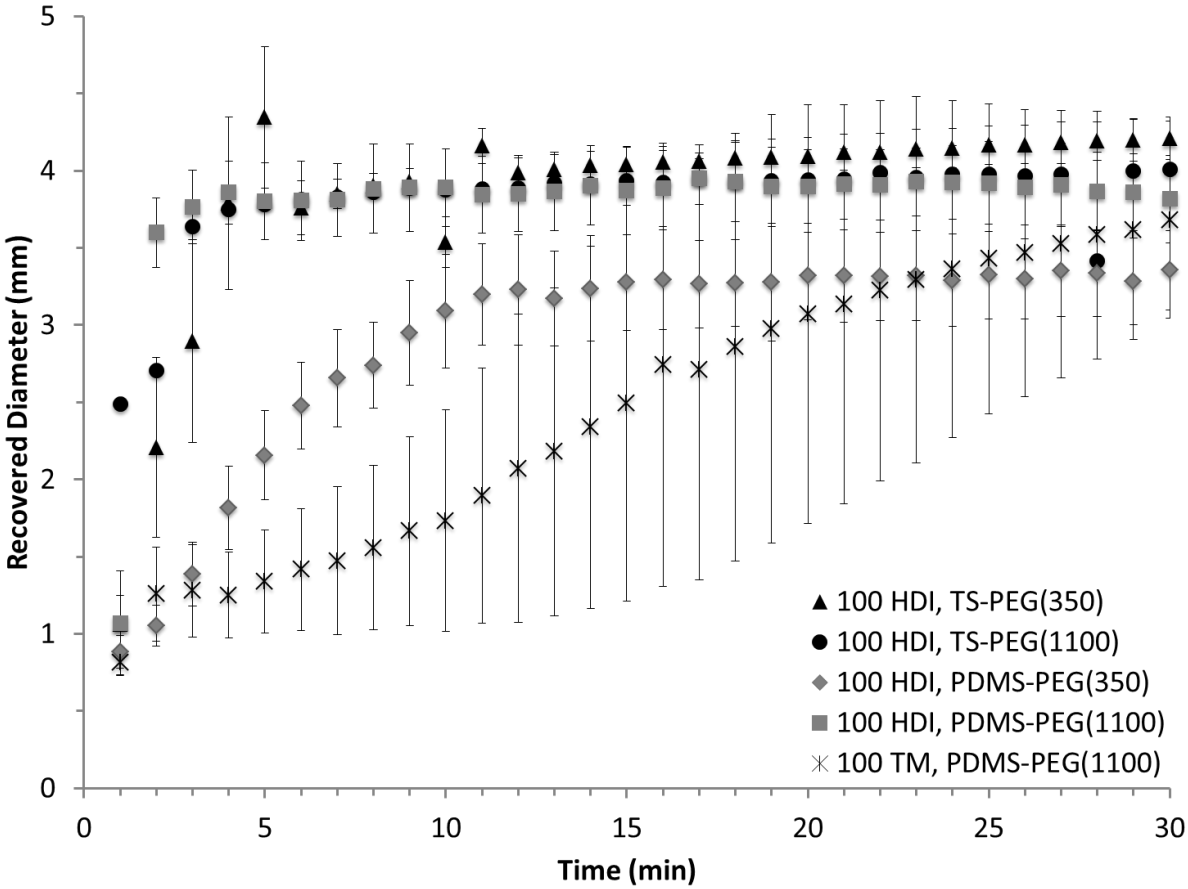

Figure 5.8: Actuation profiles of SMP foams synthesized with siloxane-PEG surfactants.

Further characterization of the actuation profiles of the SMP foams showed the foams synthesized using trisiloxane-based surfactants actuated fully within the first 3 minutes of exposure to physiological temperatures in an aqueous environment, **Figure 5.8**. The volume recovery of these foam compositions was 100%, which is indicative of their rapid shape memory behavior, Table 5.3.2. Due to the hydrophilic nature of HDI, the rapid actuation and high volume recovery is an expected outcome. However, PDMS-PEG(350) SMP foams experienced slower recovery, with full actuation achieved after

10 minutes. Additionally, the volume recovery of the PDMS-PEG(350) foams was lower compared to other compositions, at only 77%. The irregular pore morphology of the SMP foams synthesized using PDMS-PEG(350) could have a potential effect on reducing the shape memory behavior of the system. However, the total volume expansion (21x) of these foams was similar to trisiloxane-based formulations. 100 HDI, PDMS-PEG(1100) foams also experienced rapid actuation, with volume recovery similar to that of trisiloxane-based foam formulation. 100 TMHDI foam compositions had the slowest actuation, with full recovery achieved after 20 minutes. The presence of methyl groups on TMHDI increased hydrophobicity of the system, hence slower water plasticization and recovery profiles were observed. However, the volume recovery of this system was 110%, suggesting preservation of the shape memory behavior of the material. Controlling shape recovery of the SMP foams is important for modifying material properties, depending on the application. For example, fast volumetric recovery is desirable for wound hemostatic treatments while slow actuation would be optimal for aneurysm occlusion devices that require delivery though a micro-catheter.

5.4 Conclusions

Siloxane-PEG surfactants were successfully synthesized using hydrosilylation with high yield to serve as cell stabilizers during shape memory polyurethane foam synthesis. The surfactants had low surface tension, similar to commercially-available products. Siloxane-PEG surfactants successfully stabilized the foam cells during the synthesis of porous SMPs. By lowering the surface tension within the struts, the surfactants allowed liquid polymer spreading at the interface. In addition to pore

stability, the surfactants played a key role in tuning the pore size and morphology of the SMP foams. Furthermore, strut thickness of the foams was heavily dependent on surfactant type and concentration. Controlling the strut thickness also provides a means to control foam morphology and mechanical properties for a variety of applications. Overall, surfactant properties and performance were similar to those of commercially available cell stabilizers, indicating their potential for use in quality-controlled SMP foam synthesis.

CHAPTER VI

CONCLUSIONS

6.1 Summary

In this work, porous SMP scaffolds were developed to serve as implantable materials for neurovascular occlusion. The foam-over-wire device would be an improvement compared to bare metal coils due to their high volumetric filling and large surface area. Additionally, the SMP foams have reportedly improved healing outcomes with good thrombus resolution compared to the industry standard. However, control over the actuation profiles and thermo-mechanical response of the SMP foams in necessary for device development since the working time for the clinician must include full device delivery and proper placement prior to foam actuation. Chemical modifications to the bulk material, using IPDI, slowed the rate of water plasticization of the urethane/urea bonds and increased hydrophobicity of the polymer system. The added stiffness from the ring moiety of IPDI also increased foam T_g thereby delaying the onset of actuation and providing tunable foam recovery.

Radiopacity of the aneurysm occlusion device was enhanced by developing SMP nanocomposites using tugsten nanoparticles. High nanoparticle loading resulted in x-ray visibility of the SMP foams through soft and hard tissue in a porcine model. In addition to imparting radiopacity to the polymer, incorporation of tungsten nanoparticles provided further control over the foam morphology and thermal properties. The transition temperature of the system increased by 10°C with a similar effect on actuation time where the onset of foam expansion increased up to 8 minutes. High filler loading

also tuned the mechanical properties of the polymer system. Increased net points in the system resulted in increased material stiffness and decreased toughness and strain at break. While lower toughness is not desirable for medical implants, the x-ray visibility of the device is valuable for device delivery and positioning.

Using different nanoparticles to improve mechanical properties was detailed in Chapter IV. Al_2O_3, SiO_2 and W nanoparticles were incorporated into the SMP foams at low concentrations to improve material toughness and resistance to tear and particulate generation. The resulting SMP nanocomposites had controllable thermo-mechanical properties with tunable actuation profiles and improved thermal stability. Additionally, the nanocomposites had minimal particulate generation and filler leaching out of the polymer matrix.

Lastly, foam morphology and pore sizes were modified by using siloxane-PEG surfactants are cell stabilizers during the gas blowing process. Siloxane-PEG surfactants were synthesized *via* hydrosilylation with surface activity similar to commercially-available products. The surfactants provided a greater degree of control over the SMP foam pore morphology, strut thickness, and cell size. However, the surfactants had a minimal effect on the shape memory behavior of the SMP systems, indicating their use as viable cell stabilizers that do not modify the thermo-mechanical response of the material.

6.2 Significance of work

SMP foams have a potential for use has implantable biomaterials due to their good biocompatibility and healing response. As aneurysm occlusion agents, these foams

result in a rapid, stable occlusion and provide complete volumetric filling due to their shape memory behavior. The actuation time of the foams, however, requires tailoring to fit clinician need for a device working time of 10 minutes or greater. In Chapter II, the actuation time of the foams was modified to 30 minutes and greater, indicating the suitability of these SMP systems for various applications that may require tunable shape recovery. For aneurysm occlusion, a longer working time is desirable as the clinician must deploy the FOW device through a tortuous pathway and the final positioning of the device may require additional time. To prevent premature foam actuation in the catheter during the procedure, the material properties must be designed to specifically fulfil the clinician need. Additionally, the hydrophobicity of the polymer was controllable through IPDI incorporating. These changeable properties may potentially expand the use of our SMP systems as drug delivery carriers and chemotherapy-induced thrombotic agents.

In Chapter III, radiopacity of the foams containing tungsten nanoparticles were evaluated for x-ray visible devices. During a minimally-invasive endovascular coiling procedure, the clinician must rely on x-ray fluoroscopy for guiding and positioning the devices to the aneurysm. Lack of radiopacity is a significant obstacle for FOW devices since feasibility of delivery and similarity to preceding devices is an important factor for clinicians to utilize new products. Furthermore, x-ray visualization through the skull is difficult due to the presence of dense bone and soft tissue. Therefore, high concentrations of radiopaque agents are necessary for visualizing small geometry materials. The tungsten-loaded SMP foams also provide a means of evaluating actuation *in vivo*. When crimped, the foams are visible through fluoroscopy. However, upon

actuation the foams expand and lose the density requirements for radiopacity. The change in opacity would provide another metric of confirmation to the clinician regarding device actuation and clot formation.

In Chapter IV, the mechanical properties of the SMP foams were improved by reinforcing them with various nanoparticles. Mechanically robust materials are less susceptible to tear and fracture which is desirable for the SMP foams used in this work. Due to the low density of the foams, there is a high potential for particulate generation, from strut breakage, which can cause emboli in other parts of the body. However, reinforcing the foams with nanoparticles provided improved toughness which further minimized particulate generation. Additionally, the use of nanofillers in SMP foams modified their recovery profiles and thermal stability.

Finally, in Chapter V, siloxane-PEG surfactants were developed as cell stabilizers for SMP foams. Changing the length of the PEG units enabled control over surfactant properties such as surface activity and viscosity. Each surfactant had low surface tension (~20 mN/m), comparable to commercially-available products, making them suitable cell stabilizers for polyurethane foams. The siloxane-PEG surfactants provided control over the SMP foam cell morphology, cell size, and strut thickness. These properties are important to tune for ultra-low density systems to maintain high volume recovery and good mechanical properties. Uniform pores were achieved through all surfactant types with varying cell sizes. This degree of control over foam morphology allows for their use in multiple applications that require tunable scaffold porosity and size.

6.3 Challenges and future directions

The SMP foams designed in this work have significant advantages as implantable biomaterials compared to previous generation materials. While improvements in material properties and actuation response have been made in this work, further modification is required to ensure their use in medical devices. The FOW device requires SMP scaffolds with small pores (~400 μm) to allow for delivery through microcatheter. However, the SMP nanocomposites, developed in Chapter IV, do not have small pores suitable for device development. Further work is required to modify the fabrication protocol in order to generate SMPs with smaller pores. For example, pore sizes can be controlled by changing the viscosity of the NCO premix during foam synthesis. NCO premix viscosity can be modified by changing the OH content present in solution. Higher OH content would increase crosslink density and therefore increase viscosity. A highly viscous NCO premix would result in small pores in the SMP foam. Additional variables including mixing time, catalyst concentration, and surfactant concentration provide further control over cell size.

Similarly, surfactant structure can be altered to tune foam morphology. The surfactants synthesized in Chapter V contain long chain PEG units. Effects of short chain polyethylene oxide units on surfactant properties must be evaluated along with their effectiveness as polyurethane foaming surfactants. Short chain allyl methyl ethers can be synthesized by reacting a good electrophile, such as allyl bromide, with mono-terminated polyethylene oxide units of varying molecular weight in the presence of acid or base. Synthesizing custom hydrophilic constituents will provide a better

understanding of surfactant surface activity and interaction with the polymer phase. Using fluorocarbons as the hydrophobic unit may also tune surfactant properties compared to siloxane groups. Fluorocarbons are well-studied in the literature to have surface tension ranging from 15-20 mN/m. [139] This is desirable for polyurethane foaming because generation of a surface tension gradient prevents strut thinning during foam blowing.

The SMP nanocomposites, designed for FOW in Chapter IV, experienced aggregate generation of the nanoparticles. This further effected foam mechanical properties as greater aggregates generally led to lower toughness and strength. Additionally, higher concentrations of nanoparticles would cause aggregate formation in the SMP struts. To overcome this limitation, future works should focus on developing surface modified nanoparticles that can be covalently coupled to the SMP matrix during foam synthesis. Covalent binding of nanoparticles to the polymer would yield better reinforcement of the system which would provide a superior mechanical response. Additionally, permanent nanoparticle coupling would prevent filler leaching from the SMP system and potentially allow for higher filler loadings for other applications such as x-ray visibility and drug delivery. The nanoparticles could be surface modified by utilizing silane coupling agents. Silane coupling agents have been well-researched to form durable bonds between inorganic and organic materials. [140, 141] The non-hydrolyzable R group on a typical silane coupling agent ($R\text{-}(CH_2)_n\text{-}Si\text{-}X_3$) unit may be a hydroxyl or amine group which can react with the NCO groups of the SMP system. [141] Nanoparticles such as Al_2O_3 and SiO_2 may be modified using this approach to add

covalent linkers for binding to the SMP. This method would improve nanoparticle dispersion into the polymer matrix and further enhance mechanical properties due to the increased crosslink density.

Previously-designed SMP foams, similar to the ones described in this work, have known biocompatibility and desirable tissue response. However, the biocompatibility of the new SMP foams needs to be further evaluated. Direct and indirect i*n vitro* cell adhesion and proliferation studies must be conducted on all SMP foams fabricated in this work to determine their viability as implantable materials. Leachables, such as surfactants and nanoparticles, may be cytotoxic; hence their effect on cell viability should be further studied to safety of the resulting medical devices.

Lastly, scale up of SMP foams and surfactants is necessary for reproducible device manufacturing. While the current foaming protocol is optimal for small foam batches, additional experiments need to be conducted to generate a detailed protocol for producing bulk materials. Factors such as surfactant concentration, mixing time, and NCO premix viscosity would require tuning for large foam batches to prevent premature foam actuation while maintaining the small cell morphology. Additionally, the siloxane-PEG surfactants would need to be synthesized in bulk for their use in foam manufacturing. Complete solvent and catalyst removal may pose as a potential difficulty for surfactant scale up. As a solution, rigorous extraction and low-pressure evaporation steps must be taken to provide an impurity-free product.

REFERENCES

1. Hearon, K.; Singhal, P.; Horn, J.; Small, W.t.; Olsovsky, C.; Maitland, K.C.; Wilson, T.S.; Maitland, D.J. Porous shape memory polymers. *Polym Rev (Phila Pa)* **2013**, *53*, 41-75.

2. Sun, L.; Huang, W.M.; Ding, Z.; Zhao, Y.; Wang, C.C.; Purnawali, H.; Tang, C. Stimulus-responsive shape memory materials: A review. *Materials & Design* **2012**, *33*, 577-640.

3. Xie, T. Recent advances in polymer shape memory. *Polymer* **2011**, *52*, 4985-5000.

4. Meng, Q.; Hu, J. A review of shape memory polymer composites and blends. *Composites Part A: Applied Science and Manufacturing* **2009**, *40*, 1661-1672.

5. Wilson, T.S.; Bearinger, J.P.; Herberg, J.L.; Marion, J.E.; Wright, W.J.; Evans, C.L.; Maitland, D.J. Shape memory polymers based on uniform aliphatic urethane networks. *Journal of Applied Polymer Science* **2007**, *106*, 540-551.

6. Small, W.t.; Singhal, P.; Wilson, T.S.; Maitland, D.J. Biomedical applications of thermally activated shape memory polymers. *J Mater Chem* **2010**, *20*, 3356-3366.

7. Leng, J.; Lan, X.; Liu, Y.; Du, S. Shape-memory polymers and their composites: Stimulus methods and applications. *Progress in Materials Science* **2011**, *56*, 1077-1135.

8. Song, J.J.; Chang, H.H.; Naguib, H.E. Design and characterization of biocompatible shape memory polymer (smp) blend foams with a dynamic porous structure. *Polymer* **2015**, *56*, 82-92.

9. Zhao, Q.; Qi, H.J.; Xie, T. Recent progress in shape memory polymer: New behavior, enabling materials, and mechanistic understanding. *Progress in Polymer Science*.

10. Hu, J.; Zhu, Y.; Huang, H.; Lu, J. Recent advances in shape–memory polymers: Structure, mechanism, functionality, modeling and applications. *Progress in Polymer Science* **2012**, *37*, 1720-1763.

11. Hager, M.D.; Bode, S.; Weber, C.; Schubert, U.S. Shape memory polymers: Past, present and future developments. *Progress in Polymer Science*.

12. Meng, H.; Li, G. A review of stimuli-responsive shape memory polymer composites. *Polymer* **2013**, *54*, 2199-2221.

13. Janik, H.; Marzec, M. A review: Fabrication of porous polyurethane scaffolds. *Mater Sci Eng C Mater Biol Appl* **2015**, *48*, 586-591.

14. Hentze, H.P.; Antonietti, M. Porous polymers and resins for biotechnological and biomedical applications. *Reviews in Molecular Biotechnology* **2002**, *90*, 27-53.

15. Ji, C.; Annabi, N.; Hosseinkhani, M.; Sivaloganathan, S.; Dehghani, F. Fabrication of poly-dl-lactide/polyethylene glycol scaffolds using the gas foaming technique. *Acta Biomater* **2012**, *8*, 570-578.

16. Drenckhan, W.; Saint-Jalmes, A. The science of foaming. *Advances in Colloid and Interface Science*.

17. Jensen, J.K.; Jensen, L.O.; Terkelsen, C.J.; Lassen, J.F.; Tilsted, H.H.; Hansen, K.N.; Maeng, M.; Thuesen, L.; Thayssen, P. Incidence of definite stent thrombosis or in-stent restenosis after drug-eluting stent implantation for treatment of coronary in-stent restenosis: From western denmark heart registry. *Catheterization and Cardiovascular Interventions* **2013**, *81*, 260-265.

18. Frerich, S.C. Biopolymer foaming with supercritical co2—thermodynamics, foaming behaviour and mechanical characteristics. *The Journal of Supercritical Fluids* **2015**, *96*, 349-358.

19. Singhal, P.; Rodriguez, J.N.; Small, W.; Eagleston, S.; Van de Water, J.; Maitland, D.J.; Wilson, T.S. Ultra low density and highly crosslinked biocompatible shape memory polyurethane foams. *J Polym Sci B Polym Phys* **2012**, *50*, 724-737.

20. Lee, S.H.; Jang, M.K.; Kim, S.H.; Kim, B.K. Shape memory effects of molded flexible polyurethane foam. *Smart Materials and Structures* **2007**, *16*, 2486.

21. Kang, S.M. Shape memory polyurethane foams. *Express Polymer Letters* **2011**, *6*, 63-69.

22. Salerno, A.; Clerici, U.; Domingo, C. Solid-state foaming of biodegradable polyesters by means of supercritical co2/ethyl lactate mixtures: Towards designing advanced materials by means of sustainable processes. *European Polymer Journal* **2014**, *51*, 1-11.

23. Jacobs, L.J.M.; Kemmere, M.F.; Keurentjes, J.T.F. Sustainable polymer foaming using high pressure carbon dioxide: A review on fundamentals, processes and applications. *Green Chemistry* **2008**, *10*, 731-738.

24. Pasquali, I.; Bettini, R.; Giordano, F. Solid-state chemistry and particle engineering with supercritical fluids in pharmaceutics. *European Journal of Pharmaceutical Sciences* **2006**, *27*, 299-310.

25. Duarte, A.R.C.; Mano, J.F.; Reis, R.L. Supercritical fluids in biomedical and tissue engineering applications: A review. *International Materials Reviews* **2009**, *54*, 214-222.

26. Song, J.J.; Chang, H.H.; Naguib, H.E. Design and characterization of biocompatible shape memory polymer (smp) blend foams with a dynamic porous structure. *Polymer* **2015**, *56*, 82-92.

27. Ortega, J.M.; Hartman, J.; Rodriguez, J.N.; Maitland, D.J. Virtual treatment of basilar aneurysms using shape memory polymer foam. *Ann Biomed Eng* **2013**, *41*, 725-743.

28. Muschenborn, A.D.; Ortega, J.M.; Szafron, J.M.; Szafron, D.J.; Maitland, D.J. Porous media properties of reticulated shape memory polymer foams and mock embolic coils for aneurysm treatment. *Biomed Eng Online* **2013**, *12*, 103.

29. Hasan, S.M.; Raymond, J.E.; Wilson, T.S.; Keller, B.K.; Maitland, D.J. Effects of isophorone diisocyanate on the thermal and mechanical properties of shape-memory polyurethane foams. *Macromolecular Chemistry and Physics* **2014**, *215*, 2420-2429.

30. Singhal, P.; Boyle, A.; Brooks, M.L.; Infanger, S.; Letts, S.D.; Small, W.D.; Maitland, D.J.D.; Wilson, T.S.D. Controlling the actuation rate of low-density shape-memory polymer foams in water. *Macromol Chem Phys* **2013**, *214*, 1204-1214.

31. Metcalfe, A.; Desfaits, A.-C.; Salazkin, I.; Yahia, L.H.; Sokolowski, W.M.; Raymond, J. Cold hibernated elastic memory foams for endovascular interventions. *Biomaterials* **2003**, *24*, 491-497.

32. Rodriguez, J.N.; Clubb, F.J.; Wilson, T.S.; Miller, M.W.; Fossum, T.W.; Hartman, J.; Tuzun, E.; Singhal, P.; Maitland, D.J. In vivo response to an implanted shape memory polyurethane foam in a porcine aneurysm model. *J Biomed Mater Res A* **2014**, *102*, 1231-1242.

33. Singhal, P.; Small, W.; Cosgriff-Hernandez, E.; Maitland, D.J.; Wilson, T.S. Low density biodegradable shape memory polyurethane foams for embolic biomedical applications. *Acta Biomater* **2014**, *10*, 67-76.

34. Rodriguez, J.N.; Miller, M.W.; Boyle, A.; Horn, J.; Yang, C.K.; Wilson, T.S.; Ortega, J.M.; Small, W.; Nash, L.; Skoog, H.; Maitland, D.J. Reticulation of low density shape memory polymer foam with an in vivo demonstration of vascular occlusion. *J Mech Behav Biomed Mater* **2014**, *40*, 102-114.

35. Boyle, A.J.; Landsman, T.L.; Wierzbicki, M.A.; Nash, L.D.; Hwang, W.; Miller, M.W.; Tuzun, E.; Hasan, S.M.; Maitland, D.J. In vitro and in vivo evaluation of a shape memory polymer foam-over-wire embolization device delivered in saccular aneurysm models. *Journal of Biomedical Materials Research Part B: Applied Biomaterials* **2015**, n/a-n/a.

36. Avar, G.; Meier-Westhues, U.; Casselmann, H.; Achten, D. Polyurethanes. **2012**, 411-441.

37. Muschenborn, A.D.; Ortega, J.M.; Szafron, J.M.; Szafron, D.J.; Maitland, D.J. Porous media properties of reticulated shape memory polymer foams and mock embolic coils for aneurysm treatment. *BioMedical Engineering OnLine* **2013**, *12*, 1-13.

38. Rodriguez, J.N.; Yu, Y.J.; Miller, M.W.; Wilson, T.S.; Hartman, J.; Clubb, F.J.; Gentry, B.; Maitland, D.J. Opacification of shape memory polymer foam designed for treatment of intracranial aneurysms. *Ann Biomed Eng* **2012**, *40*, 883-897.

39. Currie, S.; Mankad, K.; Goddard, A. Endovascular treatment of intracranial aneurysms: Review of current practice. *Postgraduate Medical Journal* **2011**, *87*, 41-50.

40. Kim, K.-H.; Cha, K.-C.; Kim, J.-S.; Hong, S.-C. Endovascular coiling of middle cerebral artery aneurysms as an alternative to surgical clipping. *Journal of Clinical Neuroscience* **2013**, *20*, 520–522.

41. Hayakawa, M.; Murayama, Y.; Duckwiler, G.R.; Gobin, Y.P.; Guglielmi, G.; Vinuela, F. Natural history of the neck remnant of a cerebral aneurysm treated with the Guglielmi detachable coil system. *Journal of Neurosurgery* **2000**, *93*, 561-586.

42. Molyneux, A. International subarachnoid aneurysm trial (ISAT) of neurosurgical clipping versus endovascular coiling in 2143 patients with ruptured intracranial aneurysms: A randomised trial. *The Lancet* **2002**, *360*, 1267-1274.

43. Hampikian, J.M.; Heaton, B.C.; Tong, F.C.; Zhang, Z.; Wong, C.P. Mechanical and radiographic properties of a shape memory polymer composite for intracranial aneurysm coils. *Materials Science and Engineering C* **2006**, *26*, 1373-1379.

44. Cloft, H.J. Hydrocoil for endovascular aneurysm occlusion (heal) study: Periprocedural results. *American Journal of Neuroradiology* **2006**, *27*, 289-292.

45. Guo, X.B.; Fan, Y.M.; Zhang, J.N. Hydrosoft coil versus hydrocoil for endovascular aneurysm occlusion study: A single center experience. *Eur J Radiol* **2011**, *79*, e42-46.

46. Hwang, W.; Singhal, P.; Miller, M.W.; Maitland, D.J. In vitro study of transcatheter delivery of a shape memory polymer foam embolic device for treating cerebral aneurysms. *Journal of Medical Devices* **2013**, *7*.

47. Singhal, P.; Boyle, A.; Brooks, M.L.; Infanger, S.; Letts, S.; Small, W.; Maitland, D.J.; Wilson, T.S. Controlling the actuation rate of low-density shape-memory polymer foams in water. *Macromolecular Chemistry and Physics* **2013**, *214*, 1204-1214.

48. James, N.R.; Philip, J.; Jayakrishnan, A. Polyurethanes with radiopaque properties. *Biomaterials* **2006**, *27*, 160-166.

49. Zhang, X.D.; Macosko, C.W.; Davis, H.T.; Nikolov, A.D.; Wasan, D.T. Role of silicone surfactant in flexible polyurethane foam. *J Colloid Interface Sci* **1999**, *215*, 270-279.

50. Hill, R.M. Silicone (siloxane) surfactants. In *Hydrosilylation: A comprehensive review on recent advances*; Matisons, J., Ed. Springer Science+Business Media B.V.: Dordrecht, Netherlands,

51. Hill, R.M. Silicone surfactants□new developments. *Current Opinion in Colloid & Interface Science* **2002**, *7*, 255-261.

52. Maitland, D.J.; Metzger, M.F.; Schumann, D.; Lee, A.; Wilson, T.S. Photothermal properties of shape memory polymer micro-actuators for treating stroke. *Lasers Surg. Med.* **2002**, *30*, 1-11.

53. Cullum, B.M.; Wilson, T.S.; Small Iv, W.; Benett, W.J.; Bearinger, J.P.; Maitland, D.J.; Carter, J.C. Shape memory polymer therapeutic devices for stroke. *Proc. of SPIE* **2005**, *6007*, 60070R-60070R-60078.

54. Small IV, W.; Singhal, P.; Wilson, T.S.; Maitland, D.J. Biomedical applications of thermally activated shape memory polymers. *J. Mater. Chem* **2010**, *20*, 3356-3366.

55. Wilson, T.S.; Bearinger, J.P.; Herberg, J.L.; Marion, J.E.; Wright, W.J.; Evans, C.L.; Maitland, D.J. Shape memory polymers based on uniform aliphatic urethane networks. *J. Appl. Polym. Sci.* **2007**, *106*, 540-551.

56. Singhal, P.; Rodriguez, J.N.; Small, W.; Eagleston, S.; Van de Water, J.; Maitland, D.J.; Wilson, T.S. Ultra low density and highly crosslinked biocompatible shape memory polyurethane foams. *J. Polym. Sci., Part B: Polym. Phys.* **2012**, *50*, 724-737.

57. Singhal, P.; Boyle, A.; Brooks, M.L.; Infanger, S.; Letts, S.; Small, W.; Maitland, D.J.; Wilson, T.S. Controlling the actuation rate of low-density shape-memory polymer foams in water. *Macromol. Chem. Phys.* **2013**, *214*, 1204-1214.

58. Singhal, P.; Small, W.; Cosgriff-Hernandez, E.; Maitland, D.J.; Wilson, T.S. Low density biodegradable shape memory polyurethane foams for embolic biomedical applications. *Acta Biomater.* **2014**, *10*, 67-76.

59. Rodriguez, J.N.; Yu, Y.J.; Miller, M.W.; Wilson, T.S.; Hartman, J.; Clubb, F.J.; Gentry, B.; Maitland, D.J. Opacification of shape memory polymer foam designed for treatment of intracranial aneurysms. *Ann. Biomed. Eng.* **2012**, *40*, 883-897.

60. Leng, J.; Lan, X.; Liu, Y.; Du, S. Shape-memory polymers and their composites: Stimulus methods and applications. *Prog. Mater. Sci.* **2011**, *56*, 1077-1135.

61. Chae Jung, Y.; Hwa So, H.; Whan Cho, J. Water-responsive shape memory polyurethane block copolymer modified with polyhedral oligomeric silsesquioxane. *J. Macromol. Sci., Phys.* **2006**, *45*, 453-461.

62. Hearon, K.; Singhal, P.; Horn, J.; IV, W.S.; Olsovsky, C.; Maitland, K.C.; Wilson, T.S.; Maitland, D.J. Porous shape-memory polymers. *Polym. Rev.* **2013**, *53*, 41-75.

63. Rosler, A.; Vandermeulen, G.W.M.; Klok, H.-A. Advanced drug delivery devices via self-assembly of amphiphilic block copolymers. *Advanced Drug Delivery Reviews* **2001**, *53*, 95-108.

64. Warlow, C.P. Epidemiology of stroke. *The Lancet* **1998**, *352*, S1-S4.

65. Juvela, S.; Poussa, K.; Porras, M. Factors affecting formation and growth of intracranial aneurysms : A long-term follow-up study. *Stroke* **2001**, *32*, 485-491.

66. Sluzewski, M.; Bosch, J.A.; Rooij, W.J.V.; Nijssen, P.C.G.; Wijnalda, D. Rupture of intracranial aneurysms during treatment with Guglielmi detachable coils: Incidence, outcome, and risk factors. *Journal of Neurosurgery* **2001**, *94*, 238-240.

67. Kim, J.H.; Kang, T.J.; Yu, W.R. Simulation of mechanical behavior of temperature-responsive braided stents made of shape memory polyurethanes. *J Biomech* **2010**, *43*, 632-643.

68. Xue, L.; Dai, S.; Li, Z. Biodegradable shape-memory block co-polymers for fast self-expandable stents. *Biomaterials* **2010**, *31*, 8132-8140.

69. Laschke, M.W.; Strohe, A.; Scheuer, C.; Eglin, D.; Verrier, S.; Alini, M.; Pohlemann, T.; Menger, M.D. In vivo biocompatibility and vascularization of biodegradable porous polyurethane scaffolds for tissue engineering. *Acta Biomater.* **2009**, *5*, 1991-2001.

70. Hong, Y.; Ye, S.H.; Pelinescu, A.L.; Wagner, W.R. Synthesis, characterization, and paclitaxel release from a biodegradable, elastomeric, poly(ester urethane)urea bearing phosphorylcholine groups for reduced thrombogenicity. *Biomacromolecules* **2012**, *13*, 3686-3694.

71. Page, J.M.; Prieto, E.M.; Dumas, J.E.; Zienkiewicz, K.J.; Wenke, J.C.; Brown-Baer, P.; Guelcher, S.A. Biocompatibility and chemical reaction kinetics of injectable, settable polyurethane/allograft bone biocomposites. *Acta Biomater.* **2012**, *8*, 4405-4416.

72. Huang, W.M.; Yang, B.; Zhao, Y.; Ding, Z. Thermo-moisture responsive polyurethane shape-memory polymer and composites: A review. *J. Mater. Chem.* **2010**, *20*, 3367.

73. Frigione, M.; Aiello, M.A.; Naddeo, C. Water effects on the bond strength of concrete/concrete adhesive joints. *Constr. Build. Mater.* **2006**, *20*, 957-970.

74. Yu, Y.J.; Hearon, K.; Wilson, T.S.; Maitland, D.J. The effect of moisture absorption on the physical properties of polyurethane shape memory polymer foams. *Smart Mater. Struct.* **2011**, *20*.

75. Canton, G.; Levy, D.I.; Lasheras, J.C. Changes in the intraaneurysmal pressure due to hydrocoil embolization. *American Journal of Neuroradiology* **2005**, *26*, 904-907.

76. Zhang, S.; Ren, Z.; He, S.; Zhu, Y.; Zhu, C. FTIR spectroscopic characterization of polyurethane-urea model hard segments (puumhs) based on three diamine chain extenders. *Spectroc. Acta Part A* **2007**, *66*, 188-193.

77. Zhang, Y.; Maxted, J.; Barber, A.; Lowe, C.; Smith, R. The durability of clear polyurethane coil coatings studied by FTIR peak fitting. *Polym. Degrad. Stab.* **2013**, *98*, 527-534.

78. Crompton, T.R. Thermal methods of polymer analysis. **2013**.

79. Young, R.J.; Lovell, P.A. Introduction to polymers. CRC Press, Taylor and Francis Group, LLC. Boca Raton, Florida, USA. **2011**.

80. Yuan, Y.; Lee, T.R. Contact angle and wetting properties. **2013**, *51*, 3-34.

81. Lu, X.; Jiang, B. Glass transition temperature and molecular parameters of polymer. *Polymer* **1991**, *32*, 471-478.

82. Ramakrishna, S.; Mayer, J.; Wintermantel, E.; Leong, K.W. Biomedical applications of polymer-composite materials: A review. *Composites Science and Technology* **2001**, *61*, 1189-1224.

83. *Biomaterials science: An introduction to materials in medicine*; Academic Press: 1996.

84. Dawlee, S. Studies on radiopaque polymers for biomedical applications Sree Chitra Tirunal Institute for Medical Sciences and Technology: Thiruvananthapuram, India, Country, 2011.

85. Mottu, F.; Rüfenacht, D.; Doelker, E. Radiopaque polymeric materials for medical applications: Current aspects of biomaterial research. *Investigational Radiology* **1999**, *34*, 323-335.

86. Kiran, S.; James, N.R.; Jayakrishnan, A.; Joseph, R. Polyurethane thermoplastic elastomers with inherent radiopacity for biomedical applications. *J Biomed Mater Res A* **2012**, *100*, 3472-3479.

87. Tbanoo, B.C.; Sunny, M.C.; Jayakrishnan, A. Tantalum-loaded polyurethane microspheres for particulate embolization: Preparation and properties. *Biomaterials* **1991**, *12*, 525-528.

88. He, J.; Söderling, E.; Lassila, L.V.J.; Vallittu, P.K. Incorporation of an antibacterial and radiopaque monomer in to dental resin system. *Dental Materials* **2012**, *28*, 110-117.

89. Tallia, F.; Gallo, M.; Pontiroli, L.; Baino, F.; Fiorilli, S.; Onida, B.; Anselmetti, G.C.; Manca, A.; Vitale-Brovarone, C. Zirconia-containing radiopaque mesoporous bioactive glasses. *Materials Letters* **2014**, *130*, 281-284.

90. Reis, L.O.; Kaizer, M.R.; Ogliari, F.A.; Collares, F.M.; Moraes, R.R. Investigation on the use of triphenyl bismuth as radiopacifier for (di)methacrylate dental adhesives. *International Journal of Adhesion & Adhesives* **2014**, *48*, 80-84.

91. Primack, J.E. Radiopaque denture materials. *The Journal of Prosthetic Dentistry* **1972**, *28*, 363-368.

92. Amirouche-Korichi, A.; Mouzali, M.; Watts, D.C. Effects of monomer ratios and highly radiopaque fillers on degree of conversion and shrinkage-strain of dental resin composites. *Dental Materials* **2009**, *25*, 1411-1418.

93. Amirouche, A.; Mouzali, M.; Watts, D.C. Radiopacity evaluation of bis-gma/tegdma/opaque mineral filler dental composites. *Journal of Applied Polymer Science* **2007**, *104*, 1632-1639.

94. Rawls, H.R.; Starr, J.; Kasten, F.H.; Murray, M.; Smid, J.; Cabasso, I. Radiopaque acrylic resins containing miscible heavy-metal compounds. *Dental Materials* **1990**, *6*, 250-255.

95. Kiran, S.; James, N.R.; Joseph, R.; Jayakrishnan, A. Synthesis and characterization of iodinated polyurethane with inherent radiopacity. *Biomaterials* **2009**, *30*, 5552-5559.

96. DamiaMawad; Lauto, A.; Penciu, A.; Mehier, H.; Fenet, B.; Fessi, H.; Chevalier, Y. Synthesis and characterization of novel radiopaque poly(allyl amine) nanoparticles. *Nanotechnology* **2010**, *21*.

97. Gall, K.; Dunn, M.L.; Liu, Y.; Finch, D.; Munshi, N.A. Shape memory polymer nanocomposites. *Acta Materialia* **2002**, *50*, 5115-5126.

98. Hasan, S.M.; Raymond, J.E.; Wilson, T.S.; Keller, B.K.; Maitland, D.J. Effects of isophorone diisocyanate on the thermal and mechanical properties of shape-memory polyurethane foams. *Macromolecular Chemistry and Physics* **2014**, *215*, 2420–2429.

99. Kampmann, C.; Brzezinska, R.; Abidini, M.; Wenzel, A.; Wippermann, C.-F.; Habermehl, P.; Knuf, M.; Schumacher, R. Biodegradation of tungsten embolisation coils used in children. *Pediatric Radiology* **2002**, *32*, 839-843.

100. Peustera, M.; Fink, C.; Schnakenburg, C.v. Biocompatibility of corroding tungsten coils: In vitro assessment of degradation kinetics and cytotoxicity on human cells. *Biomaterials* **2003**, *24*, 4057–4061.

101. Peuster, M.; Fink, C.; Wohlsein, P.; Bruegmann, M.; Gunther, A.; Kaese, V.; Niemeyer, M.; Haferkamp, H.; Schnakenburg, C.v. Degradation of tungsten coils implanted into the subclavian artery of newzealand white rabbits is not associated with local or systemic toxicity. *Biomaterials* **2003**, *24*, 393-399.

102. Jakhmola, A.; Antona, N.; Antona, H.; Messaddeq, N.; Hallouard, F.; Klymchenko, A.; Mely, Y.; Vandamme, T.F. Poly-ε-caprolactone tungsten oxide nanoparticles as a contrast agent for x-ray computed tomography. *Biomaterials* **2014**, *35*.

103. Huang, W.M.; Yang, B.; Zhao, Y.; Ding, Z. Thermo-moisture responsive polyurethane shape-memory polymer and composites: A review. *J Mater Chem* **2010**, *20*, 3367.

104. Hwang, W.; Singhal, P.; Miller, M.W.; Maitland, D.J. In vitro study of transcatheter delivery of a shape memory polymer foam embolic device for treating cerebral aneurysms. *Journal of Medical Devices* **2013**, *7*, 020932-020932.

105. Bistričić, L.; Baranović, G.; Leskovac, M.; Bajsić, E.G. Hydrogen bonding and mechanical properties of thin films of polyether-based polyurethane–silica nanocomposites. *European Polymer Journal* **2010**, *46*, 1975-1987.

106. Bugnicourt, E.; Galy, J.; Gerard, J.-F.; Barthel, H. Effect of sub-micron silica fillers on the mechanical performances of epoxy-based composites. *Polymer* **2007**, *48*, 1596-1605.

107. Khankrua, R.; Pivsa-Art, S.; Hiroyuki, H.; Suttiruengwong, S. Thermal and mechanical properties of biodegradable polyester/silica nanocomposites. *Energy Procedia* **2013**, *34*, 705-713.

108. Fereidoon, A.; Memarian, S.; Albooyeh, A.; Tarahomi, S. Influence of mesoporous silica and hydroxyapatite nanoparticles on the mechanical and morphological properties of polypropylene. *Materials & Design* **2014**, *57*, 201-210.

109. Haldorai, Y.; Shim, J.-J.; Lim, K.T. Synthesis of polymer–inorganic filler nanocomposites in supercritical co2. *The Journal of Supercritical Fluids* **2012**, *71*, 45– 63.

110. Zare, Y. Determination of polymer–nanoparticles interfacial adhesion and its role in shape memory behavior of shape memory polymer nanocomposites. *International Journal of Adhesion and Adhesives* **2014**, *54*, 67-71.

111. Wichmann, M.H.G.; Cascione, M.; Fiedler, B.; Quaresimin, M.; Schulte, K. Influence of surface treatment on mechanical behaviour of fumed silica/epoxy resin nanocomposites. *Composite Interfaces* **2006**, *13*, 699-715.

112. Tercero, J.E.; Namin, S.; Lahiri, D.; Balani, K.; Tsoukias, N.; Agarwal, A. Effect of carbon nanotube and aluminum oxide addition on plasma-sprayed hydroxyapatite coating's mechanical properties and biocompatibility. *Materials Science and Engineering: C* **2009**, *29*, 2195-2202.

113. Gupta, A.; Tripathi, G.; Lahiri, D.; Balani, K. Compression molded ultra high molecular weight polyethylene–hydroxyapatite–aluminum oxide–carbon nanotube hybrid composites for hard tissue replacement. *Journal of Material Science and Technology* **2013**, *29*, 514-522.

114. Hasan, S.M.; Harmon, G.; Zhou, F.; Raymond, J.E.; Gustafson, T.P.; Wilson, T.S.; Maitland, D.J. Tungsten-loaded smp foam nanocomposites with inherent radiopacity and tunable thermo-mechanical properties. *Polymers for Advanced Technologies* **2015**, n/a-n/a.

115. Lalwani, G.; Henslee, A.M.; Farshid, B.; Parmar, P.; Lin, L.; Qin, Y.X.; Kasper, F.K.; Mikos, A.G.; Sitharaman, B. Tungsten disulfide nanotubes reinforced biodegradable polymers for bone tissue engineering. *Acta Biomater* **2013**, *9*, 8365-8373.

116. Glaskova, T.; Zarrelli, M.; Aniskevich, A.; Giordano, M.; Trinkler, L.; Berzina, B. Quantitative optical analysis of filler dispersion degree in mwcnt–epoxy nanocomposite. *Composites Science and Technology* **2012**, *72*, 477-481.

117. Tang, L.-C.; Zhang, H.; Sprenger, S.; Ye, L.; Zhang, Z. Fracture mechanisms of epoxy-based ternary composites filled with rigid-soft particles. *Composites Science and Technology* **2012**, *72*, 558-565.

118. Johnsen, B.B.; Kinloch, A.J.; Mohammed, R.D.; Taylor, A.C.; Sprenger, S. Toughening mechanisms of nanoparticle-modified epoxy polymers. *Polymer* **2007**, *48*, 530-541.

119. Omrani, A.; Simon, L.C.; Rostami, A.A. The effects of alumina nanoparticle on the properties of an epoxy resin system. *Materials Chemistry and Physics* **2009**, *114*, 145-150.

120. Zhao, S.; Schadler, L.S.; Duncan, R.; Hillborg, H.; Auletta, T. Mechanisms leading to improved mechanical performance in nanoscale alumina filled epoxy. *Composites Science and Technology* **2008**, *68*, 2965-2975.

121. Convention, T.U.S.P., 788 particulate matter in injections In *Revision Bulletin*, The United States Pharmacopeial Convention: Rockville, MD, October 1, 2011; Vol. 788.

122. Di Virgilio, A.L.; Reigosa, M.; Arnal, P.M.; Fernández Lorenzo de Mele, M. Comparative study of the cytotoxic and genotoxic effects of titanium oxide and aluminium oxide nanoparticles in chinese hamster ovary (cho-k1) cells. *Journal of Hazardous Materials* **2010**, *177*, 711-718.

123. Hashimoto, M.; Imazato, S. Cytotoxic and genotoxic characterization of aluminum and silicon oxide nanoparticles in macrophages. *Dental Materials* **2015**, *31*, 556-564.

124. Hussain, S.M.; Hess, K.L.; Gearhart, J.M.; Geiss, K.T.; Schlager, J.J. In vitro toxicity of nanoparticles in brl 3a rat liver cells. *Toxicology in Vitro* **2005**, *19*, 975-983.

125. Stoebe, T.; Lin, Z.; Hill, R.M.; Ward, M.D.; Davis, H.T. Surfactant-enhanced spreading. *Langmuir* **1996**, *12*, 337-344.

126. Tadros, T.F. Surfactants, industrial applications. In *Encyclopedia of physical science and technology (third edition)*; Meyers, R. A., Ed. Academic Press: New York, 2003.

127. Lim, H.; Kim, S.H.; Kim, B.K. Effects of silicon surfactant in rigid polyurethane foams. *Polymer Letters* **2008**, *2*, 194-200.

128. Yilgör, E.; Yilgör, I. Silicone containing copolymers: Synthesis, properties and applications. *Progress in Polymer Science* **2014**, *39*, 1165-1195.

129. Naghash, H.J.; Abili, B. Synthesis of a silicone containing allylic monomer and its uses in the waterborne polyurethane/vinyl acetate–acrylic hybrid emulsion copolymers. *Progress in Organic Coatings* **2010**, *69*, 486-494.

130. Anthony J. O'Lenick, J., Basic silicone chemistry - a review. In *Silicone Spectator*, SurfaTech Corporation: Dacula, GA, USA, 1999.

131. Hill, R.M. *Silicone surfactants*; Marcel Dekker, Inc.: Basek, Switzerland, 1999.

132. Wu, C.; Peng, J.; Li, J.; Bai, Y.; Hu, Y.; Lai, G. Synthesis of poly(ethylene glycol) (peg) functionalized ionic liquids and the application to hydrosilylation. *Catalysis Communications* **2008**, *10*, 248-250.

133. So, H.; Fawcett, A.S.; Sheardown, H.; Brook, M.A. Surface-active copolymer formation stabilizes peg droplets and bubbles in silicone foams. *J Colloid Interface Sci* **2013**, *390*, 121-128.

134. Roy, A.K. A review of recent progress in catalyzed homogeneous hydrosilation (hydrosilylation). In *Advances in organometallic chemistry*; Robert West, A. F. H., Mark, J. F., Eds.; Academic Press: 2007.

135. Bai, Y.; Zhang, F.; Li, J.; Xu, Y.; Peng, J.; Xiao, W. Application of polyethyleneglycol (peg) functionalized ionic liquids for the rhodium-catalyzed hydrosilylation reaction of alkenes. *Journal of Organometallic Chemistry* **2015**, *794*, 65-69.

136. Murthy, R.; Cox, C.D.; Hahn, M.S.; Grunlan, M.A. Protein-resistant silicones: Incorporation of poly(ethylene oxide) via siloxane tethers. *Biomacromolecules* **2007**, *8*, 3244-3252.

137. ASTM *Standard test methods for flexible cellular materials—slab, bonded, and molded urethane foams*; ASTM International: West Conshohocken, PA.

138. Launer, P.J. *Infrared analysis of organosilicon compounds: Spectra-structure correlations*; 1987.

139. Kovalchuk, N.M.; Trybala, A.; Starov, V.; Matar, O.; Ivanova, N. Fluoro- vs hydrocarbon surfactants: Why do they differ in wetting performance? *Advances in Colloid and Interface Science* **2014**, *210*, 65-71.

140. Ge, X.; Li, M.-C.; Li, X.X.; Cho, U.R. Effects of silane coupling agents on the properties of bentonite/nitrile butadiene rubber nanocomposites synthesized by a novel green method. *Applied Clay Science* **2015**, *118*, 265-275.

141. Mathialagan, M.; Ismail, H. Optimization and effect of 3-aminopropyltriethoxysilane content on the properties of bentonite-filled ethylene propylene diene monomer composites. *Polymer Composites* **2012**, *33*, 1993-2000.